UNIVERSITY OF CALIFORNIA, MERCED

The Extension of Symbolic Dynamics to 3D Volume-Preserving Maps

A dissertation submitted in partial satisfaction of the
requirements for the degree
Doctor of Philosophy

in

Physics

by

Joshua G. Arenson

Committee in charge:

Professor Dustin Kleckner, Chair
Professor Kevin A. Mitchell
Professor Suzanne Sindi

2021

The dissertation of Joshua G. Arenson is approved, and it is acceptable in quality and form for publication on microfilm and electronically:

_____

(Professor Kevin A. Mitchell)

_____

(Professor Suzanne Sindi)

_____

(Professor Dustin Kleckner, Chair)

University of California, Merced

2021

EPIGRAPH

The most important step a man can take.
It's not the first one, is it?
It's the next one.
Always the next step.
—Brandon Sanderson

TABLE OF CONTENTS

LIST OF FIGURES

LIST OF TABLES

ACKNOWLEDGEMENTS

Enormous thanks are due to my great advisor Kevin Mitchell for all his hard work these last several years. I could not possibly have done this without him. Credit also goes to my ever patient committee members who have always been there for me.

Special acknowledgement to Spencer Smith without whom my first paper at UC Merced would have been possible. Much of the work presented here has been a result off his help early in my career. Thanks also to Sullimon Sattari for his constant help with all things MATLAB and HLD.

Thanks to my family, who have restrained themselves only occasionally asking me when I will be done and get a real job. They have been extremely supportive all along and most especially this last year.

I want to acknowledge Spencer Smith, Kevin Mitchell, Suzanne Sindi, and Eric Roberts for allowing me to use portions of our papers in this dissertation. Finally we want to acknowledge ARO for their funding on our early work.

VITA

2011	B. A. in Physics and Mathematics, Whittier College
2014	M. S. in Physics, California State University, Long Beach
2014-2021	Graduate Teaching Assistant, University of California, Merced
2021	Ph. D. in Physics, University of California, Merced

PUBLICATIONS

Spencer A. Smith, Joshua Arenson, Eric Roberts, Suzanne Sindi, and Kevin A. Mitchell, "Topological chaos in a three-dimensional spherical fluid vortex.", *Euro-Phys. Lett.*, 117, 2017.

Joshua Arenson and Kevin A. Mitchell, "Topological dynamics of volume-preserving maps without an equatorial heteroclinic curve", *Physica D*, 424, 2021

ABSTRACT OF THE DISSERTATION

The Extension of Symbolic Dynamics to 3D Volume-Preserving Maps

by

Joshua G. Arenson
Doctor of Philosophy in Physics
University of California Merced, 2021
Professor Dustin Kleckner, Chair

Understanding the topological structure of phase space for dynamical systems in higher dimensions is critical for numerous applications, including transport of objects in the solar system, systems of fluids, and charged particles in crossed magnetic and electric fields. Many topological techniques have been developed to study maps of two-dimensional (2D) phase spaces, but extending these techniques to higher dimensions is often a major challenge or even impossible. One such technique, homotopic lobe dynamics (HLD), has shown great success in analyzing the stable and unstable manifolds of hyperbolic fixed points for area-preserving maps in two dimensions. The output of the HLD technique is a symbolic description of the minimal underlying topology of the invariant manifolds. The present work extends HLD to volume-preserving maps in three dimensions. We extend HLD to systems that have equatorial heteroclinic intersections, pole-to-pole invariant circles, and forced pole-to-pole heteroclinic intersections. In order to extend HLD to these cases, we went through multiple computational methodologies as well shift our perspective of manifolds in 3D. We demonstrate the power of the HLD by applying it to increasingly complex numerical and theoretical examples.

Chapter 1

Introduction

1.1 Motivation

It is commonly believed that chaotic systems are completely random without pattern and no way to predict the time evolution of the system. However, while extremely complex they do have patterns; in fact, most have underlying patterns that result in beautiful dynamics. A common example is the fractal patterns that many chaotic systems exhibit. Additionally, while a system may appear random there are many larger properties in the system that can be discovered with careful analysis. Take for example the motion of particles in the ocean [71]. At first glance the motion of any individual tracer or particle would appear random; however, large scale structures such as deep ocean currents can form and create patterns within the complex system.

Another example of a chaotic system is the golden braid studied by Thiffeault et. al. [63, 27, 26]. In this system a set of three rods are set in a row. The middle rod rotates counterclockwise with the left rod, and then the new middle rod (old left rod) rotates clockwise with the right rod. If one were to place a rubber band about the rods, we would find that the rubber band stretches and folds such that its length exponentially increases–at least until it snapped! The rates of stretching and mixing for the golden braid can be identified using chaotic dynamics.

Discovering the hidden complexities of chaotic systems sheds light on some of the most complex physical systems. For example, we use early time information

for a complex system to determine the forced dynamics in the long term. Such analytical tools can be used to examine complex systems and identify long term trends, which is useful for a variety of applications, such as finance, fluid dynamics, and meteorological phenomena.

1.2 Background

In the early 1880s Henri Poincare noticed that there existed solutions to the three body problem such that the trajectories were not truly periodic, yet neither would they asymptotically approach or move away from a fixed point [57]. A classic example of such an orbit is the Lorentz attractor, whose trajectories orbit around two attractors yet are nonperodic. Many others besides Poincare would study chaotic systems over the next half century, making progress in their understanding, but the field could not truly flourish until the mid-nineteenth century and the advancement of modern computers.

The original definition of a chaotic system is attributed to Robert L. Devaney who identified three properties the system must have [32]:

1. It must be sensitive to initial conditions.

2. It must be topologically mixing.

3. It must have dense periodic orbits.

The first property implies that small variations in initial conditions result in drastically different trajectories over time. In the second property topological mixing means that given two open sets, after a certain number of iterates the image of the first set intersects the second set for every iteration. In the final property dense periodic orbits means that any point in phase space will be approached by some periodic orbit. Taken together, these properties give a good definition of a chaotic system. However, the study of chaotic dynamics preceded Devaney's definition, which wasn't formulated until the 1980s.

With the advent of the modern computer, researchers could study chaotic systems with much more ease and depth. A particularly striking example of this is

the story of how Lorentz became interested in chaotic systems [41]. While studying weather systems, he needed to see a sequence of data again. To save time, he tracked down the conditions in the middle of his simulation and started to run the simulation again using these printed conditions as initial conditions. To his surprise, the machine gave a significantly different prediction. While the machine had a precision of up to six decimals the printout rounded to the third. Such a minor change in his initial conditions created a wildly different outcome. Lorentz would go on to discover the Lorentz attractor, a classic nonperodic system. Without modern computers the different outcomes due to a slight change in initial conditions might have been missed. The improvement of the modern computer resulted in a rapid advancement and diversification of chaos theory.

Computers are particularly useful for the study of discrete maps. A discrete map iterates an initial point to another; for example, if a point $\boldsymbol{p}_n$ exists in phase space then the map M will iterate it forward such that $\boldsymbol{p}_{n+1} = M(\boldsymbol{p}_n)$. The map M^{-1} (if it exists) will iterate the point $\boldsymbol{p}_{n+1}$ backward such that $\boldsymbol{p}_n = M^{-1}(\boldsymbol{p}_{n+1})$. An initial point has a *trajectory* that is the repeated iteration (both forward and backward) of the initial point. If the forward iterate of a point in phase space is the same point, i.e., $M(\boldsymbol{p}) = \boldsymbol{p}$, then the point is a fixed point. A discrete map also has a related Jacobian matrix. Each point in phase space has a set of eigenvectors and eigenvalues that arise from the Jacobian matrix at that point. The eigenvectors of the Jacobian at a fixed point linearize to the stable and unstable manifolds near the fixed point. A stable manifold is defined as the set of trajectories whose forward iterates asymptotically approach the fixed point. The unstable manifold is the set of trajectories whose backward iterates asymptotically approach the fixed point. Finally if the n^{th} iterate of a point is the same point, i.e., $M^n(\boldsymbol{p}) = \boldsymbol{p}$ then the point is n-periodic. While beyond the scope of this work, the study of periodic orbits in discrete maps is a active field of research [61].

A well studied example of a discrete map is the Hénon Map:

$$M = \begin{cases} x_{n+1} = 1 - kx_n^2 + y_n \\ y_{n+1} = bx_n \end{cases} \tag{1.1}$$

where k and b are constants. For the parameters $k = 1.4$ and $b = 0.3$ the Hénon Map is chaotic, for other values it could be chaotic, intermittent, or converge to a periodic orbit. The relative simplicity of the Hénon Map has resulted in it being one of the most well studied dynamical systems. Though simple it still proves to be effective for demonstrating new techniques.

We are particularly interested in the study of two and three dimensional maps like the Hénon Map, and the underlying structures that occur therein. A common theme of this research is the idea of *topological forcing*. Topological forcing is the idea that structures arising in the early dynamics of a system will force the existence of infinitely many long-time structures.

Initial studies of the phase space geometry of reaction dynamics were restricted to two active degrees of freedom [19, 16, 17]. Already for two degrees of freedom, it was seen that chaos could play a critical role. The current frontier for understanding phase space structures governing reaction dynamics is systems with three or more degrees of freedom [69, 66, 67, 28, 38, 68, 56, 25, 34, 42, 54]. Such work is not solely relevant to reaction dynamics but to other transport problems in Hamiltonian systems as well, such as celestial dynamics. Much of the research on transport for three degree-of-freedom systems has focused on transition-state theory, based on *normally hyperbolic invariant manifolds* (NHIMs). A NHIM is the natural generalization of a hyperbolic fixed point and a hyperbolic set. For example, a hyperbolic fixed point in phase space is a 0-dimensional NHIM. Less attention has been paid to the global structure of the stable and unstable manifolds attached to NHIMs. These manifolds are co-dimension one and (in the best case) divide phase space into topologically distinct regions, unfortunately, the invariant manifolds need not define (finite-volume) *resonance zones* i.e. regions of phase space enclosed by the stable and unstable manifold, and *lobes*, i.e. submanifolds of the unstable manifold attached at its ends to the stable manifold. Hence these manifolds need not partition phase space into finite domains [5, 64]. This was first realized by Wiggins [70], followed by an explicit chemical example by Gililan and Ezra [29]. As an alternative approach, Jung, Montoya, and collaborators [36, 21, 30, 20, 31] have studied the topological structure of chaotic scattering

functions for three-degree-of-freedom Hamiltonian systems. They have shown how symbolic dynamics can be extracted from the doubly-differential cross section and then related back to the fractal structure of the chaotic saddle itself.

Three-degree-of-freedom Hamiltonian systems generate flows in a six-dimensional phase space as each degree-of-freedom has a position and momentum component. If one is fortunate, this flow can be reduced, via a good surface-of-section, to a simplectic map on a four-dimensional phase space. This work considers volume-preserving maps of a three-dimensional (3D) phase space as an intermediate step to volume-preserving maps in four dimensions (4D). As previous studies in 3D have shown, even these maps have a wealth of complex behavior, and many open questions about their dynamics remain [39, 40, 22, 35, 45]. We consider here the global structure of intersecting two-dimensional (2D) stable and unstable manifolds of hyperbolic fixed points in 3D. Specifically, we use finite pieces of these manifolds to generate symbolic dynamics describing the forced subsequent evolution of the manifolds. We note that complications can occur in 3D that have no analogue in 2D; namely, the invariant manifolds of fixed points may not specify well defined resonance zones and lobes. We illustrate two methods for circumventing such complications.

While we are interested in 3D volume-preserving maps as a stepping stone to the study of higher dimensional phase spaces, 3D volume-preserving maps are an important area of research in their own right and exhibit a plethora of fascinating phenomena. Within the realm of 3D volume-preserving maps, one can study behavior as diverse as particle advection in incompressible fluid flows [1, 44], mixing of granular media in a tumbler [9], the motion of charged particles along magnetic field lines in a plasma [4], and circular swimmers in a 2D incompressible fluid [37, 6]. A deeper history of 2D and 3D chaotic transport can be found in reviews by Aref et al. [1] and Meiss [44].

Our work on 3D volume-preserving maps is based on prior studies of 2D maps. These studies focused on the structure of one-dimensional invariant manifolds of hyperbolic fixed points and periodic orbits, and how these manifolds intersect one another [23, 58, 59, 24]. If these stable and unstable manifolds intersect, they

force a complex series of subsequent intersections. One technique to study the complicated topology that arises is homotopic lobe dynamics (HLD) [50, 49, 51, 52, 55, 8, 60, 61]. The underlying goal of HLD is to reduce the complex networks of stable and unstable manifolds and their intersections to a set of symbolic equations that describe the minimal underlying topology. An alternative technique for understanding the underlying topology of invariant manifolds in 2D was developed by Collins [10, 11, 12, 13, 14]. Collins's approach is based on train tracks and the Bestvina-Handel algorithm [7]. This approach was recently shown to be dual to HLD [15]. The input to both techniques is finite-time information in the form of finite-length intervals of the stable and unstable manifolds and their intersections; the output is a set of symbolic equations that predicts the minimum forced evolution of the system arbitrarily far into the future. Said another way, the existence of finite-time topological structure forces future structure to exist in specific, predictable ways. The symbolic dynamics in 2D HLD describe the evolution of 1D curves. It also allows one to assign symbolic itineraries to trajectories, thereby classifying chaotic trajectories of 2D maps.

Though our work takes the homotopy perspective, there is a significant literature taking the homology point of view and using the Conley index [46, 47, 48, 18]. This can be used to develop rigorous symbolic dynamics, compute topological entropy, identify periodic orbits, etc., and it has the advantage of being based in linear algebra. However, because abelian groups in homology can be transformed into the non-abelian groups used in homotopy, some information and richness cannot be captured.

The HLD technique is described in depth in chapter 2; however, our work has focused on extending HLD to 3D maps [43, 2]. In chapter 2 we discuss the structures that allow us to perform HLD as well as working through an example known as the complete horseshoe. Following or exploration of 2D HLD we will expand into 3D HLD with an overview of the necessary differences and adjustments made to perform HLD in 3D. We will explore the numerical techniques necessary to produce the escape-time-plots (ETP) for a numerical example. In chapter 3.1 we examine a "in the wild" system produced by the numerical ETP and its dynamics [62].

In chapter 4 we discuss our initial foray into the structure of the quadratic family of maps. We found during these explorations that our current understanding was insufficient to adequately explore the map and a shift of focus was necessary. Chapter 5 describes the extension to 3D HLD necessary to understand systems with pole-to-pole intersection curves [2]. Here we explore a number of "toy model" systems to illustrate the new methods. In Chapter 6 we reexamine the quadratic family of maps and apply our new understanding of systems with pole-to-pole intersections. We apply a variation on HLD to extract the topological information contained within the system. Finally we discuss some of the outstanding work in the area and possible future projects.

Chapter 2

Homotopic Lobe Dynamics

One powerful method to understand the dynamics of 2D and 3D volume-preserving maps is Homotopic Lobe Dynamics (HLD). HLD uses the topological intersections between stable and unstable manifolds to understand the underlying dynamics of a system. A stable manifold is the set of points whose forward iterates asymptotically approach a fixed point while an unstable manifold is the set of points whose backward iterates asymptotically approach the fixed point. In 2D HLD is applied to area-preserving maps with hyperbolic fixed points. A hyperbolic fixed point is a fixed point that has at least one stable and one unstable eigenvector at the fixed point. The eigenvectors of the fixed point are the eigenvectors of the Jacobian of the map at the fixed point. The eigenvector $\vec{v}_n$ is unstable if the eigenvalue $\lambda_n > 1$ while the eigenvector is stable if $\lambda_n < 1$. The number of stable and unstable eigenvectors a hyperbolic fixed point has indicates the dimensionality of the corresponding stable and unstable manifold. For example in 2D discrete maps a hyperbolic fixed point must have a only one stable and one unstable eigenvector. Thus the fixed point must have a 1D unstable manifold and a 1D stable manifold.

HLD can only be applied to systems in which a stable and unstable manifold of the same dimension intersect. Imagine that the stable and unstable manifold intersects at a initial point $\boldsymbol{p}_n$. $\boldsymbol{p}_n$ lies on both the stable and unstable manifolds. Mapping $\boldsymbol{p}_n$ forward one iterate produces the point $\boldsymbol{p}_{n+1}$. Since the point $\boldsymbol{p}_n$ is an intersection of the stable and unstable manifolds $\boldsymbol{p}_{n+1}$ must also be an intersection on the stable and unstable manifolds. The forward iterates of $\boldsymbol{p}_n$ will follow the

stable manifold in towards the fixed point while the backward iterates of $\boldsymbol{p}_n$ follows the unstable manifold to the fixed point. Thus the set of all $\boldsymbol{p}$ is an infinite set of intersections between the stable and unstable manifolds.

The stable and unstable manifolds in a system can intersect with each other, but an unstable manifold cannot intersect another unstable manifold, or itself. The same restriction applies to stable manifolds. By definition all stable and unstable manifolds must be locally Euclidean; however, any self-intersection of the stable or unstable manifold will not be locally Euclidean at the intersection point, thus a self-intersecting manifold cannot occur [65]. Another way to consider this is that any self-intersection of the manifold would have to iterate to two different points.

In HLD if we examine a finite set of the intersections between the stable and unstable manifolds and from these intersections construct a set of symbolic dynamics describe how the manifolds are forced to intersect at higher iterates.

2.1 2D Homotopic Lobe Dynamics

At its core HLD takes a complicated set of intersections between finite stable and unstable manifolds as in Fig. 2.1 and reduces the information to a series of symbolic equations. These symbolic equations describe the long-time structure of the map. In turn, the symbolic equations can be described by a transition graph as in Fig. 2.2.

The hyperbolic fixed point $\boldsymbol{z}_0$ of a 2D map will have one unstable eigenvector and one stable eigenvector. Near the fixed point we linearize the stable manifold in the direction of the stable eigenvector. The same can be done for the unstable manifold with the unstable eigenvector. To generate the stable and unstable manifolds we start with a point, $\boldsymbol{p}_n$, near the fixed point in the direction of the appropriate eigenvector. We map this point forward to $\boldsymbol{p}_{n+1}$. The line connecting $\boldsymbol{p}_n$ to $\boldsymbol{p}_{n+1}$ is called the *fundamental segment*. The manifold is then "grown" away from $\boldsymbol{z}_0$ by iterating the fundmanetal segment forward (for the unstable manifold) or backward (for the stable manifold). If the fundamental segment is the curve from $\boldsymbol{p}_n$ to $\boldsymbol{p}_{n+1}$ then the first iterate is the curve connecting $\boldsymbol{p}_{n+1}$ to $\boldsymbol{p}_{n+2}$. Con-

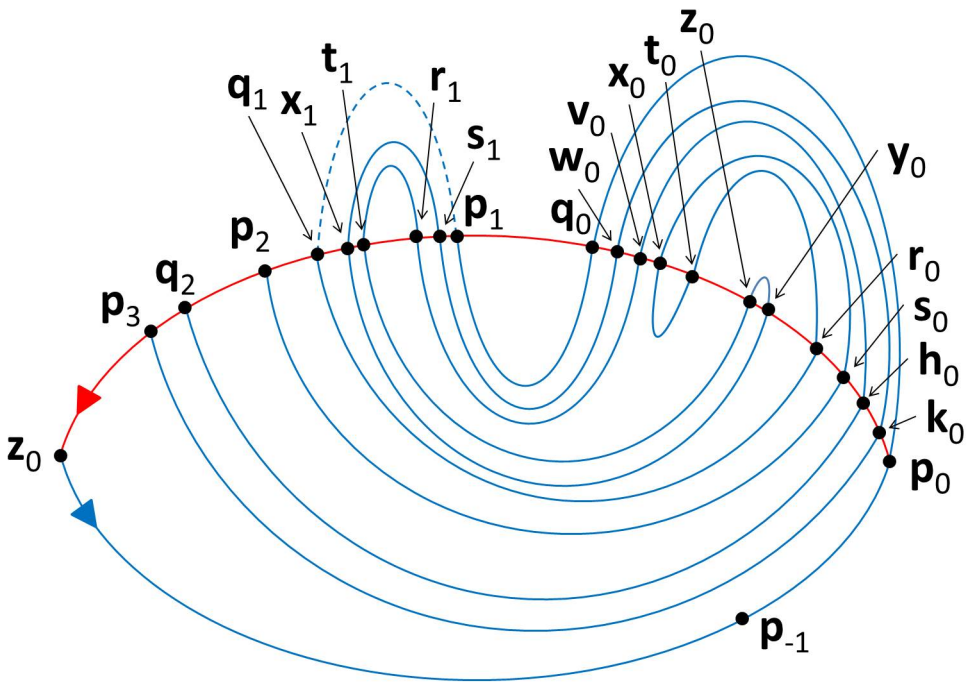

Figure 2.1: The complicated interactions between the stable (red) and unstable manifolds (blue).

catenating a few iterates of the fundamental segment produces manifolds such as those seen in fig. 2.3. After many iterations of the fundamental segment manifolds may grow to look like those in fig. 2.1.

In an HLD applicable system the stable and unstable manifolds intersect. The "first" intersection, $\boldsymbol{p}_0$, between the stable and unstable manifolds is referred to as the *primary intersection point* (pip). The manifolds up to the pip will divide phase space into an exterior region and an interior region. We call the interior region the *resonance zone* as in Fig. 2.4.

The infinite set of points that make up the stable and unstable manifolds is known as the *tangle*, while the *trellis* is a finite subset of the unstable and stable manifolds that make up the tangle. The tangle will have an infinite number of intersection points as discussed above. In the full tangle two points are a *neighbor pair* if they have no other intersection points on the stable and unstable manifolds connecting them for all iterates of the neighbor pair. If a pair of pair of points

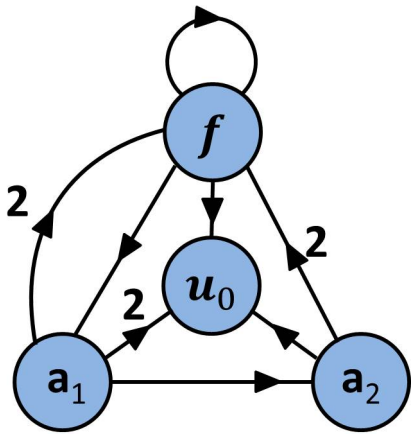

Figure 2.2: The symbolic equations that describe the dynamics of a map can be reduced to a transition graph.

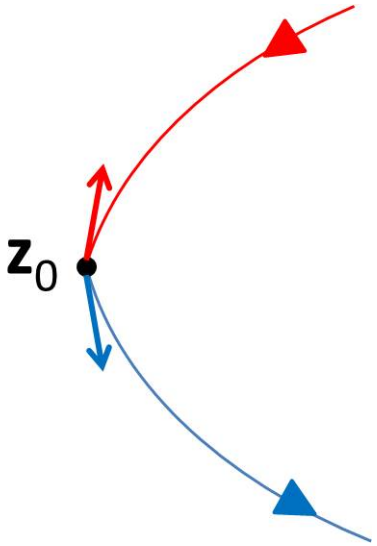

Figure 2.3: The fixed point z_0, its stable and unstable eigenvectors as well as a few iterates of the fundamental segment.

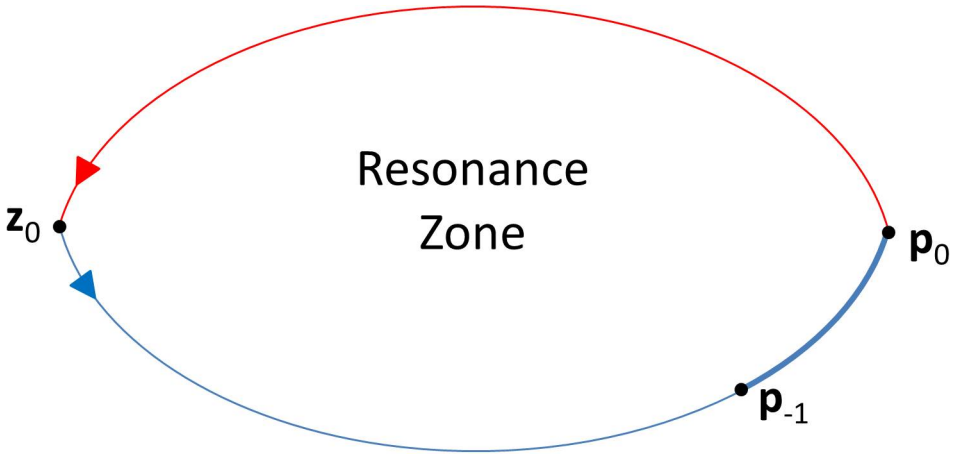

Figure 2.4: The stable and unstable manifolds up to the primary intersection point $\boldsymbol{p}_0$. The manifolds divide phase space into an exterior region and interior region called the resonance zone.

have no intersections between on the tangle well call them a *pseudoneighbor pair*. A pseudoneighbor pair is not necessarily also a neighbor pair as new intersections may occur between the pseudoneighbor pair at higher iterates.

We use the notation W^S and W^U to denote the stable and unstable manifolds respectively. The unstable submanifold connecting $\boldsymbol{p}_{-1}$ to $\boldsymbol{p}_0$ is written as $W^U[\boldsymbol{p}_{-1}, \boldsymbol{p}_0]$. To construct the trellis we iterate the unstable fundamental segment $W^U[\boldsymbol{p}_{-1}, \boldsymbol{p}_0]$ in fig. 2.4 forward twice. This produces the trellis in fig. 2.5.

HLD uses the information contained in the trellis to predict the minimal forced topology of the full tangle. HLD produces a set of symbolic equations that in turn can be represented as the transition graph in fig. 2.2. The symbolic graph can be converted into a Markov transition matrix. From the transition matrix we can extract the *topological entropy* of the trellis. One way to view the topological entropy is as a quantitative measure of the complexity of the system. It also describes the exponential stretching rate of a material line in a fluid. In HLD topological entropy represents the exponential growth of the number of symbols in the symbolic equations. For example, a single iteration of a_2 in fig. 2.2 produces three symbols, two $\boldsymbol{f}$ and one $\boldsymbol{u}_0$. Two iterates produces seven symbols and three iterates of a_2 produces fifteen symbols. Topological entropy acts a measure of this

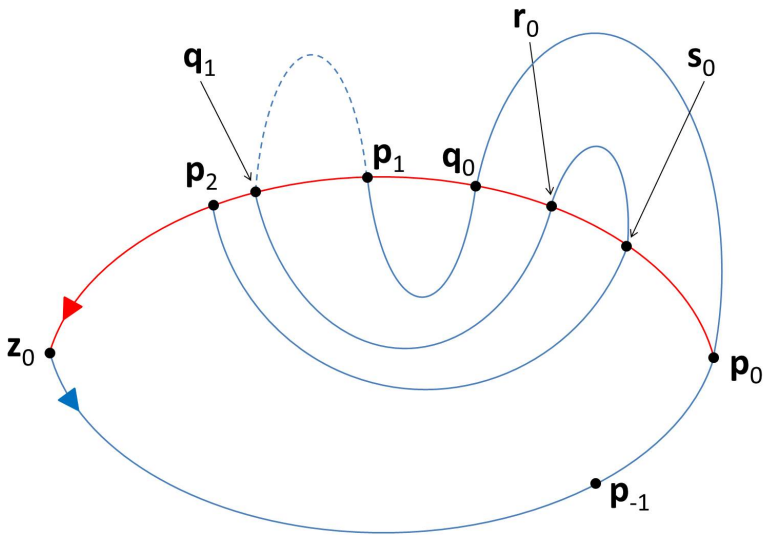

Figure 2.5: The stable (red) and unstable (blue) manifolds up to the pip $\boldsymbol{p}_0$ and the two forward iterates of the fundamental segment $W^U[\boldsymbol{p}_{-1}, \boldsymbol{p}_0]$ that forms the trellis for the complete horseshoe.

kind of growth. The topological entropy is computed by taking the natural log of largest eigenvalue of the transition matrix [49].

2.1.1 The Complete Horseshoe

We begin the discussion of HLD with the basic map known as the complete horseshoe. This system is relatively easy to apply HLD to and has a topological entropy of $\ln(2)$. *Topological entropy* measures of the complexity of a dynamical system with a higher topological entropy corresponding to more complex systems.

We construct the trellis of the complete horseshoe using the techniques outline in section 2.1. This results in the trellis in fig. 2.5. After only two iterates we see a number of intersections between the stable and unstable manifolds. We use the intersections to divide the stable and unstable manifolds up into segments known as *bridges*. A bridge is a segment of the unstable or stable manifold from one intersection to the next. For example, the segment $W^U[\boldsymbol{p}_0, \boldsymbol{q}_0]$ is a bridge; the segment $W^U[\boldsymbol{p}_0, \boldsymbol{p}_1]$ is made up of two bridges $W^U[\boldsymbol{p}_0, \boldsymbol{q}_0]$ and $W^U[\boldsymbol{q}_0, \boldsymbol{p}_1]$ but is

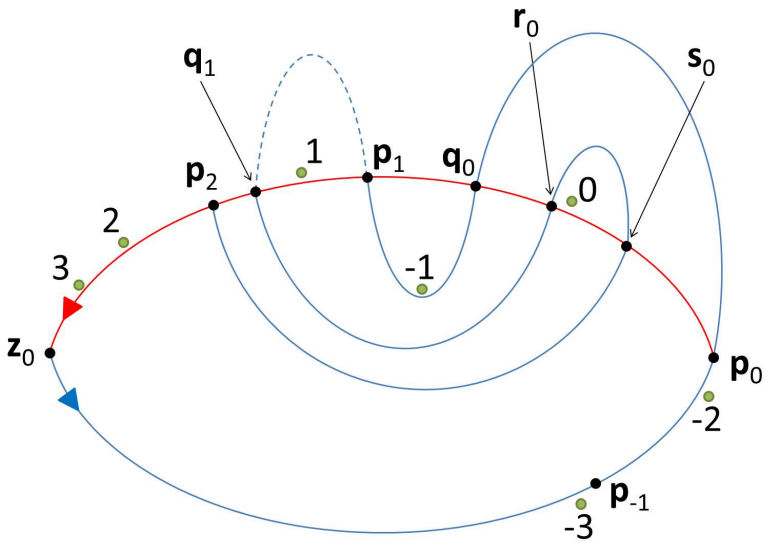

Figure 2.6: Holes are placed such that the topology of the manifolds is enforced. The initial hole is placed between $\boldsymbol{r}_0$ and $\boldsymbol{s}_0$ and labeled with a 0. The hole is also iterated forward and backward as shown.

not a bridge itself.

Next we want to place *holes* to act as barriers holding up the topology of the map. One could imagine the holes to be rods extending in the z-axis preventing any bridges from being pulled through the apart such that they eliminate intersections. Each hole placed will have a bi-infinite set of forward and backward iterates. Our goal is to place the minimal number of holes needed to enforce the topology. In this case, we need to place only one hole. This hole is located exterior to the resonance zone between the points $\boldsymbol{s}_0$ and $\boldsymbol{r}_0$, and is placed infinitesimally away from one of the two points ($\boldsymbol{r}_0$). The backward iterate of this hole lies between $\boldsymbol{p}_1$ and $\boldsymbol{q}_0$ and further backward iterates lie along the exterior of the unstable manifold below the x-axis. The forward iterate of the hole is exterior to the stable manifold marching toward the fixed point $\boldsymbol{z}_0$ as in fig. 2.6.

Once the holes are placed we identify the distinct *bridge classes* that the system is made of. Bridge classes are the set of bridges of the same homotopy class and are considered topologically equivalent. The bridge classes are defined by the

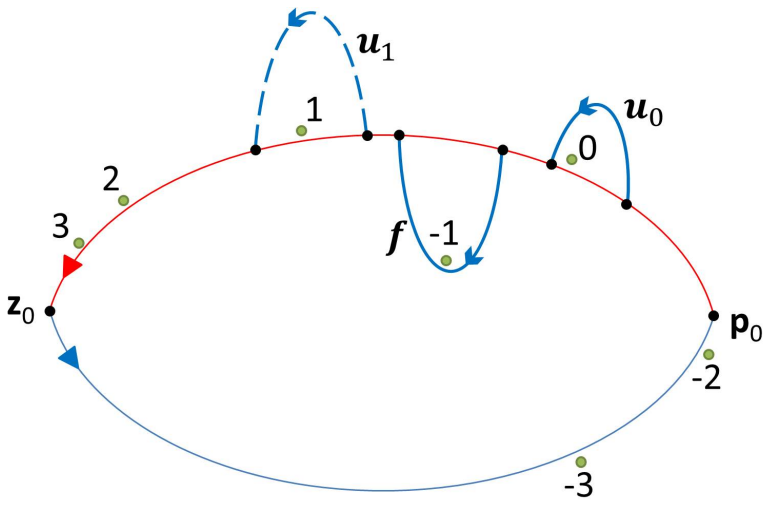

Figure 2.7: The set of bridge classes that make up the complete horseshoe. Barbed arrows indicate the direction of the bridge class while solid arrows indicate the forward time direction of the manifold. Each bridge class is defined by the holes it encloses between itself and the stable manifold. Bridge class $\boldsymbol{f}$ encloses only hole -1. All bridges that enclose only hole -1 are of bridge class $\boldsymbol{f}$. The same for hole 0 and bridge class $\boldsymbol{u}_0$, and hole 1 and bridge class $\boldsymbol{u}_1$.

way they wind around the holes. For example, bridge class $\boldsymbol{f}$ in fig. 2.7 encloses hole -1 between itself and stable manifold. All bridges in the trellis that enclose only hole -1 are of bridge class $\boldsymbol{f}$. The set of all bridge classes make up the symbolic dynamics of the system. The forward iterate of one bridge class is the concatenation of any number of other bridge classes. To identify the bridge classes group together the bridges that wind about holes in the same way. Each bridge class has a direction, represented by a barbed arrow, which is not necessarily in the same direction of the manifold, which is represented by a solid arrow. For example the bridges $W^U[\boldsymbol{r}_0, \boldsymbol{s}_0]$ and $W^U[\boldsymbol{p}_0, \boldsymbol{q}_0]$ both enclose the 0 green hole. They are both of bridge class $\boldsymbol{u}_0$ in fig. 2.7. Class $\boldsymbol{f}$ encloses the -1 green hole while class $\boldsymbol{u}_1$ encloses the green hole labeled 1.

In HLD each bridge class is iterated forward. The result is a concatenation of bridge classes. For example, the forward iterate of the bridge $W^U[\boldsymbol{p}_0, \boldsymbol{q}_0]$, of

bridge class $\boldsymbol{u}_0$, is $W^U[\boldsymbol{p}_1, \boldsymbol{q}_1]$, of bridge class $\boldsymbol{u}_1$. $\boldsymbol{u}_0$ and $\boldsymbol{u}_1$ are what are known as *inert bridge classes*. Inert bridge classes are bridge classes who iterate only to a single bridge class for all iterates. In this case, the bridge classes $\boldsymbol{u}_n$ march in sequence along the stable manifold to the fixed point. We consider inert bridge classes trivial as they do not contribute to the topological entropy of the system.

To identify the forward iterate of $\boldsymbol{f}$ we examine how the bridge $W^U[\boldsymbol{p}_1, \boldsymbol{q}_0]$, which is of class $\boldsymbol{f}$, iterates forward. Its forward iterate is $W^U[\boldsymbol{p}_2, \boldsymbol{q}_1]$. Comparing fig. 2.6 to fig. 2.7, we see $W^U[\boldsymbol{p}_2, \boldsymbol{q}_1]$ in fig. 2.6 is made up of a concatenation of the bridge classes $\boldsymbol{f}$, $\boldsymbol{u}_0$, and $\boldsymbol{f}^{-1}$ in fig. 2.7. The inverse of bridge class indicates a bridge class in the opposite direction. So we have:

$$M(\boldsymbol{f}) = \boldsymbol{f}^{-1}\boldsymbol{u}_0^{-1}\boldsymbol{f} \tag{2.1}$$

$\boldsymbol{f}$ is referred to as an active bridge class since at least one iterate of $\boldsymbol{f}$ produces more than one bridge.

Using the forward iterate of the bridge classes we construct the transition matrix and calculate the topological entropy. The transition matrix is constructed such that each row represents an active bridge class and each column represents a bridge class (thus we have an $n \times n$ matrix). Each element t_{mn} represents the number of copies bridge of n produced by iterated m forward. In this simple case we have only one active bridge class, $\boldsymbol{f}$ whose forward iterate has two copies of itself (and the inert bridge class $\boldsymbol{u}_0$, which we don't include in the matrix) resulting in the 1x1 matrix $T = (2)$. The topological entropy is the natural log of the largest eigenvalue. In this case, we have only the single eigenvalue $\lambda = 2$, which gives a topological entropy of $h = \ln(2)$. With the symbolic equations from HLD we understand the minimal topological forcing in the system.

For a simple map like the complete horseshoe the technique is fairly easy to apply. However, for a more complex trellis it is better to have a straightforward algorithm to follow. This algorithm is explored in depth in work published by Bryan Maelfeyt, Spencer Smith, and Kevin Mitchell [43].

2.2 3D Homotopic Lobe Dyanmics

The next logical step for HLD is to extend it to three dimensional systems. In 3D systems there are additional complexities that need to be accounted for but the same basic techniques will work. In 3D phase each hyperbolic fixed point will have three eigenvectors, two stable and one unstable (SSU), or two unstable and one stable (SUU). To apply HLD to a 3D map a 2D stable and 2D unstable manifolds need to intersect. Since the manifolds are 2D surfaces the intersection will be a 1D curve instead of a point. This is one of the major differences between 2D and 3D HLD. In 2D we look for the primary intersection point to define our resonance zone; in 3D we get a *primary intersection curve*. The primary intersection curve must also be a *equatorial intersection curve* in that it encloses the fixed point of the stable and unstable manifolds. In some systems intersection curves will extend from one fixed point to the other. These are *pole-to-pole intersection curves*. To apply HLD to pole-to-pole intersection curves we need to consider things slightly differently. This is explored in depth in chapter 5. Cases with equatorial intersection curves produce well defined resonance zones while cases with pole-to-pole intersection curves do not produce a well-defined resonance zone. When there is an equatorial intersection the resonance zone is formed by the stable and unstable "caps". The second key difference is that unlike in 2D, where any intersection between the stable and unstable manifolds means a resonance zone will form, in 3D intersections between the 2D stable and unstable manifolds do not force a well defined resonance zone.

As the manifolds grow they will continue to intersect with each other as in 2D dynamics; however, the intersections are generically intersection curves (in some rare cases the manifolds intersect at a tangency point), which we call boundary curves. Bridges in 2D are simple curves from one intersection point to another. In 2D each bridge had exactly two intersection points that defined. In 3D the bridges are no longer constrained to pairs of intersections. In fig. 2.8 we see a series of different types of bridges with different numbers boundary curves. Additionally, there is a distinction between bridges with the same number of intersection curves depending on the placement of the intersection curves relative to each other. For

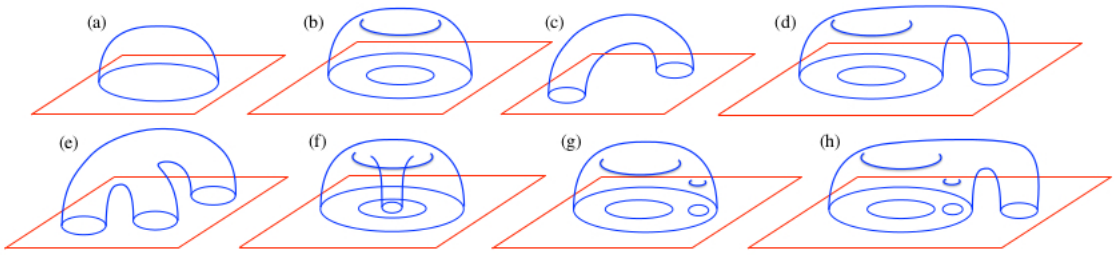

Figure 2.8: Different types of 2D bridges. (a) cap (b) bundt cake (c) macaroni (d)-(g) are tridges, different by how their boundary curves are nested. (h) an example of a bridge with four boundary curves [43].

example the bridge in fig. 2.8b is distinctly different then the bridge in fig. 2.8c even though they have the same number of boundary curves. In fig. 2.8b the intersection curves are nested so the bridge forms what we call a "bundt cake". In fig. 2.8c the not nested so the bridge forms a "macaroni" shape. Bridges are defined strictly by their intersection curves and the number and placement of boundary curves is one of the key differences between 2D and 3D HLD. In 2D we had only bridge classes, in 3D we have another homotopy class called *boundary classes*. Boundary classes are sets of boundary curves that are topologically equivalent. Thus the bridge classes of our symbolic dynamics are uniquely defined by the set of boundary classes that make up the bridge class. In 2D we identified bridge classes by a single symbol, in 3D we identify each boundary class with a single symbol and each bridge class with set of boundary class symbols that make up the bridge class. An arbitrary example could be two boundary classes A, and C could make up the single bridge class $[\![A, A, B]\!]$, that is the bridge class $[\![A, A, B]\!]$ has three boundary curves two of class A and one of class B. We represent the bridge classes in "barbell" notation where each "bell" is a boundary class and the "bar" represents the unstable manifold that connects the boundaries. An example of a set of bridge classes that could make up a trellis is seen in fig. 2.9. In fig. 2.9 the bridges are divided into bridges interior to the resonance zone (inner bridges) and bridges exterior to the resonance zone (outer bridges). Inner and outer bridges

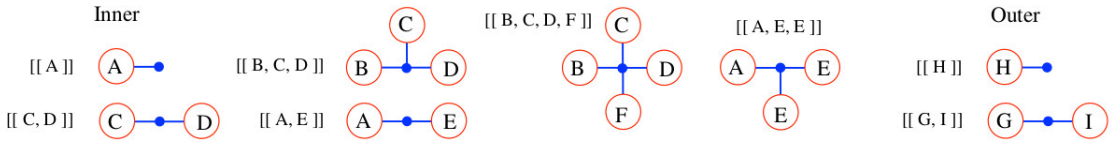

Figure 2.9: An example set of bridge classes to make up a trellis. Each "bell" represents a boundary class that is part of the bridge class while each "bar" is the manifold connecting the boundary classes together [43].

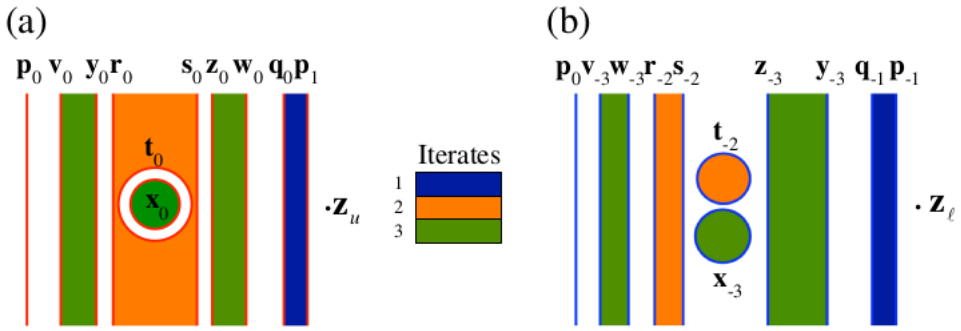

Figure 2.10: (a) the backward time ETP for a 3D system. (b) the forward time ETP [43]. The top and bottom of the ETP are identified with each other.

have their own distinct set of inner and outer boundary classes. Bridge classes are concatenated together by the boundary classes across the stable manifold.

In 2D we used the fundamental segment to define our trellis, but in 3D we use a fundamental annulus. In 2D a fundamental segment is defined as the points on the manifold from one point to its iterate. In 3D the fundamental annulus is defined as the points on the manifold from one closed curve to its iterate. The iterate of the closed curve $M(\mathcal{C})$ used to define the fundamental annulus must not intersect with the original closed curve $\mathcal{C}$. The manifolds up to the primary intersection are thus defined by only a single boundary curve $\boldsymbol{p}_0$ and so form a pair of caps, which we write as $W^U[\boldsymbol{p}_0]$ and $W^S[\boldsymbol{p}_0]$. Like in 2D when constructing the trellis we use the fundamental annulus $W^U[\boldsymbol{p}_{-1}, \boldsymbol{p}_0]$.

One of the difficulties in 3D dynamics is obtaining the manifolds numerically.

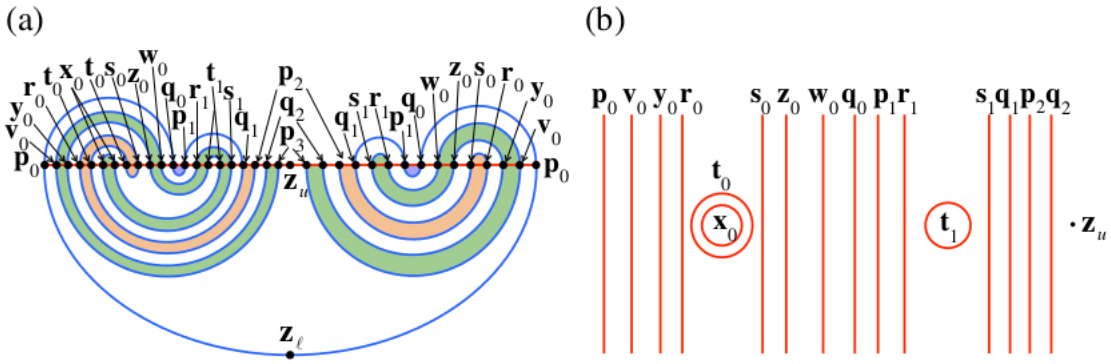

Figure 2.11: (a) A profile view of the trellis sliced down the "middle" (b) A top down view of the stable cap and the intersections in (a) [43].

In 2D systems the manifolds are 1D curves and can be generated numerically with good accuracy and short run times, 2D manifolds are necessarily more computational intensive. One alternative is to generate the forward and backward *escape-time plot* (ETP) first, and then use the ETP to create the trellis geometrically. The ETP is plot of points on the fundamental domain versus the number of iterates before the point leaves the resonance zone. In 2D the ETP is measure of the number of iterates it takes for a length of the fundamental segment to move from inside to outside the resonance zone. In 3D this is a measure of how many iterates it takes for a region of the fundamental annulus to move from inside to outside the resonance zone. The ETP is directly tied to the trellis and so a well computed ETP can be used to reconstruct the trellis. The details of how to numerically generate an ETP are discussed in Section 2.3. In fig. 2.10 shows sample backward and forward ETPs for a fully 3D "toy model". The boundaries between escaped and unescaped domains in the ETP are the intersections on the manifold. The boundaries of the backward ETP are the intersections that appear on the stable cap. We use the forward ETP to connect the boundaries on the stable cap together with the unstable manifold. The ETP in Fig. 2.10 gives rise to the trellis shown in Fig. 2.11.

To extract the trellis from the information in the ETP we begin with the stable and unstable caps up to the primary intersection $\boldsymbol{p}_0$. Fig. 2.10a shows

how the boundaries are located on the stable fundamental annulus $W^S[\boldsymbol{p}_0, \boldsymbol{p}_1]$. To determine how the unstable manifold connects to the boundary curves on the stable cap we use the forward ETP in fig. 2.10b. To identify bridges in the first iterate of the unstable fundamental annulus we consider only the first iterate *escape domains*, i.e., points in the forward ETP that have escaped after one iterate. The boundaries of the forward ETP correspond to boundaries on the unstable fundamental annulus $W^U[\boldsymbol{p}_{-1}, \boldsymbol{p}_0]$, therefore $\boldsymbol{p}_{-1}$ is connected to $\boldsymbol{q}_{-1}$ by the unstable manifold. The region between $\boldsymbol{p}_{-1}$ to $\boldsymbol{q}_{-1}$ is an escape domain, and so the bridge that connects them is exterior to the stable cap. No line drawn from $\boldsymbol{p}_{-1}$ can touch another boundary and so we know the entire bridge must extend from $\boldsymbol{p}_0$ to $\boldsymbol{q}_0$. Since the boundaries are nested on the stable cap the resultant bridge must be a "bundt cake". When constructing a particular iterate we ignore all boundaries of higher iterate escape domains. If we ignore all higher iterate boundaries the only other boundary class left is $\boldsymbol{p}_0$. A line can be drawn from $\boldsymbol{p}_0$ to $\boldsymbol{q}_{-1}$ in the forward ETP so the unstable manifold must connect $\boldsymbol{p}_1$ to $\boldsymbol{q}_0$ on the stable cap. This bridge must be inside the resonance zone since the region bounded by $\boldsymbol{p}_0$ and $\boldsymbol{q}_{-1}$ has not escaped after one iterate. We repeat this process for iterates two and three to get the full trellis as seen in fig. 2.11.

In 2D we placed 0-dimensional holes to enforce the topology of the trellis. In 3D our 0-dimensional holes become 1-dimensional "obstruction rings" which act to hold up the bridges of the trellis. Like holes each obstruction ring has a bi-infinite set of forward and backward iterates. In 3D we place the minimal number of obstruction rings such that the rings (and their iterates) act to enforce the topology of the map. Once the obstruction rings are placed we define the boundary classes. We then define the bridge classes using the boundary classes. As in 2D the bridge classes of a 3D map will form the symbolic dynamics.

Identifying the forward iterate of each bridge class in 3D is more difficult than in 2D but still based on the same idea. In 2D bridges were connected by concatenating the intersection points on the stable manifold. In 3D we concatenate bridges together by the boundary curves on the stable manifold. Finding the forward iterates of each bridge class requires us to move between other bridges. The forward

Figure 2.12: Forward iterate of bridge class [[A]]. Each "bell" represents a boundary class. Bells stuck together are where a bridge classes connects to the next through the stable manifold.

iterate of bridge [[A]] from Fig. 2.9 is seen in Fig. 2.12. Each boundary class (the bell part of the barbell structure) is connected to another boundary class for a bridge on the opposite side of the stable manifold.

In 2D the forward iterate of each bridge grows only linearly, but in 3D bridges are free to grow in two dimensions making the forward iterations more complex. When iterating a bridge class forward it is important to determine only the forced set of bridge classes and associated boundary classes. The algorithm for properly applying HLD to a 3D system was initially explored in depth by Bryan Maelfeyt, Spencer Smith, and Kevin Mitchell [43]. We analyze an example of 3D HLD with a well defined resonance zone in sec. 5.2.

Like in 2D the bridge classes and their forward iterates are the symbolic dynamics that make up the map. We take this set of symbolic dynamics and extract a lower bound of the topological entropy of the map by creating the transition matrix the same was we do in 2D. In 3D the transition matrix for the bridge classes that make trellis will give a lower bound on the 2D topological entropy. 2D topological entropy represents a 2D stretching of the manifold. This can be visualized by imagining a rubber sheet that is being pulled from its corners and stretched along both its axes. In 3D there is also a 1D stretching like a rubber band being pulled in only one direction the details of which are explored by Bryan Maelfeyt, Spencer Smith, and Kevin Mitchell [43].

2.3 Computation of the Escape Time Plots

Since computation of the trellis is computationally intensive we instead numerically computer the ETPs then construct the trellis from the ETP as in Section 2.2.

ETPs are created by taking the fundamental annulus $W^U[\boldsymbol{p}_{-1}, \boldsymbol{p}_0]$ and iterating it forward noting the number of iterates it takes for each point on the annulus to escape the resonance zone. To calculate the ETP we start with a small annular disk with a uniformly random seeding of points centered at the hyperbolic fixed point and in the plane of the two stable or unstable eigenvectors. The points of this disk are iterated forward until they have escaped the resonance zone. Higher point density will result in more detailed ETPs. It is particularly important to us to get highly accurate boundaries of the escape domains. To do this we created an algorithmic way to add new points to regions of poor resolution while not wasting computational power on well resolved regions. Generating a single iterate of the ETP follows a four step algorithm:

1. Generate an initial seed of points, construct a delaunay triangulation to connect the points and then iterate the points forward until they escape the resonance zone (or reach a user defined maximum number of iterates).

2. Refine the boundaries of the ETP based on topological properties of the triangulation that makes up the boundaries.

3. Refine the boundaries of the ETP based on angular properties of the boundary triangles.

4. Refine the ETP by shrinking the size of the boundary triangles.

The steps and results of each successive refinement of the algorithm are be seen in fig. 2.13a-d. The algorithm is designed to resolve escape domains for a single iterate at a time, building a nested set of data for each iterate.

When creating a numerical plot we always define the maximum iterate that any point will be iterated to. Generally when starting a new ETP the maximum iterate is set to 1. If a point has reached the maximum iterate before exiting the resonance zone it belongs to a region known as a *gap*.

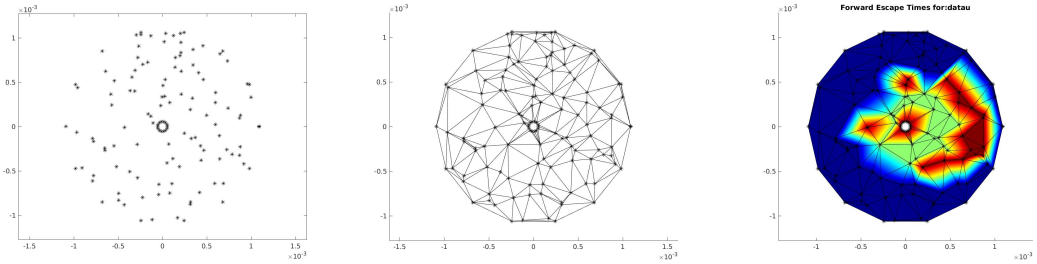

(a) Progression of the ETP during the initial seeding and iteration.

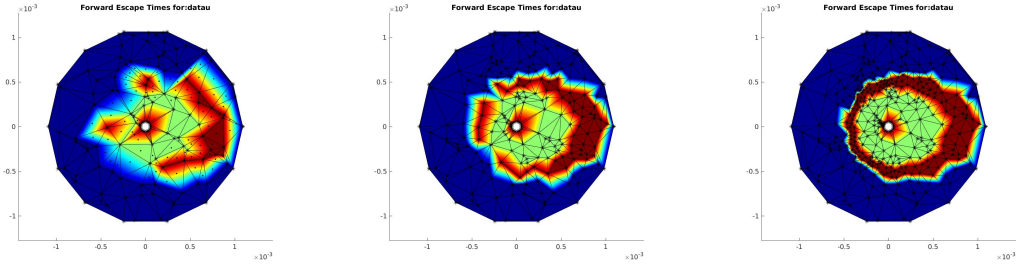

(b) Progression of the ETP during topological refinement.

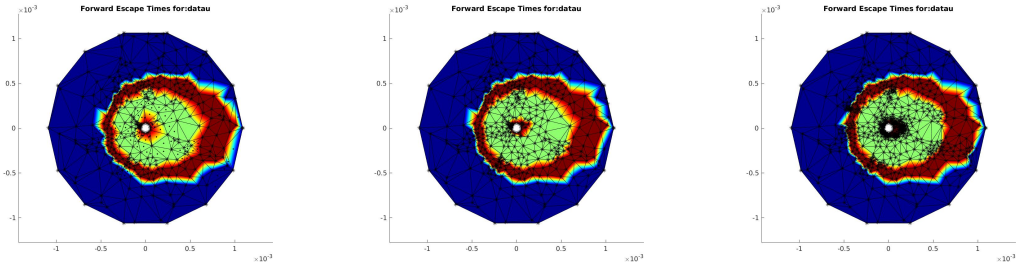

(c) Progression of the ETP during angular refinement.

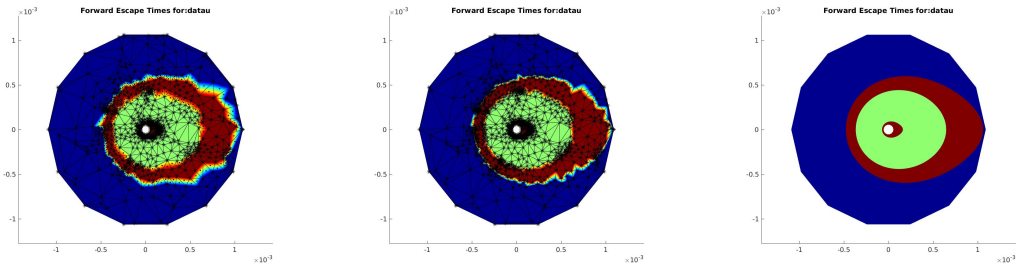

(d) Progression of the ETP during boundary shrinking.

Figure 2.13: Progression of the ETP after successive refinements of its points. Red regions are points that have not yet exited the resonance zone while blue and green are points that have exited the resonance zone at different iterates

For a new ETP we seed an initial annulus near the fixed point with uniformly random points ranging from r_{min} to $\lambda r_{min} < r_{max} < \lambda^2 r_{min}$ with λ being the largest eigenvalue at the fixed point. In addition we want to place points around the circumference of the circles with r_{min} and r_{max} which act as constraints for the delaunay triangulation. An example initial seed is seen in the left most graph of 2.13a. The points are defined by two sets of coordinates, first in three dimensional phase space, and second as their two dimensional position on the annulus. The points in phase space are iterated forward and change after every iterate. The position on the annulus will not change iterate to iterate.

Once the initial seed is created we want to link the points together so as to topologically describe the way they iterate forward. To do so we use a delaunay triangulation. Each point is attached to a number of other points forming a triangulation of all points. When performing the delaunay triangulation we enforce the constraint that the points placed along the circumference of r_{min} and r_{max} share an edge with the points immediately adjacent to them on the circumference. An example of a delaunay triangulation is seen in the middle image of Fig. 2.13a.

Once the points have been generated and the triangulation constructed we iterate each point in phase space forward until they exit the resonance zone or have been iterated user defined maximum number of iterates. This produces the result on the right of Fig. 2.13a. The plot can be divided up into three different types of regions. First we have *escape domains*, which points that are connected by the triangulation, have the same number of iterates, and have escaped the resonance zone i.e. have been iterated less than the maximum allowed number of iterations. Second are the gaps, points connected by the triangulation who have reached the maximum number of allowed iterations but not yet escaped the resonance zone. Finally we have the boundary triangles, which are triangles with at least two vertices of different iterate number. The true boundaries of the ETP will exist somewhere within the area defined by the boundary triangles. Boundary triangles typically have a combination of non-crossing edges (NCE), edges whose vertices have the same iterate number, and crossing edges (CE), edges whose vertices have different iterate numbers. The true boundary between a gap and escape domain

necessarily intersects the crossing edges. In order to construct the trellis we need to accurately identify boundaries in the backward-time ETP that map forward to boundaries in the forward-time ETP. This means that we need to accurately compute the boundary curves.

Our goal is to refine the boundary triangles and triangles near the boundary so that we are confident we have isolated the true path of the boundary curve. The first step of this process is a topological refinement of the boundaries. To do so we first have to identify "bad" triangles that violate certain topological requirements, namely:

1. Boundary triangles with a vertex that belongs to zero NCEs.
2. Boundary triangles with a vertex that is the vertex of more than two NCE.
3. Boundary triangles whose NCE is also the NCE of another boundary triangle.

Bad triangles, and any other triangle that shares an edge with a bad triangle are refined by placing a new point at the center of the triangle. An example of triangles with bad topology that need refinement and the new points they give rise to are seen in the left most image of Fig. 2.13b. These new points are then iterated forward until they exit the resonance zone or reach the maximum iterate as was done for the initial seed. The the delaunay triangulation is updated to include the new points. This results in the middle image in Fig. 2.13b. We repeat this topological refinement until all topologically bad triangles have been eliminated as in the rightmost image of Fig. 2.13b.

Completion of the topological refinement will increase the accuracy of our numerical boundaries, but there are still flaws. One major flaw is that two points that have not yet exited could be connected by an edge that crosses two boundary curves, or even a boundary curve that has looped back on itself. Our topological conditions would be satisfied, and yet we would see two unconnected escape domains that are actually part of the same escape domain. To resolve this issue we also perform an angular refinement.

After the topological refinement is complete each vertex of a boundary triangle will be attached to exactly two NCEs. For an accurate computation the angle

formed by the NCEs that share a vertex should be close to 180°. To make things more efficient we instead use the average of the angles made at each boundary triangle vertex and n adjacent vertices. If the average at the vertex is beyond a user defined tolerance we refine the triangles that includes the "bad" vertex as well all triangles that share an edge with the "bad" triangles. In the left image of Fig. 2.13c we see the new points that are added to the center of these triangles while the middle image of Fig. 2.13c is the refined ETP. We then perform the topological refinement on the updated ETP until all topologically poor triangles are eliminated, then repeat the angular refinement. We repeat this until all topologically bad triangles and all points with extreme angles are eliminated as seen in the right image of Fig. 2.13c.

At this point we have accurately identified the escape domains and gaps as seen in the right image of Fig. 2.13c. However not only are large boundary regions visually unappealing, but are poor approximations of the true boundary curve. Large boundaries also make it harder to accurately match the boundaries of backward and forward ETPs, especially when working with large number of iterates where the boundaries tend to be very close to each other. To shrink the size of these boundaries we identify all CEs whose Euclidean length on the fundamental annulus is greater than our tolerance. Triangles which have these bad CEs are refined by placing a new point at the center as seen in the left and middle images of Fig. 2.13d. We repeat the shrinking algorithm until all CEs are below our tolerance, then run the topological and angular refinements to remove all other bad triangles. The right image in Fig. 2.13d shows what an ETP will look like after all three algorithms have been completed. We see that there are three distinct regions, two that have escaped after different iterates separated by one gap (in red). The boundary triangles that separate these regions have been shrunk to the point where they are visually unidentifiable unlike the previous images.

The delaunay triangulation allows us to identify connected components using graph theory. The connected components are the distinct regions of the ETP. Points of the same iterate number that are connected by edges are broken into separate regions. The iterate number of these regions will determine if they are

gaps or escape domains. We take the points of a region and their associated data and create a new structure containing this information. For gaps this is particularly useful as we use the points of the gap as our initial seed for the algorithm. By increasing the maximum iterate by one and iterating every point in a gap forward once we find the escape domains for one iterate higher. We repeat the algorithm algorithm given above to refine the new escape domains and gaps. Repeating this for each of the gaps in the previous iterate will give us the complete set of escape domains for the next iterate. This process can be repeated until we have an ETP with all the data we want or need. Additionally this allows us to isolate parts of the ETP to examine instead of computing the entire ETP at once.

In practice the algorithm has limitations. The accuracy of the boundaries are dependent on the numerical accuracy of the resonance zone. We numerically compute the manifolds for short time, enough to identify the primary intersection curve; however, the manifolds themselves are not perfectly accurate. We use an inbuilt MATLAB function to interpolate the manifolds that bound the resonance zone. Any error in our interpolation of the manifolds will result in errors in the ETP. For a finite ETP no two distinct escape domains will share a boundary, however if our interpolation of the boundary between resonance zone and the exterior region is in the true exterior region the algorithm will misidentify some points as "gaps" when they are part of the escape domain. These misidentified points will still "escape" on the next iterate, but will result in two escape domains sharing a boundary. Another issue is that regions that are very thin but exist across a large domain of x and y coordinates are hard to refine as new points will sometimes be within machine precision of older points. In cases like this the algorithm will sometimes fail or run indefinitely trying to add new points.

These limitations do not usually effect early iterates but at higher iterates the escape domains and gaps become very long and thin making accurate identification of the regions and their boundaries more susceptible to error. Overall the generation of numerical ETPs is sufficient to perform a good HLD analysis as we will see in the next chapter.

Chapter 3

The Perturbed Hill's Vortex

Our initial foray into 3D HLD used "toy models" to create simple chaotic systems to test against. However, for the theory to be truly viable, it must be applied to a numerical system. To that end we need a map with the following properties:

1. Fully chaotic.
2. Volume-preserving.
3. The map must have 2D stretching, i.e., the map must be fully 3D.
4. Have a well defined resonance zone (i.e., the stable and unstable manifolds form an equatorial intersection curve).

There are many maps that satisfy these conditions. We opted to begin with the Hill's Spherical Vortex flow, turn it into a discrete map, then perform finite transformations on it to break any symmetries. We chose the Hill's Spherical Vortex because it is a common volume-preserving physical system with a well defined resonance zone. The remaining properties can be induced using transformations.

3.1 The Perturbed Hill's Spherical Vortex

The Hill's spherical vortex is a 3-dimensional flow field with the profile in fig. 3.1. Hill's Vortex is a well known solution to the Euler Equations for an invicid

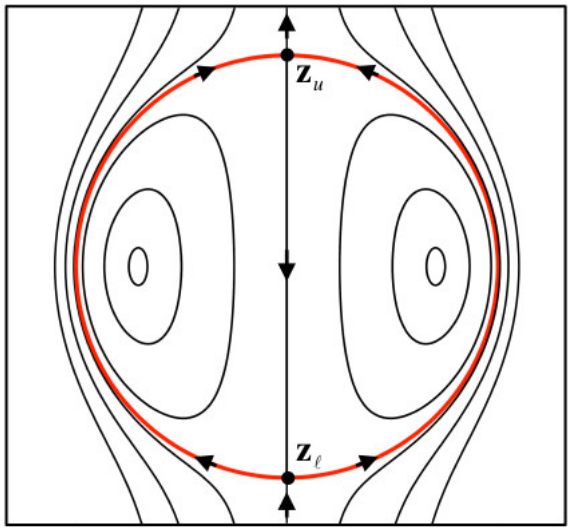

Figure 3.1: Flow for a classic Hill's Vortex [62].

incompressible fluid [3] and has the stream function [53]:

$$\psi(r,\theta) = \begin{cases} \frac{1}{2}U\left(1-\frac{a^3}{r^3}\right)r^2\sin^2\theta, & (r>a), \\ -\frac{3}{4}U\left(1-\frac{r^2}{a^2}\right)r^2\sin^2\theta, & (r<a), \end{cases} \tag{3.1}$$

where a is the vortex radius and U is the flow speed at infinity.

The flow field in cylindrical coordinates is:

$$\begin{aligned} \dot{\rho} &= -\rho^{-1}\partial\psi/\partial z \\ \dot{z} &= \rho^{-1}\partial\psi/\partial\rho \end{aligned} \tag{3.2}$$

This flow has two fixed points, $\boldsymbol{z}_u$ and $\boldsymbol{z}_\ell$ with stable and unstable manifolds that form a separatrix preventing mixing from outside the vortex. To break the separatrix and induce sufficient chaos to the system we apply a series of perturbations. First we begin with the unperturbed map H by integrating a point (x, y, z) over the time-interval $[t_i, t_f]$. We then perturb the map by composing it with a series of other maps to break particular symmetries. First we break the separatrix and induce mixing by applying the map:

$$L_z(x,y,z) = \left(x, y, z + \epsilon\left(x^2 + y^2\right)\right) \tag{3.3}$$

Next we apply a rotation about the y-axis to break the 1D separatrix formed between $\boldsymbol{z}_u$ and $\boldsymbol{z}_\ell$

$$R_y(\theta) = 2\pi\delta_y \frac{a-r}{1+r^2} \tag{3.4}$$

and finally we also applied a rotation about the z-axis:

$$R_z(\theta) = 2\pi\omega_y \frac{a-r}{1+r^2} \tag{3.5}$$

The final map M is:

$$M = R_z^{-1} \circ R_y \circ L_z \circ H \circ L_z \circ R_y \circ R_z. \tag{3.6}$$

M is thus a fully chaotic volume-preserving map with 2D stretching. M also has the property $M^{-1} = S \circ M \circ S$, where $S(x,y,z) = (x,y,-z)$, making it time reversible.

A reversible map M is defined as a map with a symmetry operator S such that $M^{-1} = S \circ M \circ S$. S must be idempotent, i.e. $S = S^{-1}$. A consequence of reversibility is that $W^S_{\boldsymbol{z}_u} = S(W^U_{\boldsymbol{z}_\ell})$. If we assume S to be linear then its eigenvalues must be either $+1$ or -1. In 3D there are only three possibilities: a single negative eigenvalue, two negative eigenvalues, or three negative eigenvalues. With appropriate rotations of phase space, we can express any S as $S(x,y,z) = (x,y,-z)$, $S(x,y,z) = (-x,y,-z)$, or $S(x,y,z) = (-x,-y,-z)$.

Consider $S(x,y,z) = (x,y,-z)$. Under this operator every point on the xy-plane is invariant under S. As a consequence of $W^S_{\boldsymbol{z}_u} = S(W^U_{\boldsymbol{z}_\ell})$, any equatorial intersection of $W^U_{\boldsymbol{z}_\ell}$ with the xy-plane must be a primary intersection curve. This symmetry is a convenient way of forcing a primary intersection curve to exist.

Now consider $S(x,y,z) = (-x,y,-z)$. In this case every point on the y-axis is invariant, and so any intersection of the y-axis by $W^U_{\boldsymbol{z}_\ell}$ results in an intersection point with $W^S_{\boldsymbol{z}_u}$. These forced intersection points generically lie on a heteroclinic intersection curve. However, this curve need not be equatorial. Thus this symmetry is convenient for exploring cases without primary intersection curves.

Finally we consider $S(x, y, z) = (-x, -y, -z)$. In this case the only invariant point under S is the origin. Systems with this symmetry operator do not generically have any forced intersection points. However, other advantages of reversibility still exist.

Reversibility produces a number of advantages when computing manifolds and applying HLD. Applying the symmetry operator to the unstable manifold produces the stable manifold and vice versa. This is desirable when computing manifolds numerically as it cuts computation time in half, and computations for 2D (and higher dimensional) manifolds can be resource intensive. A second advantage is that the forward and backward ETPs are geometrically identical, requiring only a single computation. Finally for reversible maps with a pair of hyperbolic fixed points always have one fixed point with a 2D unstable manifold and one with a 2D stable manifold. Many examples throughout this work use time-reversibility to simplify the analysis.

3.2 Scattering Data and HLD

We chose a radius $a = 1$ the time-interval to $t = [0, 1]$ and parameters $U = -1.2573$, $\epsilon = 0.75$, $\delta = 0.3$ and $\omega = 0.2$. Fig 3.2 shows the manifolds up to the primary intersection curve $\boldsymbol{p}_0$ as well as the first full iterate of the dynamics. Using this data we created an interpolation of the resonance zone which allowed us to compute the ETPs necessary to perform HLD.

Iterate 3 Dynamics

We began our HLD analysis of the perturbed Hill's vortex by using ETP data for the first three iterates. Fig. 3.3a shows the numerically calculated ETP for the first three iterates. Fig. 3.3b is a "cartoon" version of the ETP that is easier to visualize. Due to the time symmetric nature of our map the topology of the backward ETP and the forward ETP are identical. Due to reversibility we had to only compute the ETP once in order to construct the trellis since the boundaries in the forward ETP are geometrically the same in the backward ETP.

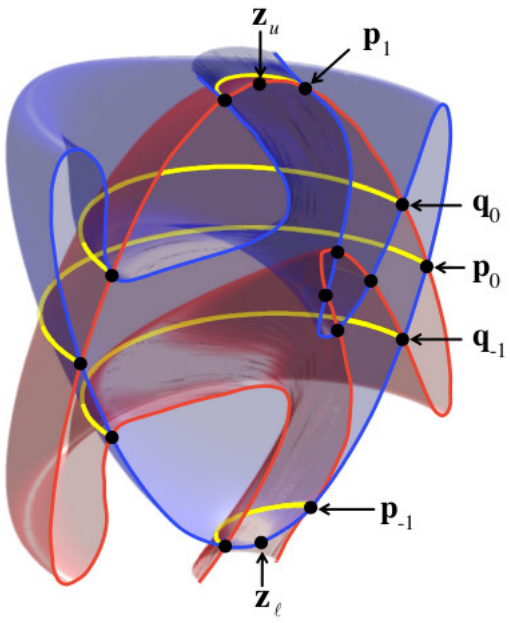

Figure 3.2: Stable and unstable manifolds for Hill's Vortex after two iterates [62].

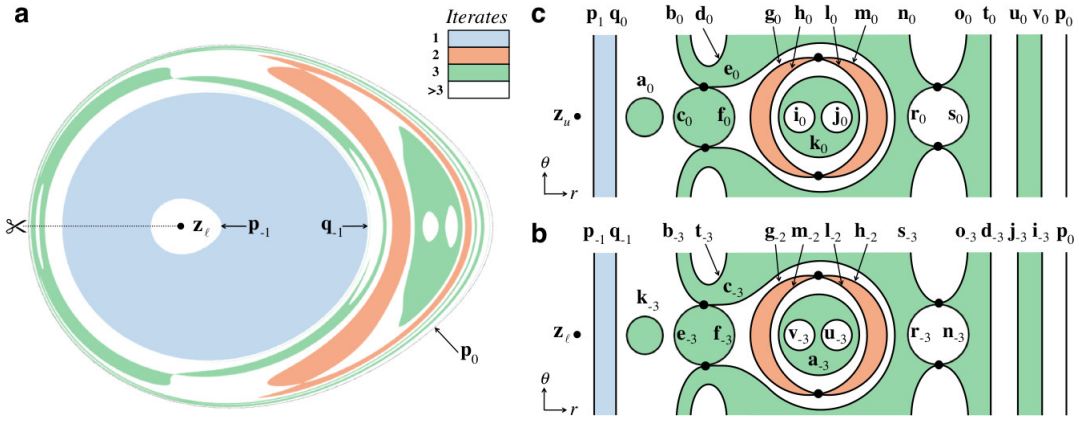

Figure 3.3: Escape time plots for a Hill's Vortex after three iterates. a) is the numerical escape time plot and b) is a "cartoon" version for better visualization [62].

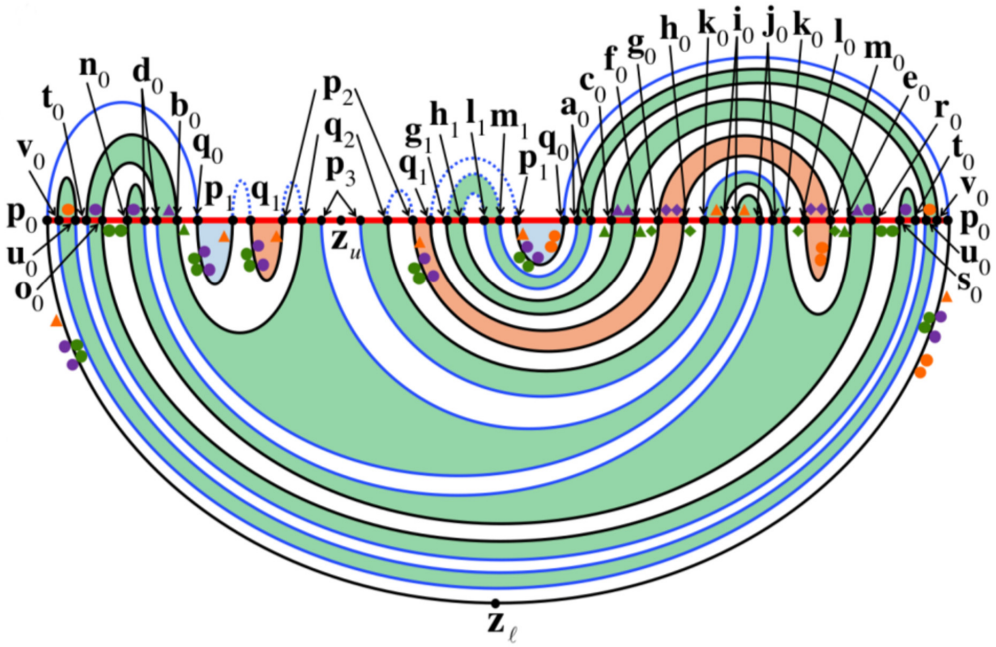

Figure 3.4: Profile view of the stable manifold and the unstable manifold up to three iterates. The trellis was constructed from the ETPs [62].

From the ETPs in fig. 3.3 we generate a profile view of the manifolds as seen in fig. 3.4. We chose obstruction rings as indicated by the colored circles, triangles, and diamonds in fig 3.4. Using Fig. 3.4 we construct our boundary classes as in fig. 3.5. Finally, we use the boundary classes to identify the complete set of bridge classes and iterate them forward. This results in the full symbolic dynamics in fig. 3.6. These dynamics only include information up to the third iterate of fundamental annulus.

In fig. 3.6 the unnumbered bridge classes are *transient* (non-recurrent under the dynamics), while the numbered classes are recurring.

From the symbolic dynamics we construct the transition graphs in fig. 3.7. The graph in fig. 3.7a shows how recurrent bridge classes iterate to new recurrent bridge classes. Fig. 3.7b is the transition graph for the 1D bridges that can be embedded in the full transition graph. For example in fig. 3.6a bridge class 1 iterates forward to bridge classes 1 and 2. Bridge Class 2 when iterated forward creates a copy of 3, and bridge class 3 when iterated forward creates a copy bridge

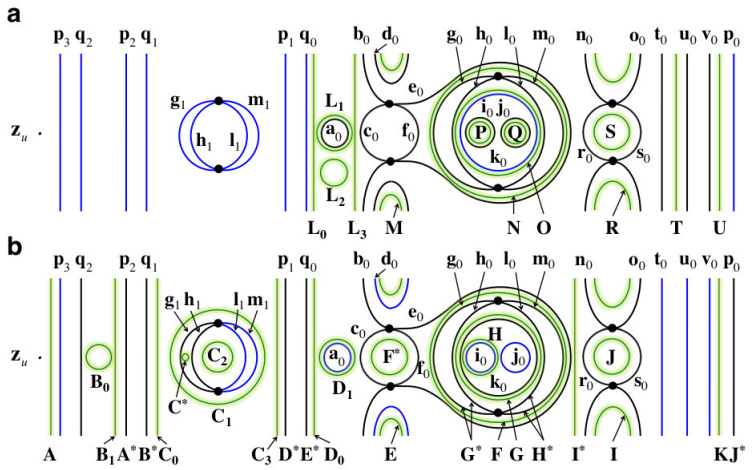

Figure 3.5: Boundary classes for the perturbed Hill's Vortex using third iterate data. a) the boundary classes describing bridge classes above the stable cap. b) the boundary classes describing bridge classes below the stable cap [62].

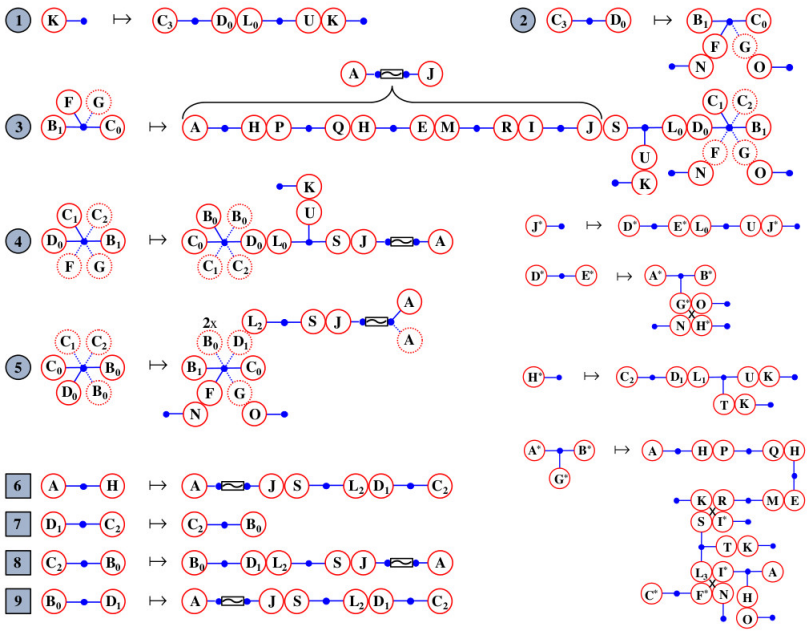

Figure 3.6: Symbolic dynamics of perturbed Hill's Vortex using information from the first three iterates [62]

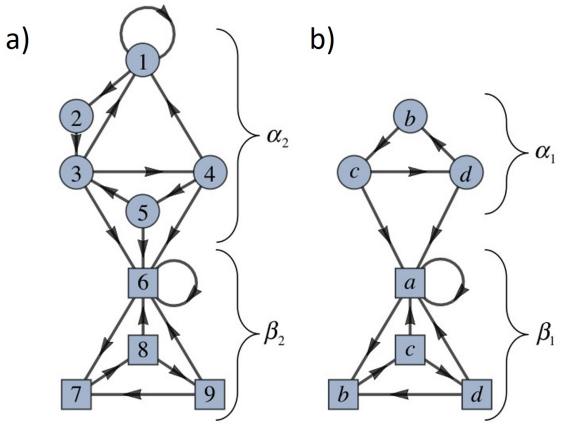

Figure 3.7: Transition graph representation of the symbolic dynamics from three iterates of the perturbed Hill's vortex [62]. a) is the transition graph of all the active bridge classes while b) is the transition graph for 1D bridges which can be embedded into the full transition graph.

classes 1, 4 and 6. One important feature of the transition graph is that the upper connected components labeled α_2 represent the 2D dynamics while the lower set of components β_2 are the 1D dynamics. Bridges in α_2 can create brides in either α_2 or β_2 however bridges in β_2 do not create bridges in α_2.

3.2.1 Iterate 4 Dynamics

We computed the fourth iterate of the map to confirm that the minimum predicted escape domains from the third iterate appear in fourth iterate. Fig. 3.8 is the numerically computed ETP and fig. 3.9 is the simplified "cartoon" ETP.

From fig. 3.9 we construct the trellis after four iterates and then derive the symbolic dynamics. Using the symbolic equations we construct the symbolic graph in fig. 3.10. Including data up to iterate four produces the bridges predicted by the third iterate symbolic equations as well as new bridges that were not predicted. In the transition graph for the fourth iterate information there is still the distinct separation between the β_2 and α_2 connected components. The bridges that appear at the fourth iterate that were not predicted by the information at the third iterate implies that the bridge classes from iterate three dynamics are not the complete set

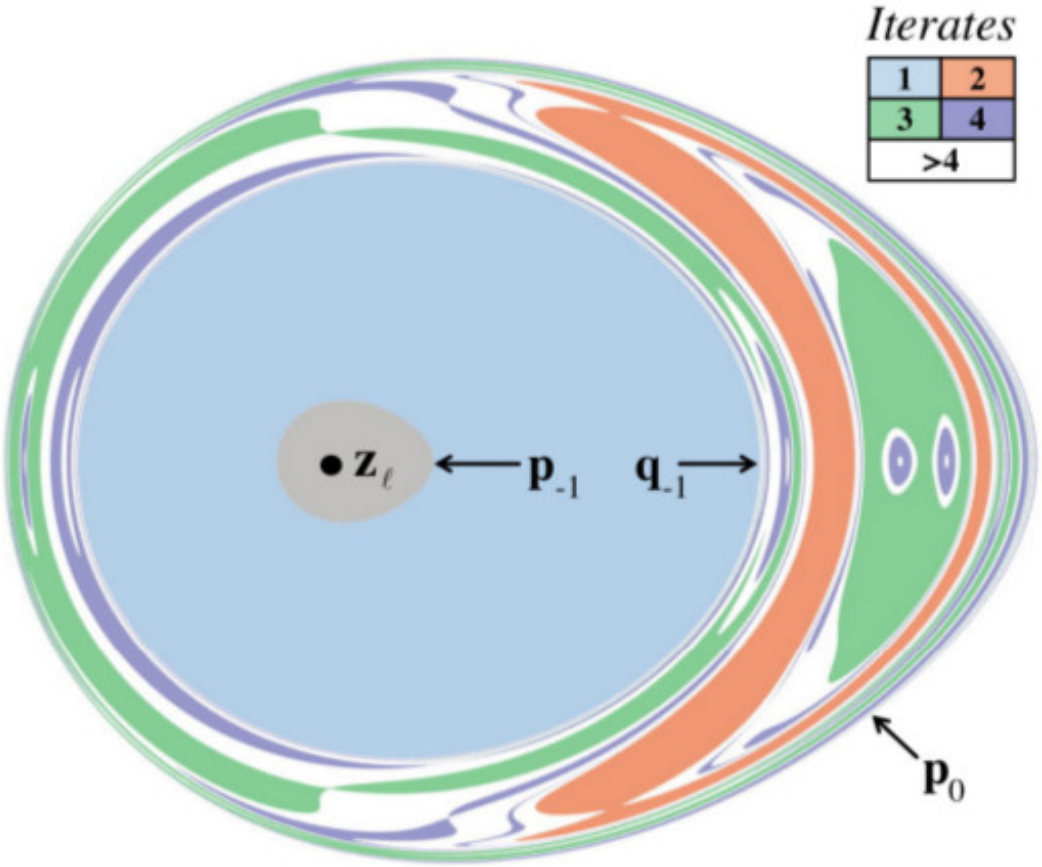

Figure 3.8: Fourth iterate numerical ETP for the Perturbed Hill's Vortex [62].

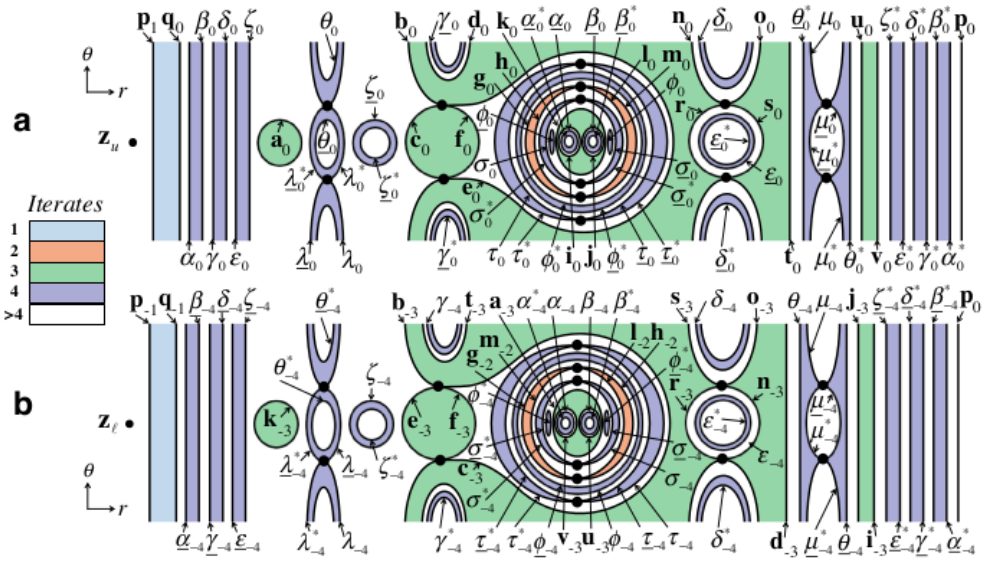

Figure 3.9: (a)The "cartoon" backward ETP with four iterates of the perturbed Hill's vortex. (b) Forward ETP for with four iterates of perturbed Hill's vortex [62].

for the tangle. When the fourth iterate data is included we get a more complete set of dynamics, though there is no guarantee that it is the complete set of dynamics for the tangle.

3.3 Topological Entropy and Stretching Rates

Topological entropy is a quantifiable way to identify the exponential growth rate of "distinguishable" trajectories with respect to time. Closely related is the topological entropy of the symbolic dynamics. To obtain a lower bound of the topological entropy we construct the transition matrix T and take the natural log of of its largest eigenvalue. Each element of the transition matrix T_{nm} is the number of copies of the bridge in column n produced when the bridge m is iterated forward. For the perturbed Hill's Vortex with three iterates of information we get,

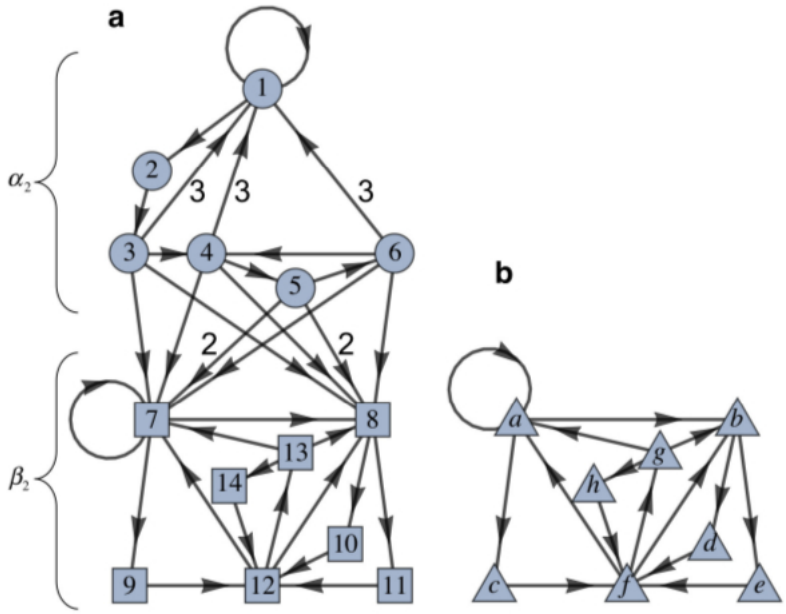

Figure 3.10: (a) The transition graph of all bridge classes that come from the fourth iterate. (b) Transition graph for 1D bridges which can be embedded into the full transition graph [62].

$$T = \begin{pmatrix} 1 & 1 & 0 & 0 & 0 & 0 & 0 & 0 & 0 \\ 0 & 0 & 1 & 0 & 0 & 0 & 0 & 0 & 0 \\ 1 & 0 & 0 & 1 & 0 & 1 & 0 & 0 & 0 \\ 1 & 0 & 0 & 0 & 1 & 1 & 0 & 0 & 0 \\ 0 & 0 & 1 & 0 & 0 & 1 & 0 & 0 & 0 \\ 0 & 0 & 0 & 0 & 0 & 1 & 1 & 0 & 0 \\ 0 & 0 & 0 & 0 & 0 & 0 & 0 & 1 & 0 \\ 0 & 0 & 0 & 0 & 0 & 1 & 0 & 0 & 1 \\ 0 & 0 & 0 & 0 & 0 & 1 & 1 & 0 & 0 \end{pmatrix} \tag{3.7}$$

which has a topological entropy of $h_{top} = \ln 1.6956$. When we include fourth iterate information the topological entropy increases to $h_{top} = \ln 2.1105$. A directly computed numerical approximation of the topological entropy for our system puts it between $ln2.7114$ and $\ln 2.8210$. If we incorporate information from higher iterates our lower bound of the topological entropy will converge on the topological entropy of the system.

Additionally we can look to the 1D dynamics of our system and calculate its topological entropy. Using the transition matrix associated with the transition graph in fig. 3.7b we get a topological entropy of $h_{top} = \ln 1.6956$ and $h_{top} = \ln 2.1105$ when using the transition graph in fig. 3.10b. These are identical to the 2D stretching rates and something we were not expecting from the system. This is a result of reversibility as bridges that are fully 2D in the forward dynamics will become 1D in the backward dynamics. Such a duality between the forward and backward time dynamics gives rise to identical 1D and 2D topological entropy.

3.4 Fractal Structure

One of the more interesting properties of chaotic systems is an inherent fractal structure that arises within them. This occurs within the dynamics of the system by repeated fractal bridge structures. While we cannot directly see the bridges of the system we do see this fractal structure in the ETPs. Two clear examples of the

fractal structures are seen in fig. 3.11. Fig 3.11a is an example 2D fractal structure while fig. 3.11b is an example of 1D fractal structure.

In particular both of the structures in fig. 3.11 are the results of a loop in the transition graph in Fig. 3.10. Fig. 3.11a shows the $1 \to 2 \to 3$ cycle of the iterate four dynamics, which repeats every third iterate. The structure for iterates $4 - 6$ is nearly identical to the structure at iterates $1 - 3$. If we look in the same region in the second image of fig. 3.11a we see the pattern repeat again for iterates $7 - 9$. The bridges represented by this cycle are fully 2D bridges as well.

Finally Fig. 3.11b shows a 1D cycle of three annular bands repeating after only one iterate. These bands represent simple 1D bridges that are the repeated 6 in Fig. 3.10. Additionally one further iterate between some of these three bands contain bridges that are unpredicted by the dynamics from information up to iterate four. These unpredicted bridges are also 1D in nature and will continue to repeat with each cycle of the fractal structure.

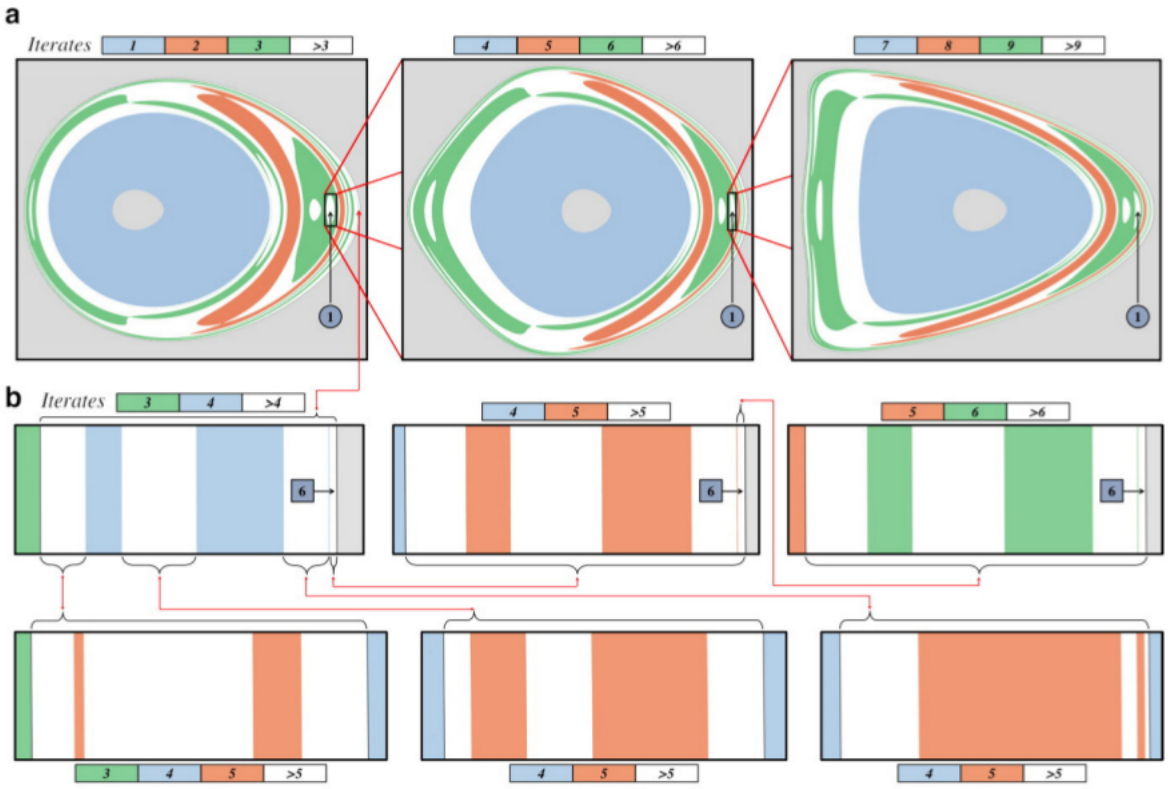

Figure 3.11: (a) An example of a 2D fractal structure as the initial three iterates are repeated every third iterate. (b) Example of a 1D structure are three annular bands are repeated every iterate. Additionally new unpredicted bands occur between the three predicted bands [62].

Chapter 4

Searching for an Analytic Map with an Equatorial Intersection Curve

Our next step was to apply HLD to an analytic 3D map. Analytic maps are more efficient to compute than flows such as the Hill's spherical vortex examined in chapter 3.1. Specifically, the increased computational efficiency of an analytic map would allow the exploration of a greater number of maps within the associated parameter space. By examining a large number of parameters we might be able to identify any hyperbolic plateaus that occur in the space. We began our explorations considering the 3D equivalent to the Hénon map.

In 2D, one of the most explored maps is the Hénon map [33]. Indeed, our group has also explored this map in depth using HLD [61]. The 2D Hénon map is defined as,

$$M = \begin{cases} x_{n+1} = 1 - kx_n^2 + y_n \\ y_{n+1} = bx_n \end{cases} \tag{4.1}$$

with k and b as constants. In cases where $b = 1$ the Hénon map is area-preserving. In addition, there are well defined ranges of k where the area-preserving map reaches a *hyperbolic plateau*. A hyperbolic plateau is a range of parameters

where the topological entropy is the same.

In 3D the equivalent to the Hénon map is the quadratic family of maps. We chose to explore this family of maps hoping to find a numerical example with a well defined resonance zone to apply HLD to. We also hoped to identify a hyperbolic plateau.

4.1 The Quadratic Family of Maps

In 3D the nearest equivalent to the Hénon map is the quadratic family of maps [39, 22, 35, 45]. The quadratic family of maps is defined as:

$$f(x,y,z) = \begin{pmatrix} x+y \\ y+z-\epsilon+\mu y+\bar{P}(x,y) \\ z-\epsilon+\mu y+\bar{P}(x,y) \end{pmatrix} \tag{4.2}$$

where $\bar{P}$ is the quadratic form

$$\bar{P}(x,y) = \bar{a}x^2 + \bar{b}xy + \bar{c}y^2. \tag{4.3}$$

We refer to this particular form of the quadratic family of maps as the *Dullin-Meiss form*. These maps are volume-preserving for all parameters. While $\bar{a}\epsilon > 0$ this form has two fixed points at

$$\boldsymbol{z}_\pm = \begin{pmatrix} x_\pm \\ 0 \\ 0 \end{pmatrix} \tag{4.4}$$

where,

$$x_\pm = \pm\sqrt{\frac{\epsilon}{\bar{a}}}. \tag{4.5}$$

When $\bar{a}\epsilon = 0$ there is a single fixed point at the origin and when $\bar{a}\epsilon < 0$ there are no fixed points. When they do occur the fixed point always occur symmetrically on the x-axis. In the volume-preserving case these fixed points are always hyperbolic and have either two stable directions and one unstable (SSU), or two unstable

directions and one stable (UUS). SSU fixed points have a 2D stable manifold and a 1D unstable manifold while UUS fixed points have a 2D unstable manifold and 1D stable manifold. There are three combinations for the two fixed points; 1) both are SSU and both have 2D stable manifolds, 2) both are UUS fixed points and both have 2D unstable manifolds, or 3) one is an SSU fixed point with a 2D stable manifold and the other UUS with a 2D unstable manifold. 3D HLD requires a transverse intersection between 2D stable and unstable manifolds and therefore we cannot apply it to cases with only two SSU or only two UUS fixed points. It is key the the chosen parameter values produce at least one SSU fixed point and one UUS fixed point.

A second form of the quadratic family of maps is be obtained using an affine change of coordinates [45]. We refer to this form of the quadratic family of maps as the *Lomelí form* and it is given as,

$$f(x,y,z) = \begin{pmatrix} \alpha + \tau + z + P(x,y) \\ x \\ y \end{pmatrix} \tag{4.6}$$

with,

$$P(x,y) = ax^2 + bxy + cy^2. \tag{4.7}$$

In this case the fixed points occur at,

$$\boldsymbol{z}_\pm = \begin{pmatrix} x_\pm \\ x_\pm \\ x_\pm \end{pmatrix} \tag{4.8}$$

where,

$$x_\pm = \frac{-\tau \pm \sqrt{\tau^2 - 4\alpha(a+b+c)}}{2(a+b+c)} \tag{4.9}$$

In the Lomelí form of the map the fixed points occur on the line $x = y = z$ but the fixed points are not symmetric across the origin. As with the Dullin-Meiss form the fixed points go through a saddle-node bifurcation when $\tau^2 - 4\alpha(a+b+c) = 0$.

Both of the forms exist in five-dimensional parameter space. The parameter space is reduced by a dimension by applying a scaling transformation to set $a + b + c = 1$ in the Lomelí form or $\bar{a} = 1$ in the Dullin-Meiss form [39]. This scaling transformation has the effect of scaling the fixed points in the Lomelí form to,

$$\boldsymbol{z}_{\pm} = \begin{pmatrix} x_{\pm} \\ x_{\pm} \\ x_{\pm} \end{pmatrix}, \; x_{\pm} = \frac{-\tau \pm \sqrt{\tau^2 - 4\alpha}}{2} \tag{4.10}$$

and the fixed points in the Dullin-Meiss form as

$$\boldsymbol{z}_{\pm} = \begin{pmatrix} \pm\sqrt{\epsilon} \\ 0 \\ 0 \end{pmatrix}. \tag{4.11}$$

We convert from the Dullin-Meiss parameters to the Lomelí parameters using,

$$\begin{aligned} a &= \bar{c} \\ b &= \bar{b} - 2\bar{c} \\ c &= \bar{c} + \bar{a} - \bar{b} \\ \tau &= \tfrac{2\bar{a}(3+\mu)}{2\bar{a}-\bar{b}} \\ \alpha &= \tfrac{(3+\mu)^2\bar{a}+\epsilon(-4\bar{a}^2+4\bar{a}\bar{b}-\bar{b}^2)}{(2\bar{a}-\bar{b})^2}. \end{aligned} \tag{4.12}$$

Converting from Lomelí parameters to Dullin-Meiss parameters is done using,

$$\begin{aligned} \bar{a} &= a + b + c \\ \bar{b} &= b + 2a \\ \bar{c} &= a \\ \mu &= \tfrac{(b+2c)\tau}{2(a+b+c)} \\ \epsilon &= \tfrac{\alpha(2\bar{a}-\bar{b})^2-(3-\mu)^2\bar{a}}{-4\bar{a}^2+4\bar{a}\bar{b}-\bar{b}^2}. \end{aligned} \tag{4.13}$$

We eliminate an additional parameter by constraining ourselves to maps with with a reversor S. For the Lomelí form reversibility occurs when $a = c$ and has the reversor,

$$S(x, y, z) = -\begin{pmatrix} z + \tau \\ y + \tau \\ x + \tau \end{pmatrix} \tag{4.14}$$

while for the Dullin-Meiss form reversibility occurs when $\bar{a} = \bar{b}$ and has the reversor,

$$S(x, y, z) = \begin{pmatrix} -x \\ y - z \\ -z \end{pmatrix}. \tag{4.15}$$

Unfortunately, eq 4.15 has two negative eigenvalues resulting in a line of invariant points under the reversor. While we cannot use the reversible map to force an equatorial intersection curve, it is still desirable as reversibility reduces the complexity of the computations and analysis, forces a pair of UUS and SSU fixed points, and reduces parameter space down to three dimensions.

4.2 Searching Parameter Space

4.2.1 The Broad Search of Parameter Space

Our goal is to find a set of parameter values where the 2D stable and unstable manifolds of the fixed points have an equatorial intersection leading to a well-defined resonance zone. Once we identify the parameters we want, we will apply HLD to construct the symbolic dynamics. If successful we plan to explore nearby parameter space to try and identify a hyperbolic plateau.

We began the exploration of parameter space by setting $\bar{a} = 1$ (to scale the map) and impose reversibility such that $\bar{a} = \bar{b} = 1$. This reduces the parameter space from five independent parameters to three, $\bar{c}$, ϵ, and μ.

We explored parameter space using a brute force method of computing the manifolds. To numerically compute the manifolds we first identified the two unstable (or two stable) eigenvectors of the lower fixed point. Sufficiently close to the fixed point, the manifold is approximated using the plane defined by the two

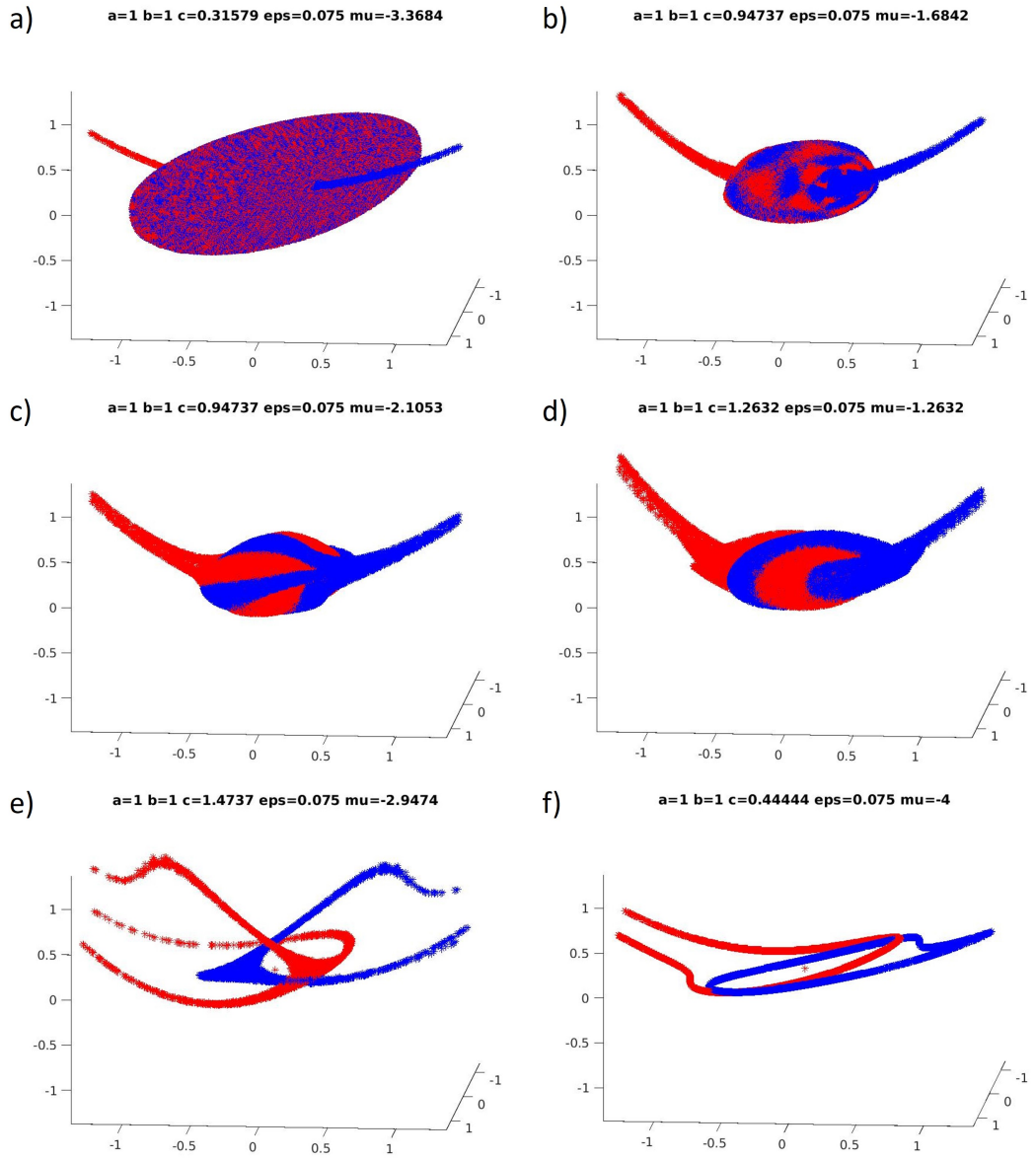

Figure 4.1: Examples of intersections between 2D stable (red) and unstable (blue) manifolds of the quadratic family of maps. a) A near-seperatrix type intersection. The manifolds appear to lie completely on top of one another. b) A bubbles type of intersections. Here small portions of the unstable manifold poke through the stable cap forming a series of bubbles. c) Wedge type intersections. Wedges of stable or unstable manifold form with intersection curves that connect extend from one fixed point to the other. d) A spiral wedge. Here the pole-to-pole intersection curves of the wedges spiral around the fixed points. e) A Non-intersecting case, or manifolds that do not appear to intersect under finite iteration. f) Degenerate manifolds. The two stable (or unstable) eigenvectors of the fixed point are degenerate leading to 1D non-intersecting manifolds.

eigenvectors. We populate a small disk (in our case, a disk of radius 10^{-5}) with a random distribution of initial points (in our case, 10^6). These points are iterated forward until reaching a set number of iterates (usually 250), or iterated beyond a sufficiently large sphere centered on the fixed points. Since we constrained ourselves to reversible maps, we obtain the stable manifold by applying the reversor to the points computed for the unstable manifold.

We plotted the resultant manifolds by simply plotting the points and their iterates as seen in fig. 4.1. Note that we maintained our convention of plotting the stable manifold using red points and the unstable manifold using blue points. Unfortunately our exploration of this large parameter space was unable to identify any cases with an equatorial intersection. We did identify many cases with non-equatorial intersections which we broke down into the six broad cases in fig. 4.1.

We call manifolds with intersections of the type seen in fig. 4.1a a *near-separatrix*. These are not true separatrices, as the manifolds are not truly the same, but they are close enough. In some cases the difference between the manifolds is sufficient to see that they have intersection curves running from the lower fixed point to the upper fixed point. In either case the systems do not have a well-defined resonance zone. In some cases (such as the fig. 4.1a) the type of intersection is not directly discernible, but minor adjustments in parameter space always lead to cases without a well-defined resonance zone. Additionally near-separatrix cases likely have many invariant tori and invariant circles in their interior as detailed in [22] which we are trying to avoid as they complicate the HLD analysis.

Fig. 4.1b shows what we categorize as a *bubbles* case. In this case the two manifolds intersect in such a way as to produce a bubbling pattern along the cap of manifold. We see portions of the stable manifold appearing beyond the unstable manifold and portions of the unstable manifold appearing beyond the stable manifold. The bubble intersections between the manifolds are always non-equatorial, but not pole-to-pole. They do not enclose a fixed point allowing the formation of a well defined resonance zone. Manifolds such as this are worth studying in the future but are beyond the scope of this project.

Fig. 4.1c and fig. 4.1d are very similar. The first is a case of *wedges* and the

second *spiral wedges*. In both cases the manifolds form lobes (which we call *wedges*) that go from a fixed point out to infinity while the intersection curves of the lobe connect one fixed point to the other. These pole-to-pole curves are periodic under the map. In some cases, each point on the pole-to-pole curve will iterate onto the same pole-to-pole intersection curve, meaning the intersection curve is invariant under the map. In other cases, a point may iterate from one pole-to-pole curve to another before being iterated back to its original curve. In both cases the point will be iterated from the unstable fixed point to the stable one. The difference between the two categories is the spiral nature of the pole-to-pole intersection curves. This difference is subtle but can have significant effects on the structure as we will see in chapter 6. Cases of the wedge category will have fixed points with real eigenvalues. We suspect that fig. 4.1c is actually a spiral wedge case whose spiral only appears close to the fixed point.

In fig. 4.1e the manifolds are *non-intersecting* manifolds. We found that even after an extremely large number of iterations of the initial annulus these manifolds never intersect. We do note that the manifolds get closer together and we suspect, but cannot confirm, that the trellis actually does intersect at the pole-to-pole curves and only at the pole-to-pole curves.

Finally, cases such as those in fig. 4.1f are *degenerate*. In these cases, the two unstable (or two stable) eigenvalues and eigenvectors are both degenerate, resulting in a 1D manifold. Fig. 4.1f likely does not have degenerate eigenvalues and eigenvectors at the fixed points, but is sufficiently close to those values.

When moving through parameter space we noticed that the manifolds would change between the different cases. Fig. 4.2 shows an example of how decreasing μ results in manifolds switching between different cases. Fig. 4.2a is a spiral wedge case as is Fig. 4.2b; however, the latter's intersection curves start to look closer to bubbles. Fig. 4.2c is clearly a bubbles case while Fig. 4.2d is once again a spiral wedge. Fig. 4.2e is a wedge with no spirals. Fig. 4.2f and Fig. 4.2g are both spiral wedges though the latter again has bubble-like pole-to-pole curves. Fig. 4.2h is also a spiral case but the manifolds seem to be pulling apart and begins to form structure similar to the non-intersecting case. Fig. 4.2i and Fig. 4.2j are both non-

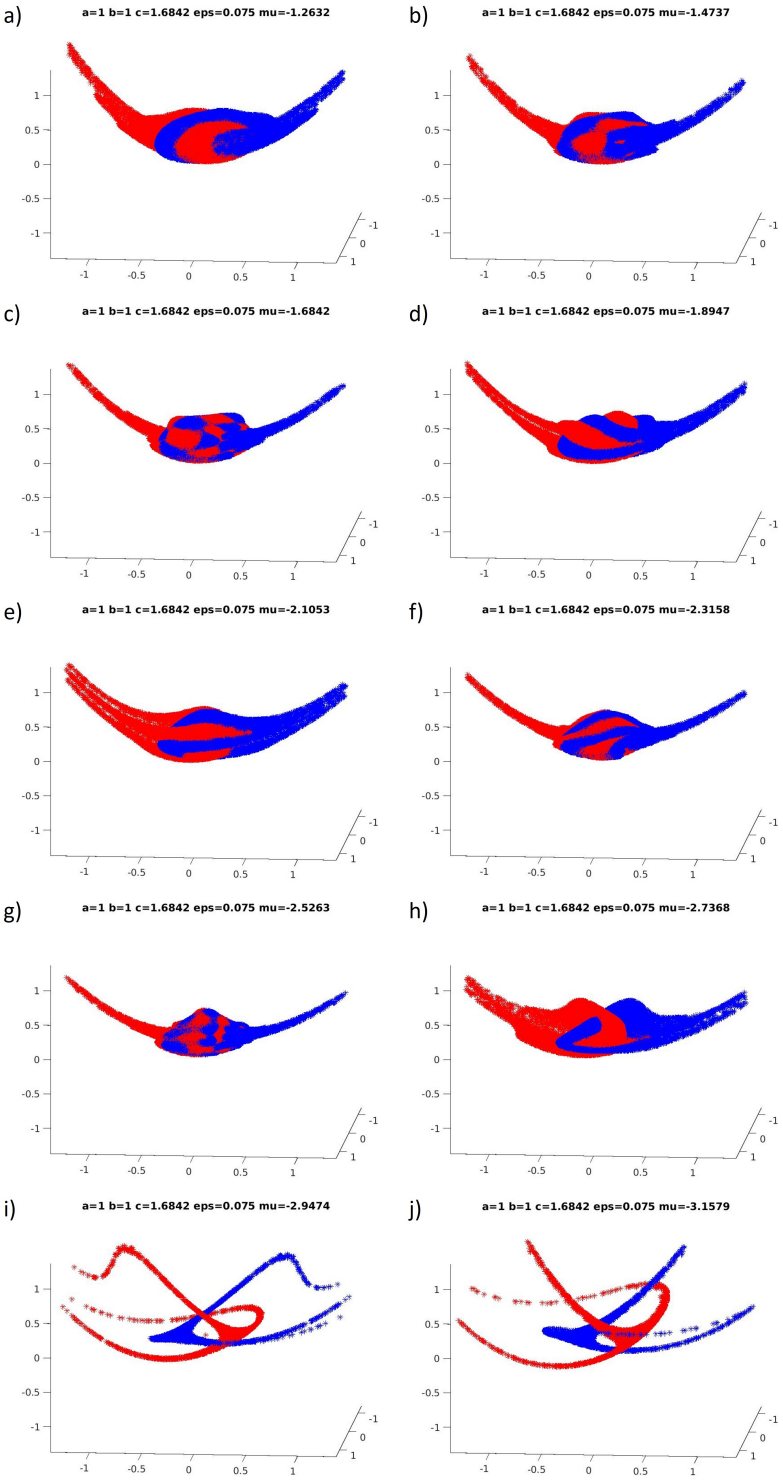

Figure 4.2: Stable and unstable manifolds for decreasing values of μ. a) and b) are both spiral wedges. c) is a bubbles case while d) is again a sprial wedge. e) is a wedge with no spiral. f) - h) are spiral wedges. i) and j) are both non-intersecting.

intersecting. We expected that wedges and spiral wedges would be similar enough that they could easily transform from one case to the other. However, we were surprised by how the bubbles case shifted into a spiral wedge case. We speculate that what appear to be bubbles might be full spirals sufficiently close to the fixed point. This warrants further study. Finally as μ decreases we see the manifolds pull away from each other and form into the non-intersecting case. We're not sure what the dynamics behind this final case is but it is also worth further investigation.

Our broad search of parameter space gave us a clearer idea of how the stable and unstable manifolds might intersect in 3D when an equatorial intersection could not be found. We still hoped to find an equatorial intersection and so had to narrow our search of parameter space.

4.2.2 Narrowing the Search of Parameter Space

To narrow our search of parameter space, we drew inspiration from work by Dullin and Meiss [22]. This work focused mainly on the invariant circles that form inside the *vortex bubble* of the system. They define the vortex bubble as a roughly spherical volume of space enclosing the fixed points and the majority of intersections between the 2D manifolds. We wanted to find a parameter space with an equatorial intersection but not the invariant circles and invariant tori that Dullin and Meiss were studying; essentially, we believed that if we found a parameter set near their work, we could then move to a region of parameter space where the invariant tori no longer formed.

Dullin and Meiss constructed a figure similar to fig. 4.3 to help identify regions with invariant circles. To construct this figure, we considered 100^3 points on a three-dimensional box with dimensions $[-2x_+, 2x_+] \times [-4x_+, 4x_+] \times [-8x_+, 8x_+]$ for 100^2 parameters of $0 \leq \epsilon \leq 0.4$ and $-4 \leq \mu \leq 0$. An initial point was considered "bounded" if it remained within a ball of $r = 10$ for 10^4 iterates. The resultant percent of bounded orbits were plotted for each (ϵ, μ) point.

Using fig. 4.3 as a guide, we chose to set $\epsilon = 0.075$ and explore varying values for $\bar{c}$ and μ. We chose a low enough epsilon to allow us to be close to the near integrable case of the map while still allowing us to identify an equatorial intersection. We

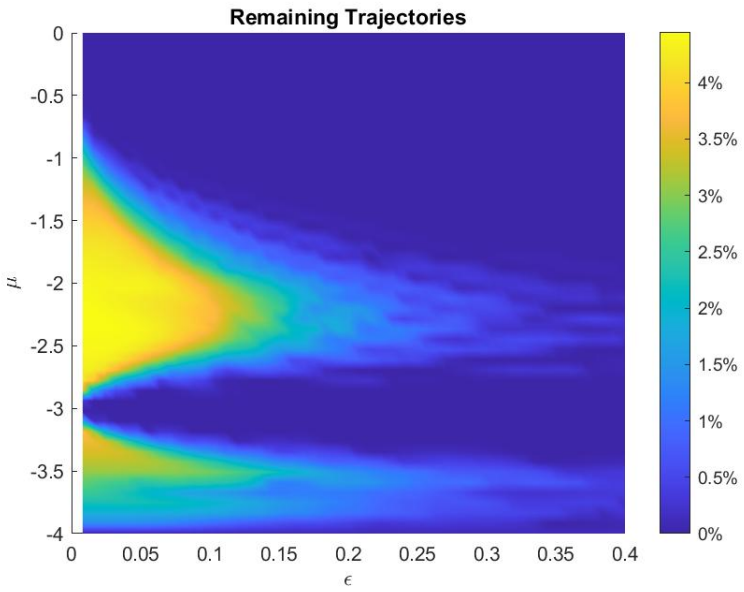

Figure 4.3: Remaining trajectories of 100^3 points inside a ball of radius 10 after 10^4 iterates. For this plot we used quadratic parameters $\bar{a} = 1$, $\bar{b} = 1$, $\bar{c} = 0.5$.

generated 2D stable and unstable manifolds for a 20×20 grid of $0 \leq \bar{c} \leq 2$ and $-4 \leq \mu \leq 0$. We sorted the manifolds for each parameter set into one of the six categories discussed in sec. 4.2.1. Unfortunately, our refined search of phase space was unable to identify parameters with equatorial intersection curves necessary to perform HLD in its current form. After consulting with colleagues who had also worked on the quadratic family of maps we concluded that cases with well-defined resonance zones either did not exist or were extremely rare within the quadratic family of maps.

4.3 The 3D Modified Hénon Map

Our next attempt to apply HLD to an analytic 3D map involved creating a new map using the 2D Hénon map. This has the advantage of allowing us to force a well-defined resonance zone and reversibility. We began by taking the Hénon map and extending it into three dimensions,

$$H(x, y, z) = \begin{pmatrix} y - k + x^2 \\ -x \\ z \end{pmatrix} \tag{4.16}$$

This is the 2D Hénon map stretched along the z-axis. To introduce variation in the map along the z-direction we made k a function of z,

$$k(z) = \delta \sin(2\pi z) + k_{ave}. \tag{4.17}$$

k is sinusoidally dependent on z. We used a period of $2\pi z$ to allow for the identification of $z = 0$ with $z = 1$. Each point on the z-axis is a fixed point with 1D stable and unstable manifolds originating from it. Since $z = 0$ and $z = 1$ are identified the 2D resonance zone becomes a 3D resonance zone. The z-axis can be imagined to be a loop closed on itself, and the resonance zone a torus attached to the z-axis. We have introduced two new parameters, δ which controls how much k changes with z and k_{ave} as the average k value.

We turned the z-axis from a stack of fixed points to an invariant circle by creating a second mapping,

$$M_z = \begin{pmatrix} x \\ y \\ (z + \phi) \mod 1 \end{pmatrix} \tag{4.18}$$

and introducing a third parameter, ϕ, which governs the shift in the z-direction. Putting eq. 4.16 and eq. 4.18 together we get the map M,

$$M = M_z \circ H \tag{4.19}$$

This map produces some mixing and asymmetries in the ETP in fig. 4.4. To introduce more mixing we added a sheer in the x-direction to M_z transforming eq. 4.18 into

$$M_z = \begin{pmatrix} x \\ y \\ (z + \phi + ax) \mod 1 \end{pmatrix}. \tag{4.20}$$

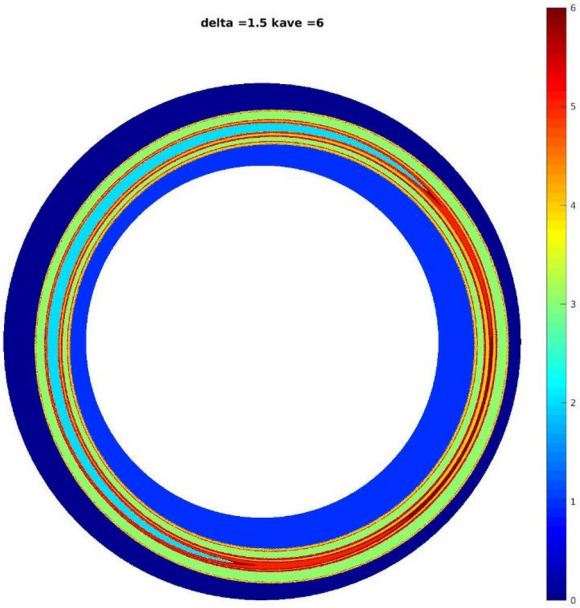

Figure 4.4: Forward ETP using the modified Hénon map in eq. 4.19 with the shift in eq. 4.18. Some boundaries are non-equatorial, however the dynamics present are not sufficiently complex.

This adds a fourth parameter a which controls the strength of the sheer in the x-direction. This new sheer produces a nice amount of 3D mixing as in fig. 4.5. In this example we've used parameters $\delta = 2$, $k_{ave} = 4.5$ and $a = .35$.

To determine if a map is fully 3D, we examined the forward and backward ETP. This allowed us to identify curves that are equatorial in one direction but non-equatorial in the other. The toy model example in fig. 4.6 shows how this would appear. In fig. 4.6a the curve $\boldsymbol{a}_{-n}$ in the forward-ETP iterates backward to $\boldsymbol{a}_0$ in the backward-ETP. In this case $\boldsymbol{a}_{-n}$ is equatorial while $\boldsymbol{a}_0$ is not. The same is true for $\boldsymbol{b}_{-n}$ and $\boldsymbol{b}_0$. This indicates that the manifolds that make up the ETPs of fig. 4.6a are not reducible to 2D equivalents. In fig. 4.6b $\boldsymbol{a}_{-n}$ in the forward-ETP and $\boldsymbol{a}_0$ in the backward ETP are both non-equatorial. The is also true $\boldsymbol{b}_{-n}$ and $\boldsymbol{b}_0$. The manifolds that result in the ETPs in fig. 4.6b could possibly be reduced to a 2D equivalent.

Fig. 4.7a is a cartoon that is topologically equivalent to the fifth iterate information in fig. 4.5. Fig. 4.7b is a cartoon version of the fifth iterate backward-ETP

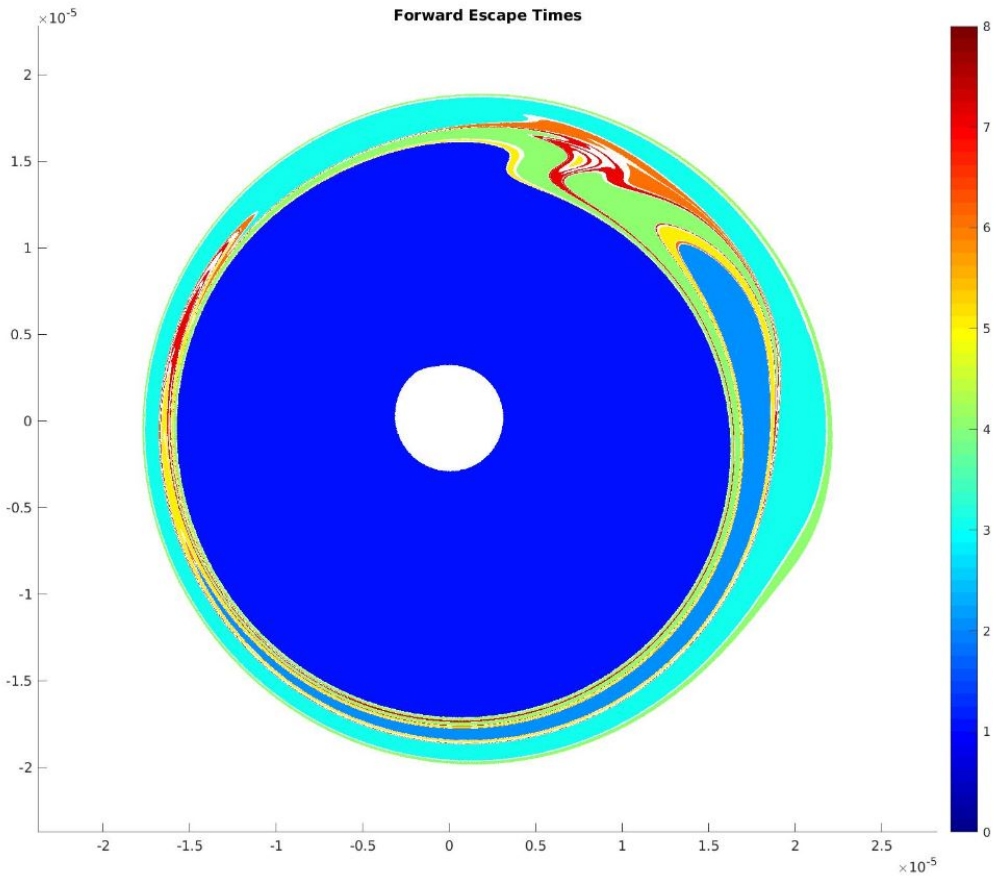

Figure 4.5: Forward-ETP for the modified Hénon map with parameters $\delta = 2$, $k_{ave} = 4.5$ and $a = .35$. Seven iterates are computed in the forward direction.

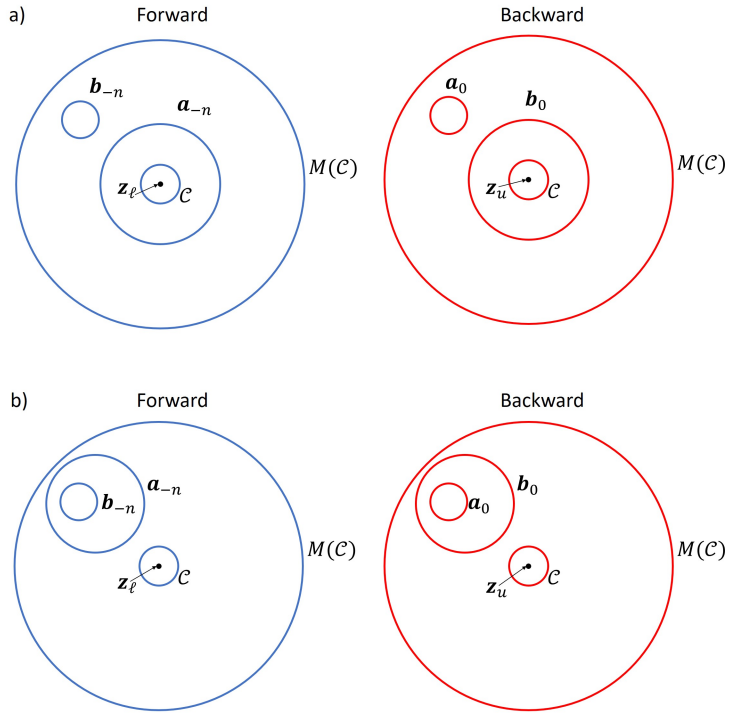

Figure 4.6: Intersection curves that are equatorial or non-equatorial in the respective ETP. In a) the curve $\boldsymbol{a}_{-n}$ is equatorial in the forward ETP but $\boldsymbol{a}_0$ is non-equatorial in the backward ETP. In b) both $\boldsymbol{a}$ and $\boldsymbol{b}$ are non-equatorial in both forward and backward ETP.

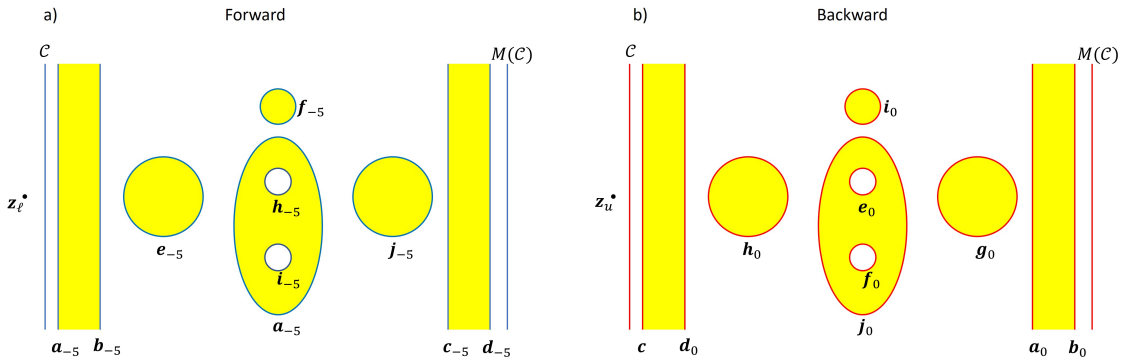

Figure 4.7: Cartoon versions of the forward and backward ETPs for the modified Hénon map with parameters $\delta = 2$, $k_{ave} = 4.5$ and $a = .35$. The ETPs are cut and "unfolded" such that the curve $\mathcal{C}$ becomes a line. We display only the fifth iterate data of these ETPs.

of the same set of manifolds. Note that the ETP has been cut and "unfolded" around the curve $\mathcal{C}$.

The curves $\boldsymbol{a}$, $\boldsymbol{b}$, $\boldsymbol{c}$, and $\boldsymbol{d}$ are all equatorial in both forward and backward ETP while $\boldsymbol{e}$, $\boldsymbol{f}$, $\boldsymbol{g}$, $\boldsymbol{h}$, $\boldsymbol{i}$, and $\boldsymbol{j}$ are non-equatorial in both ETPs. This result does not conclusively show that these parameter values result in fully 3D mixing. Repeating the analysis for other iterates produced the same inconclusive result which indicated that it was like that the map was always reducible to 2D.

At this point, we had explored in depth two different maps in the hopes of finding a system that included equatorial intersection curves leading to a well defined resonance zone, and a system with fully 3D dynamics. The quadratic family of maps does not seem to generically produce equatorial intersection curves and could not be analyzed using HLD. Our attempt at modifying the Hénon map to produce the needed dynamics in 3D failed as well. While we did get equatorial intersection curves and a well defined resonance zone which would allow us to apply HLD, the system itself was not fully 3D. We decided our next step would be to extend the HLD technique to systems without a well defined resonance zone.

Chapter 5

Poorly Defined Resonance Zones and Invariant Circles

To apply HLD to systems where there were no equatorial intersection curves we needed to change our perspective of the systems we were considering. Previously we considered only the 2D stable and unstable manifolds of the two fixed points. We concluded that we needed to also consider the 1D manifolds of these fixed points. Even more importantly we realized that in cases where the 2D manifolds of the fixed points formed wedges the pole-to-pole curves that formed could be considered invariant (or periodic) circles. These invariant circles would have associated 2D manifolds extending from them. By considering the 2D manifolds of the invariant circles we could obtain intersections that were not equatorial to the fixed points, but equatorial to the invariant circles. This in turn would allow us to identify a well-defined resonance zone and apply HLD. As seen previously the topology of the 2D stable and unstable manifolds can become very intricate in numerical models. Thus we have opted to explain our extension of 3D HLD using a series of "toy model" examples. These examples were chosen to illustrate the basic concept of 3D HLD and how a shift in perspective allows us to extend it to systems we could not previously work with. A motivated reader will be able to apply the same techniques to a wide class of trellises.

Section 5.1.1 introduces a number of key definitions concerning the invariant manifolds attached to fixed points and their intersections. Section 5.1.2 discusses

how a pole-to-pole intersection curve allows us to recast our definitions for invariant manifolds of an invariant circle. Sections 5.2-5.6 are a series of examples that demonstrate how we extend the 3D HLD technique. Section 5.2 discusses a 3D system where the invariant manifolds of the fixed points have an equatorial intersection curve. Section 5.3 presents a simple case where an equatorial intersection curve does not exist. We show that we can extract rules for topological forcing in this example, but we cannot analyze the full trellis. Section 5.4 analyzes a basic trellis composed of invariant manifolds attached to the invariant circle constructed from pole-to-pole intersection curves. We are able to successfully apply HLD to this system. Section 5.5 considers the trellis analyzed in Sec. 5.3 and, extending it slightly, reanalyzes it as invariant manifolds of the invariant circle. With the slight modification, we successfully apply HLD to the full trellis and show that the graphical equations in Sec. 5.5 reduce to the graphical equations in Sec. 5.3. Section 5.6 is the culmination of our work. An equatorial intersection does not exist between the 2D manifolds of the fixed points, and we require two homoclinic curves to construct a resonance zone using the invariant manifolds of the invariant circle. The bridge dynamics are explicitly 3D in nature and include both 2D and 1D components.

5.1 Preliminaries

5.1.1 Invariant manifolds attached to fixed points

Suppose that we have a volume-preserving map M in $\mathbb{R}^3$ and that M has two hyperbolic fixed points, which we assume lie on the z-axis. We assume the upper fixed point, denoted $\mathbf{z}_u$, has two stable directions and one unstable direction. See Fig. 5.1a. The two stable directions point along the horizontal plane and the unstable direction points vertically. Similarly, we assume the lower fixed point, denoted $\mathbf{z}_\ell$, has two unstable directions, aligned horizontally, and one stable direction, aligned vertically. The 2D stable manifold of $\mathbf{z}_u$ is denoted $W^S_{\mathbf{z}_u}$, and the 2D unstable manifold of $\mathbf{z}_\ell$ is denoted $W^U_{\mathbf{z}_\ell}$. Two-dimensional connected submanifolds of $W^S_{\mathbf{z}_u}$ can be specified by the set of n curves $\boldsymbol{\gamma}_1, ..., \boldsymbol{\gamma}_n$ that form the boundary

of the submanifold (Fig. 5.1b). We designate the (closed) submanifold by the notation $W^S_{\mathbf{z}_u}[\boldsymbol{\gamma}_1, ..., \boldsymbol{\gamma}_n]$. Similar notation applies to submanifolds of $W^U_{\mathbf{z}_\ell}$. The 1D unstable manifold of $\mathbf{z}_u$ and stable manifold of $\mathbf{z}_\ell$ are denoted $W^U_{\mathbf{z}_u}$ and $W^S_{\mathbf{z}_\ell}$, respectively. (Closed) subintervals of these manifolds, with endpoints $\mathbf{a}$ and $\mathbf{b}$, are denoted by $W^U_{\mathbf{z}_u}[\mathbf{a}, \mathbf{b}]$ and similarly for $W^S_{\mathbf{z}_\ell}$.

We focus first on the 2D invariant manifolds $W^S_{\mathbf{z}_u}$ and $W^U_{\mathbf{z}_\ell}$. Following Lomeli and Meiss [40], we define fundamental annuli and primary intersections of stable and unstable manifolds. We first define an *equatorial* curve of either invariant manifold as a non-self-intersecting curve that winds once around the fixed point, i.e. an equatorial curve bounds a topological disk (within the invariant manifold) that includes the fixed point in its interior (see Fig. 5.1c). Next, we define a *proper loop* $\boldsymbol{\gamma}$ as an equatorial curve that does not intersect its own iterate, i.e. $M(\boldsymbol{\gamma}) \cap \boldsymbol{\gamma} = \varnothing$. A *fundamental domain*, or *fundamental annulus*, is then the region of an invariant manifold between a given proper loop and its iterate. See Fig. 5.1d. One edge of a fundamental annulus is open and the other closed, which we denote by $W^S_{\mathbf{z}_u}(\boldsymbol{\gamma}, M(\boldsymbol{\gamma})]$ if $\boldsymbol{\gamma}$ is omitted and $W^S_{\mathbf{z}_u}[\boldsymbol{\gamma}, M(\boldsymbol{\gamma}))$ if $M(\boldsymbol{\gamma})$ is omitted, and similarly for $W^U_{\mathbf{z}_\ell}$. Note that each trajectory within the invariant manifold passes through a given fundamental annulus exactly once. The collection of all fundamental annuli in $W^U_{\mathbf{z}_\ell}$ is denoted $\mathcal{F}^U_{\mathbf{z}_\ell}$ and all fundamental annuli in $W^S_{\mathbf{z}_u}$ is denoted $\mathcal{F}^S_{\mathbf{z}_u}$. Fundamental annuli are important because they can be used to generate the entire invariant manifold, and indeed this is often how invariant manifolds are computed in practice. Heteroclinic intersections between the stable and unstable manifolds are often detected by fixing the stable fundamental annulus and then iterating the unstable annulus forward. Each heteroclinic trajectory will then land exactly once within the fundamental stable annulus.

Lomeli and Meiss [40] define the *intersection index* κ between two fundamental annuli $\mathcal{U} \in \mathcal{F}^U_{\mathbf{z}_\ell}$ and $\mathcal{S} \in \mathcal{F}^S_{\mathbf{z}_u}$ as the largest iterate of $\mathcal{S}$ that still intersects $\mathcal{U}$, i.e.

$$\kappa(\mathcal{U}, \mathcal{S}) = \max\left\{k \in \mathbb{Z} | M^k(\mathcal{S}) \cap \mathcal{U} \neq \varnothing\right\}. \tag{5.1}$$

We define an *index-0 point* as a point that lies in the intersection between two fundamental annuli of intersection index 0, i.e. $\mathbf{r}$ is an index-0 point if $\mathbf{r} \in \mathcal{S} \cap \mathcal{U}$ for some $\mathcal{U} \in \mathcal{F}^U_{\mathbf{z}_\ell}$ and $\mathcal{S} \in \mathcal{F}^S_{\mathbf{z}_u}$ satisfying $\kappa(\mathcal{U}, \mathcal{S}) = 0$. Similarly, an *index-0 curve*

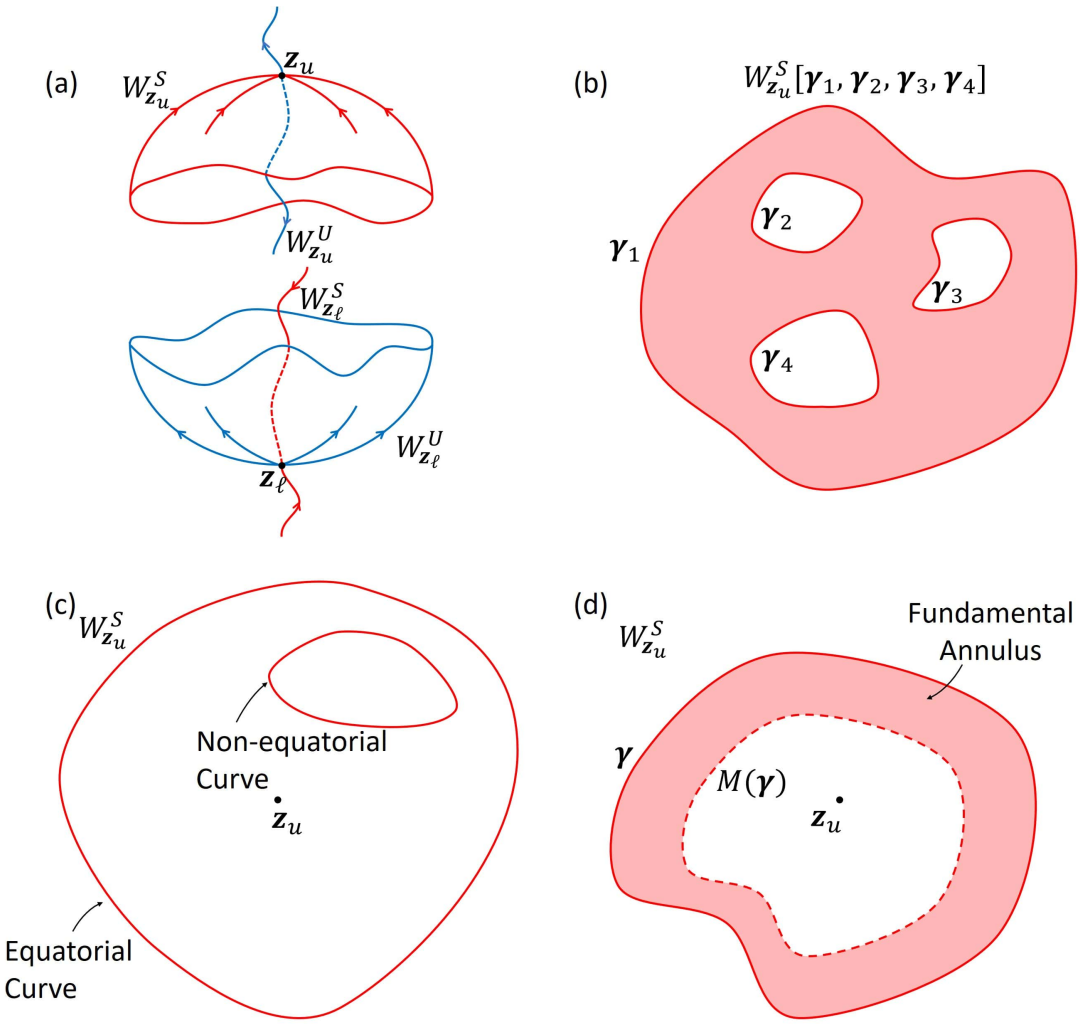

Figure 5.1: (a) Two fixed points with their resultant invariant manifolds. The lower fixed point $\boldsymbol{z}_\ell$ has a 2D unstable manifold $W^U_{\boldsymbol{z}_\ell}$ and a 1D stable manifold $W^S_{\boldsymbol{z}_\ell}$. The upper fixed point $\boldsymbol{z}_u$ has a 2D stable manifold $W^S_{\boldsymbol{z}_u}$ and 1D unstable manifold $W^U_{\boldsymbol{z}_u}$. (b) A submanifold of a 2D stable manifold. It is uniquely defined by the boundary curves $\boldsymbol{\gamma}_1$, $\boldsymbol{\gamma}_2$, $\boldsymbol{\gamma}_3$, and $\boldsymbol{\gamma}_4$. (c) Two curves on the stable manifold. An equatorial curve encloses the fixed point. A non-equatorial curve does not. (d) A fundamental annulus defined by the curve $\boldsymbol{\gamma}$ (included in the annulus) and its iterate $M(\boldsymbol{\gamma})$ (not included in the annulus).

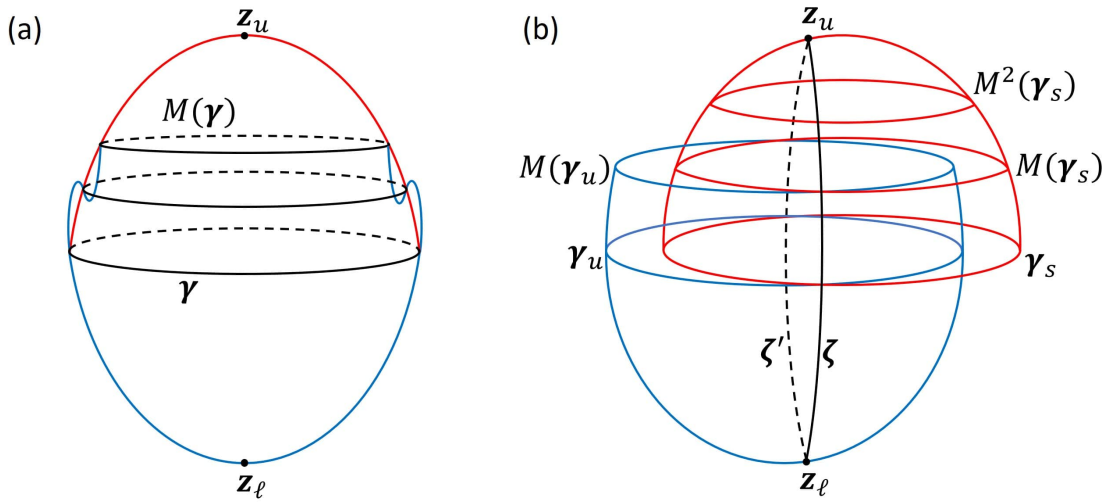

Figure 5.2: (a) 2D stable (red) and unstable (blue) manifolds with a primary (equatorial) intersection curve γ. (b) 2D stable and unstable manifolds without an equatorial intersection curve. γ_s and γ_u are equatorial but are not intersection curves. Two pole-to-pole intersection curves ζ and ζ' exist connecting z_u and z_ℓ.

is one that consists entirely of index-0 points.

We define a *primary intersection curve* γ as an equatorial curve on both the stable and unstable manifolds such that the stable disk $W^S_{z_u}[\gamma]$ and the unstable disk $W^U_{z_\ell}[\gamma]$ only intersect at their common boundary γ. See Fig. 5.2a. It is clear that a primary intersection curve has index 0. Our definition of primary intersection curve reduces to the definition of a primary intersection point for 2D maps [23] [1]. For such an intersection γ, choose stable and unstable fundamental domains $\mathcal{S} = W^S[\gamma, M(\gamma))$ and $\mathcal{U} = W^U[M^{-1}(\gamma), \gamma)$. The set of all index-0 points is readily seen to be $M(\mathcal{U}) \cap \mathcal{S}$, plus all forward and backward iterates. In other words, we do not need to search over all possible pairs of fundamental annuli with index 0. We need only consider the pair $(M(\mathcal{U}), \mathcal{S})$, which has index 0. In Fig. 5.2a, there are, up to iteration, two primary intersection curves γ and β. Despite their convenience, primary intersection curves need not exist, and many important examples do not have them. For example, we have been unable

[1] Our definition of a primary intersection curve differs from Lomeli and Meiss [40]. Their primary intersection curve is what we call an index-0 curve.

to find primary intersection curves in the family of volume-preserving quadratic maps [39, 22, 35, 45]. Other kinds of index-0 curves may form loops that do not encircle the fixed point or curves that stretch from pole to pole, that is curves that converge upon $\mathbf{z}_u$ in one direction and upon $\mathbf{z}_\ell$ in the other. Figure 5.2b illustrates a pole-to-pole intersection curve of index 0. Both non-equatorial index-0 loops and pole-to-pole index-0 curves exist in the family of 3D volume-preserving quadratic maps [45].

We further refine our analysis of heteroclinic intersections by defining the *index* σ of a heteroclinic intersection $\mathbf{r}$. This index is the smallest intersection index of any two fundamental annuli that intersect at $\mathbf{r}$, i.e.

$$\sigma(\mathbf{r}) = \min\left\{\kappa(\mathcal{U},\mathcal{S})|\ \mathbf{r} \in \mathcal{S}\cap\mathcal{U} \text{ for } \mathcal{U}\in\mathcal{F}^U_{\mathbf{z}_\ell}, \mathcal{S}\in\mathcal{F}^S_{\mathbf{z}_u}\right\}.$$

An equivalent characterization of heteroclinic intersection points is via the transition number. For any two fundamental annuli $\mathcal{U}\in\mathcal{F}^U_{\mathbf{z}_\ell}$ and $\mathcal{S}\in\mathcal{F}^S_{\mathbf{z}_u}$, the *transition number* $\tau_{\mathcal{US}}$ of a heteroclinic trajectory $\mathbf{r}_i$ *relative* to $(\mathcal{U},\mathcal{S})$ is defined as the number of iterates needed for the trajectory to map from $\mathcal{U}$ to $\mathcal{S}$, i.e.

$$\tau_{\mathcal{US}}(\mathbf{r}_i) = n, \text{ where } M^n(\mathbf{r}_j)\in\mathcal{S} \text{ when } \mathbf{r}_j\in\mathcal{U} \text{ for some } j.$$

Typically one chooses the unstable fundamental annulus to "precede" the stable fundamental annulus so that the transition numbers are positive. This is formalized by the concept of a properly ordered pair of fundamental annuli: $\mathcal{U}\in\mathcal{F}^U_{\mathbf{z}_\ell}$ and $\mathcal{S}\in\mathcal{F}^S_{\mathbf{z}_u}$ are said to be *properly ordered* if $\mathcal{U}\cap M^n(\mathcal{S}) = \varnothing$ for all $n\geq 0$. We then define *the* transition number τ of a trajectory $\mathbf{r}_i$, independent of the choice of fundamental annuli, as

$$\tau(\mathbf{r}_i) = \min\left\{\tau_{\mathcal{US}}(\mathbf{r}_i)|\ \mathcal{S}\in\mathcal{F}^S_{\mathbf{z}_u}, \mathcal{U}\in\mathcal{F}^U_{\mathbf{z}_\ell} \text{ are properly ordered}\right\}.$$

Note that τ is constant on a single connected intersection curve, whereas $\tau_{\mathcal{US}}$ need not be. It follows immediately from the above definitions that the transition number of a heteroclinic intersection equals its index plus one, i.e. $\tau = \sigma + 1$.

Primary intersection curves are again particularly useful for analyzing transition numbers. Assuming that such a curve $\boldsymbol{\gamma}$ exists, choose $\mathcal{S} = W^S[\boldsymbol{\gamma}, M(\boldsymbol{\gamma}))$

and $\mathcal{U} = W^U[M^{-1}(\boldsymbol{\gamma}), \boldsymbol{\gamma})$ as above. Then $\tau(\mathbf{r}) = \tau_{\mathcal{US}}(\mathbf{r})$ for all heteroclinic intersections $\mathbf{r}$ simultaneously. There is no need to consider other fundamental annuli. If no primary intersection exists, however, there may be no choice of $\mathcal{U}$ and $\mathcal{S}$ that simultaneously minimizes the relative transition number for all heteroclinic intersections. This is true even when considering a single heteroclinic intersection curve; as noted previously, there may be no choice of $\mathcal{U}$ and $\mathcal{S}$ such that $\tau_{\mathcal{US}}$ is constant on the curve.

For a primary intersection curve $\boldsymbol{\gamma}$, consider the two caps $W^S_{\mathbf{z}_u}[\boldsymbol{\gamma}]$ and $W^U_{\mathbf{z}_\ell}[\boldsymbol{\gamma}]$, as shown in Fig. 5.2a. These caps bound a compact domain R, which we call the *resonance zone*. Specifying $\mathcal{S} = W^S[\boldsymbol{\gamma}, M(\boldsymbol{\gamma}))$ and $\mathcal{U} = W^U[M^{-1}(\boldsymbol{\gamma}), \boldsymbol{\gamma})$ as above, define the *escape time* for every point in $\mathcal{U}$ as the number of iterates for it to map out of R. (For simplicity, assume that no trajectory reenters R after it has escaped.) Then the set of points with a given escape time n is divided into disconnected open *escape domains*. The boundary of these open domains are heteroclinic curves with transition number n. *Escape-time plots* (ETPs), i.e. 2D plots of the escape time, are an effective way to visualize the structure of heteroclinic intersection curves when primary intersections exist. See Fig. 5.6 in Sec. 5.2. In this paper, we use both *forward* and *backward* escape-time plots defined respectively on the unstable and stable fundamental annuli using the forward and backward maps.

We now shift our focus to the 1D stable and unstable manifolds of $\mathbf{z}_\ell$ and $\mathbf{z}_u$, respectively, and their relationship to the 2D manifolds. Many of the above definitions for the 2D manifolds have similar formulations for the 1D manifolds. A *fundamental domain* of either 1D manifold is simply a half-open interval between a point $\mathbf{r}$ and its iterate $M(\mathbf{r})$. The collections of all such fundamental domains of the 1D manifolds are denoted $\mathcal{F}^U_{\mathbf{z}_u}$ and $\mathcal{F}^S_{\mathbf{z}_\ell}$. We then define the intersection index $\tau_{\mathcal{US}}$ between a 1D (stable/unstable) fundamental domain and a 2D (unstable/stable) fundamental domain using Eq. (5.1) as before. The definition of an index-0 point between a 1D (stable/unstable) invariant manifold and 2D (unstable/stable) invariant manifold similarly generalizes: an index-0 point is a point that lies in the intersection of two fundamental domains of intersection index 0. More generally, the index σ of a heteroclinic intersection between 1D invariant and 2D invariant

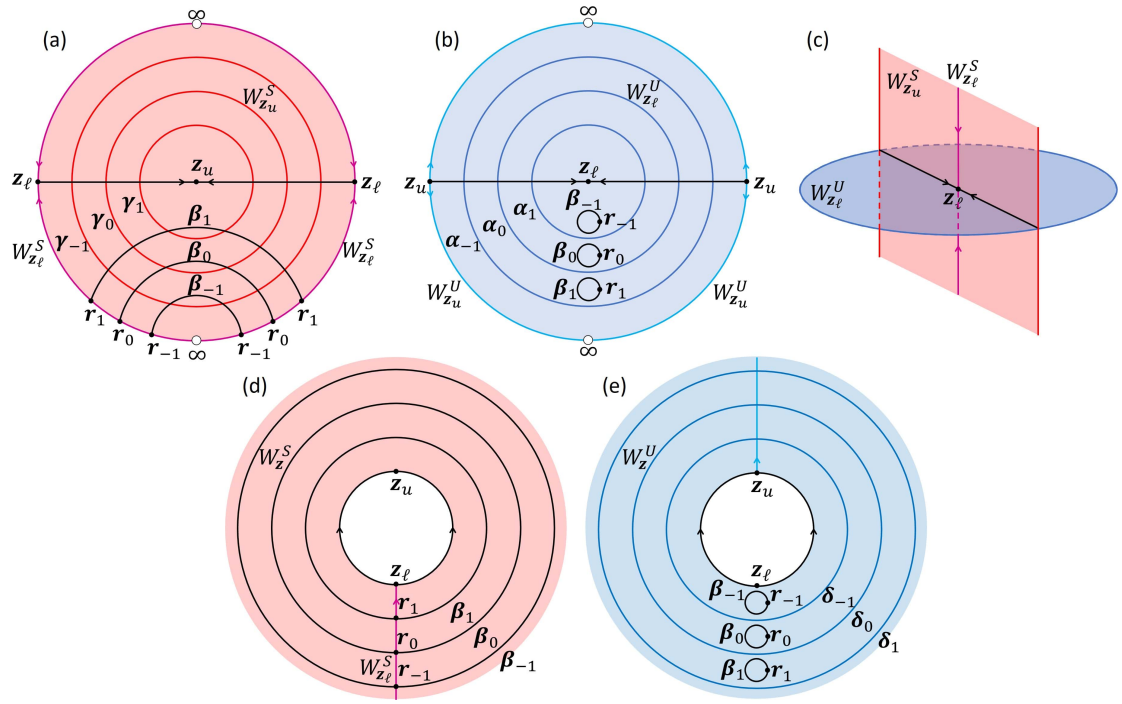

Figure 5.3: (a) The union of the 2D stable manifold $W^S_{\boldsymbol{z}_u}$ (red disk) and the 1D stable manifold $W^S_{\boldsymbol{z}_\ell}$ (magenta). Two pole-to-pole intersection curves connect the fixed points $\boldsymbol{z}_u$ and $\boldsymbol{z}_\ell$. The red curves $\boldsymbol{\gamma}_n$ form a family of proper loops. The 1D intersection curves $\boldsymbol{\beta}_n$ (black) asymptotically approach the points $\boldsymbol{r}_n$ on the 1D stable manifold. (b) The union of the 2D unstable manifold $W^U_{\boldsymbol{z}_\ell}$ (blue) and the 1D unstable manifold $W^U_{\boldsymbol{z}_u}$ (cyan). The intersection curves $\boldsymbol{\beta}_n$ from (a) together with the points $\boldsymbol{r}_n$ are closed circles. (c) A 3D view of the invariant manifolds in the vicinity of the fixed point $\boldsymbol{z}_\ell$. (d) One-half of the 2D stable manifold of the invariant circle formed by the pole-to-pole intersection curves from $\boldsymbol{z}_\ell$ to $\boldsymbol{z}_u$. The union of $\boldsymbol{\beta}_n$ and $\boldsymbol{r}_n$ forms a proper loop of the invariant circle. (e) One-half of the 2D unstable manifold of the invariant circle. The union of $\boldsymbol{\beta}_n$ and $\boldsymbol{r}_n$ is not an equatorial curve on the unstable manifold of the invariant circle $\boldsymbol{z}$.

manifolds is defined analogous to Eq. (5.2). Similarly the definition of the transition number $\tau_{\mathcal{US}}$ of a heteroclinic point $\mathbf{r}$ relative to fundamental domains $\mathcal{U}$ and $\mathcal{S}$ carries over analogously, as does the concept of properly ordered fundamental domains and the definition of the transition number τ of a heteroclinic point.

5.1.2 Invariant manifolds attached to an invariant circle

Suppose now that a pole-to-pole index-0 curve exists between $W^U_{\mathbf{z}_\ell}$ and $W^S_{\mathbf{z}_u}$, as in Fig. 5.2b. For simplicity, we assume that there are only two such pole-to-pole curves and that these curves are invariant, i.e. each curve maps to itself. In general, there can be any even number of pole-to-pole intersection curves, and they may each be invariant or form periodic families of curves. All of our results can easily be extended to this more general case.

Now, let $\mathbf{r}_0$ be a heteroclinic intersection point between the 1D manifold $W^S_{\mathbf{z}_\ell}$ and the 2D manifold $W^U_{\mathbf{z}_\ell}$. Given the presence of the two pole-to-pole curves, we assert that there must be a 1D intersection $\boldsymbol{\beta}_0$ between the 2D manifolds $W^S_{\mathbf{z}_u}$ and $W^U_{\mathbf{z}_\ell}$. The set $\boldsymbol{\beta}_0$ has the topology of a curve with a single point removed at $\mathbf{r}_0$; that is, the union of $\boldsymbol{\beta}_0$ and $\mathbf{r}_0$ is a continuous curve. Furthermore, the index of the set $\boldsymbol{\beta}_0$ equals the index of the point $\mathbf{r}_0$. These facts will be proved below.

Fig. 5.3a shows a convenient way of visualizing heteroclinic intersections when two pole-to-pole intersections exist. The open disk in Fig. 5.3a represents the entirety of $W^S_{\mathbf{z}_u}$. The fixed point $\mathbf{z}_u$ is at the center of the disk. A proper loop $\boldsymbol{\gamma}_0$ encircles the fixed point. Its forward iterate $\boldsymbol{\gamma}_1$ is closer to $\mathbf{z}_u$ and its backward iterate $\boldsymbol{\gamma}_{-1}$ is farther away. The regions between iterates of the proper loop are fundamental stable domains. In this representation, as $\boldsymbol{\gamma}_0$ is mapped backward an arbitrary number of times it approaches, but never reaches, the outer boundary of the disk. At the left and rightmost boundary points of the disk is the lower fixed point $\mathbf{z}_\ell$. Though represented twice in the figure, these two points are geometrically the same and are thus identified with one another. The black horizontal line represents both pole-to-pole intersection curves connecting $\mathbf{z}_u$ to $\mathbf{z}_\ell$. The lower half of $W^S_{\mathbf{z}_u}$ in Fig. 5.3a corresponds to the left piece of $W^S_{\mathbf{z}_u}$ in Fig. 5.2b, which is in the "interior" region, whereas the upper half of $W^S_{\mathbf{z}_u}$ in Fig. 5.3a corresponds to

the right piece of $W^S_{\mathbf{z}_u}$ in Fig. 5.2b, which remains in the "exterior" region.

The 1D stable manifold of $\mathbf{z}_\ell$ is shown as the magenta boundary of the disk in fig 5.3a. It is divided into four separate curves, each beginning at $\mathbf{z}_\ell$ and terminating at the open circle at either the bottom or the top. Just as the left copy of $\mathbf{z}_\ell$ is identified with the right copy of $\mathbf{z}_\ell$, the lower left branch of $W^S_{\mathbf{z}_\ell}$ is identified with the lower right branch of $W^S_{\mathbf{z}_\ell}$. Similarly, the upper left branch of of $W^S_{\mathbf{z}_\ell}$ is identified with the upper right branch. These identifications mean that there is a single upper branch of $W^S_{\mathbf{z}_\ell}$, corresponding to the bottom half of $W^S_{\mathbf{z}_\ell}$ in Fig. 5.1a, and a single lower branch, corresponding of the top half in Fig. 5.1a. Because the stable manifold $W^S_{\mathbf{z}_u}$ of the upper fixed point approaches the lower fixed point (via backward iteration) along the pole-to-pole intersection curve, the stable manifold $W^S_{\mathbf{z}_u}$ is eventually drawn away from $\mathbf{z}_\ell$ (via backward iteration) along the 1D curve $W^S_{\mathbf{z}_\ell}$, so that the 2D manifold $W^S_{\mathbf{z}_u}$ converges upon the 1D manifold $W^S_{\mathbf{z}_\ell}$. This geometry is shown in Fig. 5.3c. For this reason, we have placed the red curve $W^S_{\mathbf{z}_\ell}$ along the boundary of the disk representing $W^S_{\mathbf{z}_u}$ in Fig. 5.3a. Finally, the open circles at the top and bottom of the disk are not points within $W^S_{\mathbf{z}_\ell}$, but can be thought of as points "at infinity" along the 1D stable manifold.

Recall that $W^S_{\mathbf{z}_\ell}$ transversely intersects the 2D unstable manifold $W^U_{\mathbf{z}_\ell}$ at the point $\mathbf{r}_0$. Then because $W^S_{\mathbf{z}_u}$ converges upon $W^S_{\mathbf{z}_\ell}$, $W^S_{\mathbf{z}_u}$ must also intersect $W^U_{\mathbf{z}_\ell}$ in the curve $\boldsymbol{\beta}_0$. We have drawn $\boldsymbol{\beta}_0$ as a single arc in Fig. 5.3a, though in fact $\boldsymbol{\beta}_0$ could intersect $W^S_{\mathbf{z}_\ell}$ multiple times. Notice that $\boldsymbol{\beta}_0$ does not fit within a single fundamental domain, as defined by the curves $\boldsymbol{\gamma}_n$. Indeed, there is no proper loop for which the resulting fundamental domain would include the entire curve $\boldsymbol{\beta}_0$, since $\boldsymbol{\beta}_0$ terminates at $W^S_{\mathbf{z}_\ell}$.

Fig. 5.3b is a representation of $W^U_{\mathbf{z}_\ell}$ analogous to Fig. 5.3a for $W^S_{\mathbf{z}_u}$. Here the point $\mathbf{r}_0$ is not on the boundary, since it lies within the 2D manifold $W^U_{\mathbf{z}_\ell}$ where the 1D stable manifold $W^S_{\boldsymbol{z}_\ell}$ intersects it. Thus, the curves $\boldsymbol{\beta}_n$ can lie within a single unstable fundamental domain, assuming the proper loops are chosen appropriately, as we have shown with the loops $\boldsymbol{\alpha}_n$ in Fig. 5.3b.

Another convenient way of thinking about the invariant manifolds is to recognize that the two fixed points together with the two pole-to-pole intersection

curves form an invariant circle, which we denote by $\mathbf{z}$ without a subscript. Then the stable manifold $W^S_{\mathbf{z}}$ of the invariant circle is two-dimensional and equal to the union of $W^S_{\mathbf{z}_u}$ and $W^S_{\mathbf{z}_\ell}$. The analogous statement is true for the unstable manifold $W^U_{\mathbf{z}}$. The stable manifold $W^S_{\mathbf{z}}$ has two branches, corresponding to the upper and lower halves of the disk in Fig. 5.3a. Focusing on just the lower half-disk, we may wrap the horizontal black line into a circle, gluing the two points representing $\mathbf{z}_\ell$ together. We similarly glue the two lines representing $W^S_{\mathbf{z}_\ell}$ together, forming the image in Fig. 5.3d. This branch of $W^S_{\mathbf{z}}$ begins on the interior black circle representing $\mathbf{z}$ and extends outward. Note that each arc representing $\boldsymbol{\beta}_n$ in Fig. 5.3a is now wrapped into a circle surrounding $\mathbf{z}$ in Fig. 5.3d. We similarly represent the lower branch of $W^U_{\mathbf{z}}$ in Fig. 5.3b by the image in Fig. 5.3e.

Note that all of the original definitions of equatorial curves, proper loops, fundamental domains, indices, transition numbers, primary intersection curves, etc. introduced above for the 2D manifolds $W^S_{\mathbf{z}_u}$ and $W^U_{\mathbf{z}_\ell}$ can now be directly applied to the branches of $W^S_{\mathbf{z}}$ and $W^U_{\mathbf{z}}$. In Fig. 5.3d, we then see that the curves $\boldsymbol{\beta}_n$, combined with their missing points $\mathbf{r}_n$, are homoclinic proper loops of $W^S_{\mathbf{z}}$. This is an important realization for analyzing the topological structure of manifolds with pole-to-pole intersections. It can be much easier and more natural to analyze these manifolds as invariant manifolds of the invariant circle $\mathbf{z}$ than as invariant manifolds of the two fixed points. This shall be explored in Sec. 5.4 - Sec. 5.6.

5.2 Example 1: An Equatorial Intersection

We begin with an example of a system whose 2D stable and unstable manifolds of the fixed points $\boldsymbol{z}_u$ and $\boldsymbol{z}_\ell$ intersect at a primary intersection curve. The purpose of this example is to introduce the techniques used in Refs. [43, 62]. Figure 5.4a shows a cross section of the trellis, while Fig. 5.4b shows a top down view of the trellis. The stable (red) and unstable (blue) manifolds intersect at the equatorial intersection $\boldsymbol{p}_0$. The trellis is made up of a series of iterates of the *primary* unstable cap $W^U_{\boldsymbol{z}_\ell}[\boldsymbol{p}_0]$. Each iterate of the primary unstable cap produces a series of concatenated "bridges". A *bridge* is defined as a 2D submanifold of the unsta-

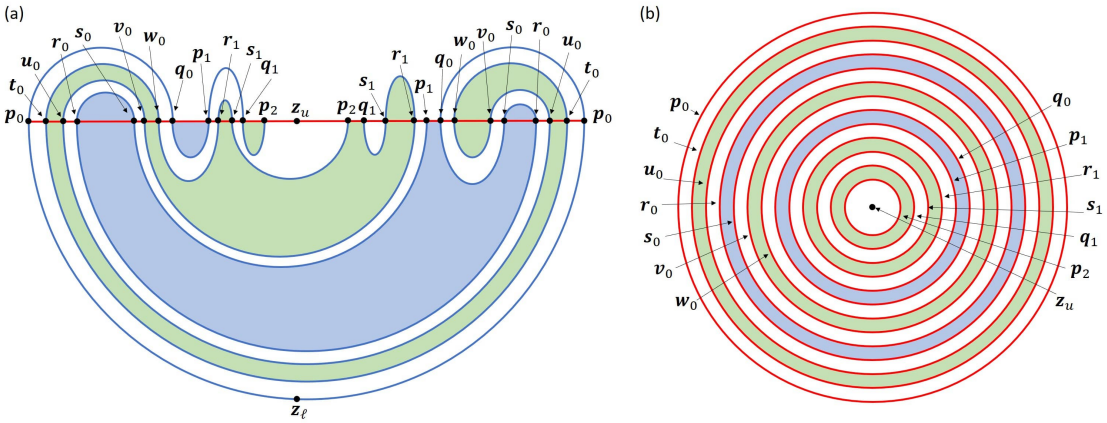

Figure 5.4: (a) A cross-section of 2D stable and unstable manifolds growing from fixed points $\boldsymbol{z}_u$ and $\boldsymbol{z}_\ell$ respectively. The stable and unstable manifolds intersect at an primary intersection curve $\boldsymbol{p}_0$. Iterating the primary unstable cap forward twice results in a series of intersections with the stable manifold. (b) A top down view of the stable manifold showing the heteroclinic intersections between the stable and unstable manifolds.

ble manifold all of whose boundary circles lie within the stable cap $W^S_{\boldsymbol{z}_u}[\boldsymbol{p}_0]$ and which does not otherwise intersect the stable cap, i.e. bridges are the pieces one obtains when the unstable manifold is cut by the stable cap. Figure 5.5 shows three examples of bridges: a "cap" with a single boundary circle, a "bundt cake" with two nested boundary circles, and a "tridge" with three nested boundary circles. The first iterate of the unstable cap $W^U_{\boldsymbol{z}_\ell}[\boldsymbol{p}_0]$ produces three bridges interior to the resonance zone: the original cap $W^U_{\boldsymbol{z}_\ell}[\boldsymbol{p}_0]$, an interior cap $W^U_{\boldsymbol{z}_\ell}[\boldsymbol{r}_0]$, and an interior tridge $W^U_{\boldsymbol{z}_\ell}[\boldsymbol{q}_0, \boldsymbol{s}_0, \boldsymbol{p}_1]$. The first iterate of $W^U_{\boldsymbol{z}_\ell}[\boldsymbol{p}_0]$ also produces two bundt cake bridges exterior to the resonance zone: $W^U_{\boldsymbol{z}_\ell}[\boldsymbol{p}_0, \boldsymbol{q}_0]$ and $W^U_{\boldsymbol{z}_\ell}[\boldsymbol{r}_0, \boldsymbol{s}_0]$. The cap $W^U_{\boldsymbol{z}_\ell}[\boldsymbol{r}_0]$ can now be iterated forward producing an additional two interior caps, $W^U_{\boldsymbol{z}_\ell}[\boldsymbol{t}_0]$ and $W^U_{\boldsymbol{z}_\ell}[\boldsymbol{u}_0]$, an interior tridge $W^U_{\boldsymbol{z}_\ell}[\boldsymbol{v}_0, \boldsymbol{w}_0, \boldsymbol{r}_1]$, and produces two exterior bundt cakes, $W^U_{\boldsymbol{z}_\ell}[\boldsymbol{t}_0, \boldsymbol{w}_0]$ and $W^U_{\boldsymbol{z}_\ell}[\boldsymbol{u}_0, \boldsymbol{v}_0]$. The forward iterate of $W^U_{\boldsymbol{z}_\ell}[\boldsymbol{p}_0, \boldsymbol{q}_0]$ produces $W^U_{\boldsymbol{z}_\ell}[\boldsymbol{p}_1, \boldsymbol{q}_1]$, $W^U_{\boldsymbol{z}_\ell}[\boldsymbol{r}_0, \boldsymbol{s}_0]$ produces $W^U_{\boldsymbol{z}_\ell}[\boldsymbol{r}_1, \boldsymbol{s}_1]$, and $W^U_{\boldsymbol{z}_\ell}[\boldsymbol{q}_0, \boldsymbol{s}_0, \boldsymbol{p}_1]$ produces $W^U_{\boldsymbol{z}_\ell}[\boldsymbol{q}_1, \boldsymbol{s}_1, \boldsymbol{p}_2]$.

Next we place *obstruction rings* in our system. These rings are obstructions in phase space designed to prevent bridges from being pulled back through the stable

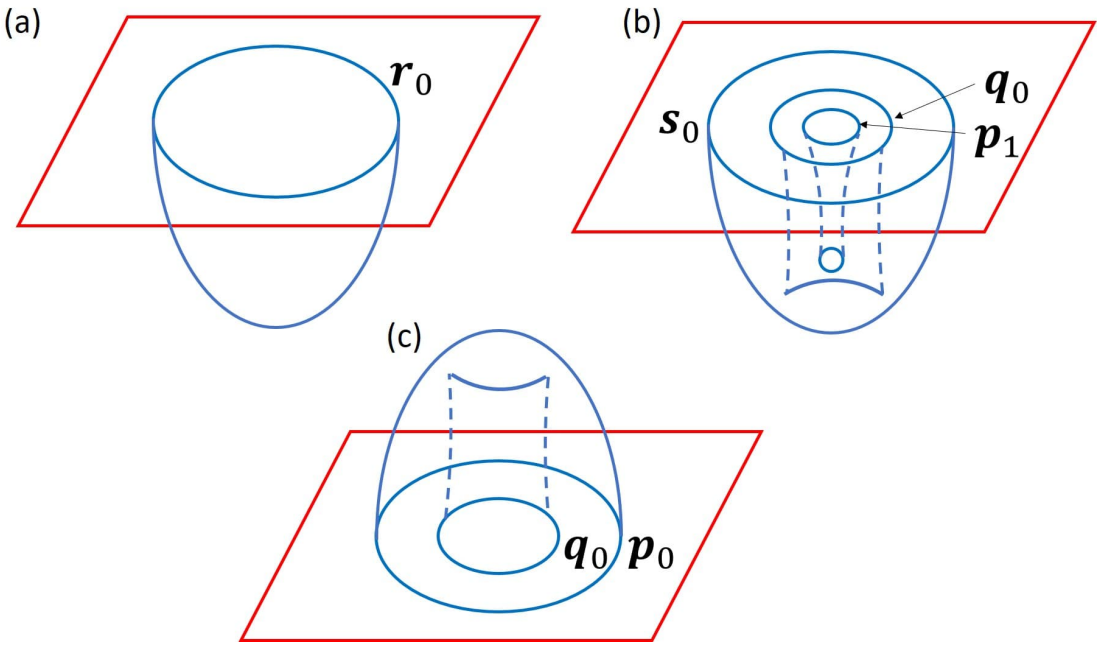

Figure 5.5: (a) The bridge $W^U_{z_\ell}[\boldsymbol{r}_0]$ which exists inside the resonance zone. With only one intersection curve, this bridge takes the form of a "cap". (b) The interior bridge $W^U_{z_\ell}[\boldsymbol{s}_0, \boldsymbol{q}_0, \boldsymbol{p}_1]$. With three nested intersection curves, the bridge takes the form of a "tridge". (c) The exterior bridge $W^U_{z_\ell}[\boldsymbol{p}_0, \boldsymbol{q}_0]$. This bridge has two intersection curves nested inside each other forming a "bundt cake".

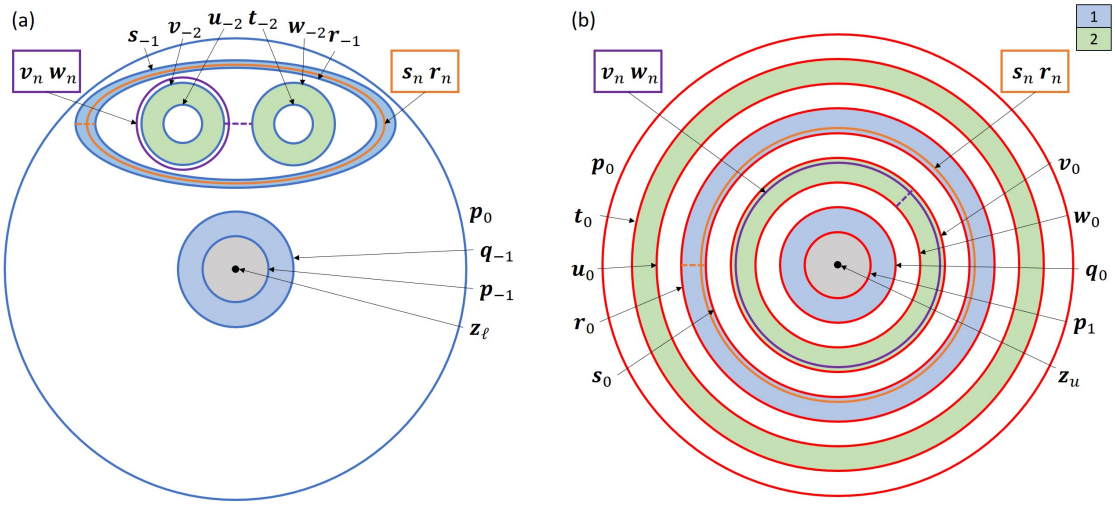

Figure 5.6: (a) Forward and (b) backward escape-time plots. The color (blue or green) indicates the number of iterates (either forward or backward) needed to escape the resonance zone. The boundaries of escape domains are heteroclinic intersection curves, blue in (a) and red in (b). Dashed lines connect pseudoneighbor pairs; note that these lines do not intersection any other heteroclinic curves. The solid lines intersecting the dashed lines are the obstruction rings, which are labeled in boxes by their corresponding pseudoneighbor pair.

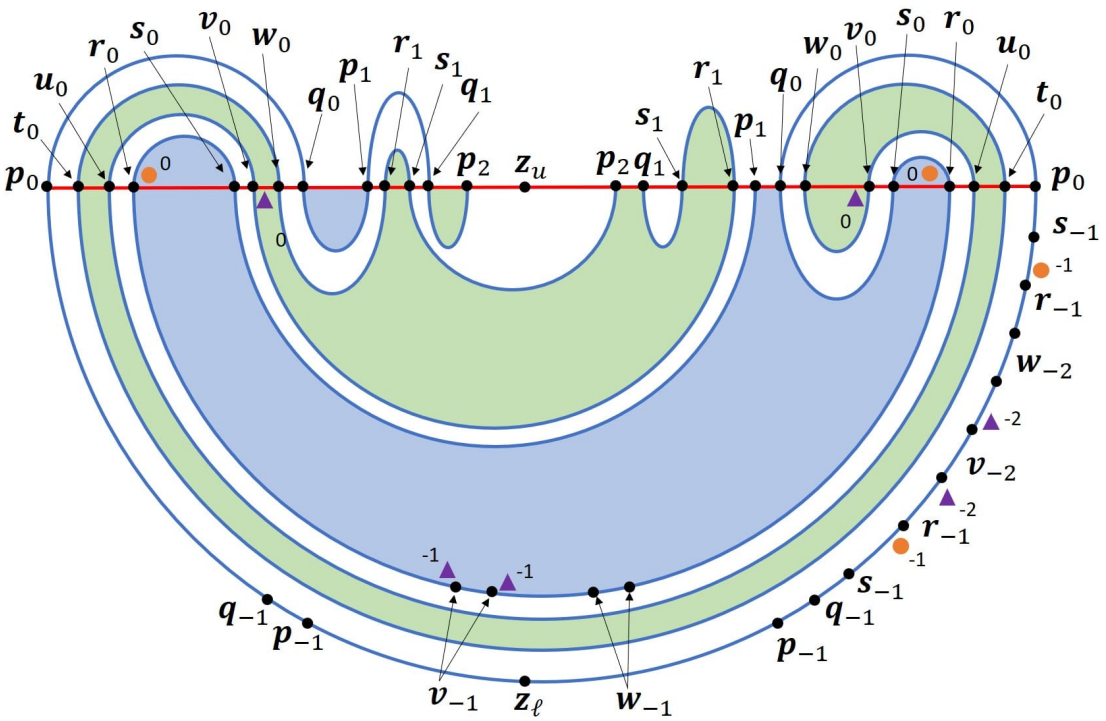

Figure 5.7: The trellis with the preiterates of the pseudoneighbors, r_0, s_0, w_0, and v_0 shown. The obstruction rings are placed slightly perturbed from one pseudoneighbor in a pair toward the other. Each obstruction ring intersects the cross-section at two points, represented either by a pair of purple triangles or orange circles.

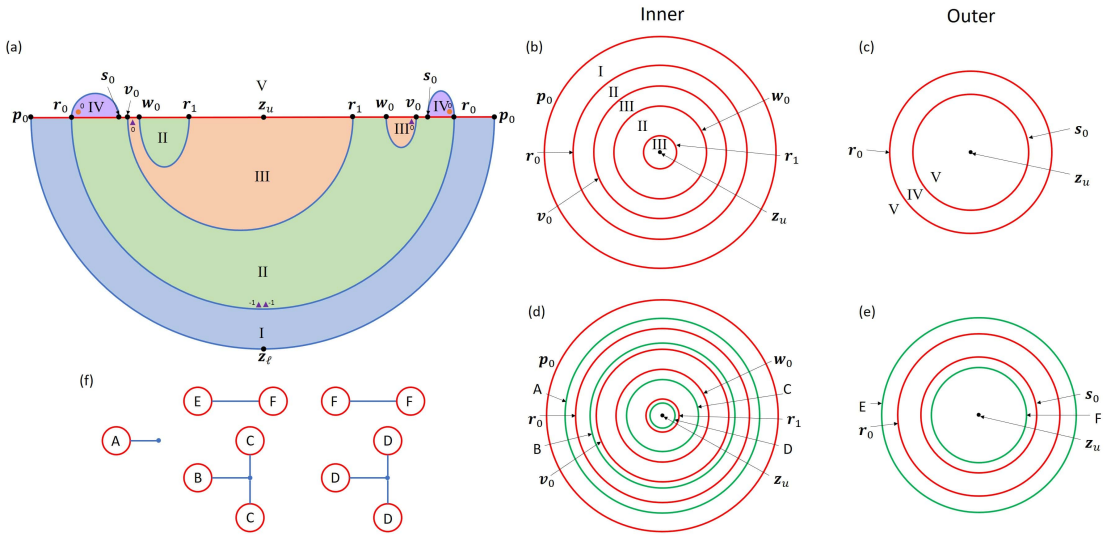

Figure 5.8: (a) A cross-section view of the primary division. Volumes partitioned by the bridges are labeled I-V. Each obstruction ring intersects the cross-section at two points, represented either by a pair of purple triangles or orange circles. (b) The inner stable division. (c) The outer stable division. The heteroclinic intersection curves that appear in the inner or outer stable division are the boundary curves of inner or outer bridges in the primary division. (d) The inner stable division with boundary classes (green). (e) The outer stable division with boundary classes (green). (f) The complete set of bridge classes for the system. Each bridge class is uniquely specified by its boundary classes (red circles with letters) connected together by the unstable manifold (blue lines).

manifold. Placement of the rings are crucial to the topological distinction of different bridges. To identify the proper placement of the rings we need to investigate the forward and backward escape-time plots of the trellis as seen in Fig. 5.6. ETPs record the number of iterates for points to exit the resonance zone. To construct the ETP we iterate points forward (or backward) from the fundamental unstable (or stable) annulus until they exit the resonance zone. Following Ref. [43] we identify pairs of *pseudoneighbor* intersection curves from the ETPs. Two heteroclinic curves $\boldsymbol{\alpha}_n$ and $\boldsymbol{\beta}_n$ form a pair of pseudoneighbors if $\boldsymbol{\alpha}_n$ and $\boldsymbol{\beta}_n$, or some iterate $\boldsymbol{\alpha}_m$ and $\boldsymbol{\beta}_m$, are adjacent on both the forward and backward ETPs, more precisely, if a line can be drawn between the two curves on both the forward and backward ETPs without intersecting any other heteroclinic curve. (An individual intersection curve can be a self-pseudoneighbor. See Ref. [43].) Note that the iterate of a pseudoneighbor pair is a pseudoneighbor pair. As seen in Fig. 5.6 there are two pseudoneighbor pairs $[\boldsymbol{v}_n, \boldsymbol{w}_n]$ and $[\boldsymbol{r}_n, \boldsymbol{s}_n]$. We draw the obstruction rings in the ETPs slightly perturbed from one of the pseudoneighbor intersections such that they lie between the two pseudoneighbors. The position of the rings in the ETPs dictate their placement in phase space as shown in Fig. 5.7.

We define homotopy classes of bridges with respect to the obstruction rings, which are viewed as ring-shaped holes in phase space. Two bridges are homotopically identified if one can be continuously distorted into the other without passing through an obstruction ring and while keeping all boundary circles attached to the stable cap. To determine these *bridge classes*, we construct the *primary division* of phase space. The primary division is a partitioning of phase space into a set of 3D domains. The primary division is obtained by cutting phase space along the following 2D manifolds:

1. the stable component of the trellis, e.g. the stable cap $W^S_{\boldsymbol{z}_u}[\boldsymbol{p}_0]$;

2. any bridge that includes a pseudoneighbor in its interior, i.e. within the bridge but not as a boundary circle;

3. any bridge with a boundary circle that is a *primary inert* pseudoneighbor—i.e. the first iterate of a pseudoneighbor to land on the stable component

of the trellis—and for which the corresponding obstruction ring is nudged toward the interior of the bridge.

Figure. 5.8a shows the primary division of Example 1. By Cutting Rule 1 we include the stable cap $W^S_{\boldsymbol{z}_u}[\boldsymbol{p}_0]$. From Cutting Rule 2 we include the unstable cap $W^U_{\boldsymbol{z}_\ell}[\boldsymbol{p}_0]$ since every pseudoneighbor eventually maps into it in the backward-time direction. Furthermore the cap $W^U_{\boldsymbol{z}_\ell}[\boldsymbol{r}_0]$ is also included by Rule 2 since it contains the pseudoneighbors $\boldsymbol{v}_{-1}$ and $\boldsymbol{w}_{-1}$. Finally we include the bridges $W^U_{\boldsymbol{z}_\ell}[\boldsymbol{r}_0, \boldsymbol{s}_0]$ and $W^U_{\boldsymbol{z}_\ell}[\boldsymbol{v}_0, \boldsymbol{w}_0, \boldsymbol{r}_1]$ by Rule 3. In total this partitions phase space into five regions (Fig. 5.8a).

The stable cap is in turn partitioned by the boundary curves of the bridges that cut up phase space into the primary division. In fact, we define two primary divisions of the stable cap, one defined by the boundaries of bridges outside of the resonance zone and one by the boundaries of bridges inside the resonance zone. Figure 5.8b shows the inner stable division while Fig. 5.8c shows the outer stable division. The primary divisions of the stable cap define two sets of homotopy classes (inner and outer) for curves in the stable cap. We call these *boundary classes*. Each bridge class can be uniquely specified by its boundary classes. The boundary classes for Example 1 are the green curves in Fig. 5.8d and Fig. 5.8e.

We denote a bridge class using a double bracket notation with the boundary classes that specify the bridge class enclosed. Example 1 has three inner bridge classes, the cap $[\![A]\!]$, the tridge $[\![B, C, C]\!]$, and the tridge $[\![D, D, D]\!]$, and two outer bridge classes, the bundt cakes $[\![D, E]\!]$ and $[\![F, F]\!]$. Bridge classes can also be represented in a graphic form as seen in Fig. 5.8f. This form is more convenient to represent the concatenation of bridge classes. Each boundary class is represented by a letter surrounded by a red circle, indicating its intersection with the stable manifold. These circles are connected with blue lines representing the connecting unstable surface.

To understand how the bridge classes are stretched and folded when they are iterated forward, we create a new division of phase space called the secondary division. The secondary division is constructed by cutting along the following surfaces:

1. the stable component of the trellis, e.g. the cap $W^S_{\boldsymbol{z}_u}[\boldsymbol{p}_0]$;

2. the forward iterate of every bridge with a pseudoneighbor in its interior, i.e. the iterate of those bridges included by Rule 2 of the primary division.

Cutting phase space this way generates Fig. 5.9a. This division of phase space creates eleven domains labeled with lower-case Roman numerals. The boundary of each domain is made up of some number of bridges and some number of pieces of the stable manifold. For example, region i is bounded by the bridges $W^U_{\boldsymbol{z}_\ell}[\boldsymbol{p}_0]$, $W^U_{\boldsymbol{z}_\ell}[\boldsymbol{t}_0]$, and the stable piece $W^S_{\boldsymbol{z}_u}[\boldsymbol{p}_0, \boldsymbol{t}_0]$. Just like the primary division, the boundary curves of the bridges that make up the secondary division divide the stable cap in two ways. Figure 5.9b and Fig. 5.9c show the inner and outer secondary divisions of the stable cap. The bold red curves represent boundary curves that also occur in the primary division. Green curves are the boundary classes.

We specify that two domains of the secondary division are *connected* if they share a common boundary along a piece of the stable fundamental annulus. This relationship is represented graphically by the *connection graph*. See Fig. 5.9d. Every domain of the secondary division is represented as a circular node in the connection graph. Each circular node is connected to some number of red boxes, where each box represents one connected piece of the stable boundary for that domain. These pieces are labeled by their boundary curves. Two domains that are connected to one another are attached to a common red box, representing the mutual boundary between them. For example, the domains i and x are separated by the piece of the stable annulus $W^S_{\boldsymbol{z}_u}[\boldsymbol{t}_0, \boldsymbol{p}_0]$. Note that the connection graph for Example 1 has three connected components.

We map all of the bridge classes forward one iterate. We begin with the class $[\![A]\!]$, which includes the bridge $W^U_{\boldsymbol{z}_\ell}[\boldsymbol{p}_0]$. This class is specified by the boundary class A; a representative curve for A can be chosen to lie within the domain $W^S_{\boldsymbol{z}_u}[\boldsymbol{p}_0, \boldsymbol{r}_0]$ (as seen in Fig. 5.8d). The forward iterate of this representative curve must lie within the domain $W^S_{\boldsymbol{z}_u}[\boldsymbol{p}_1, \boldsymbol{r}_1]$. This curve is of boundary class C, as seen by the inner secondary division (Fig. 5.9b). Note that even though the green curve C is not between the curves $\boldsymbol{p}_1$ and $\boldsymbol{r}_1$ in Fig. 5.9b, it could be deformed to lie between these two curves without passing through a curve from the primary division (bold

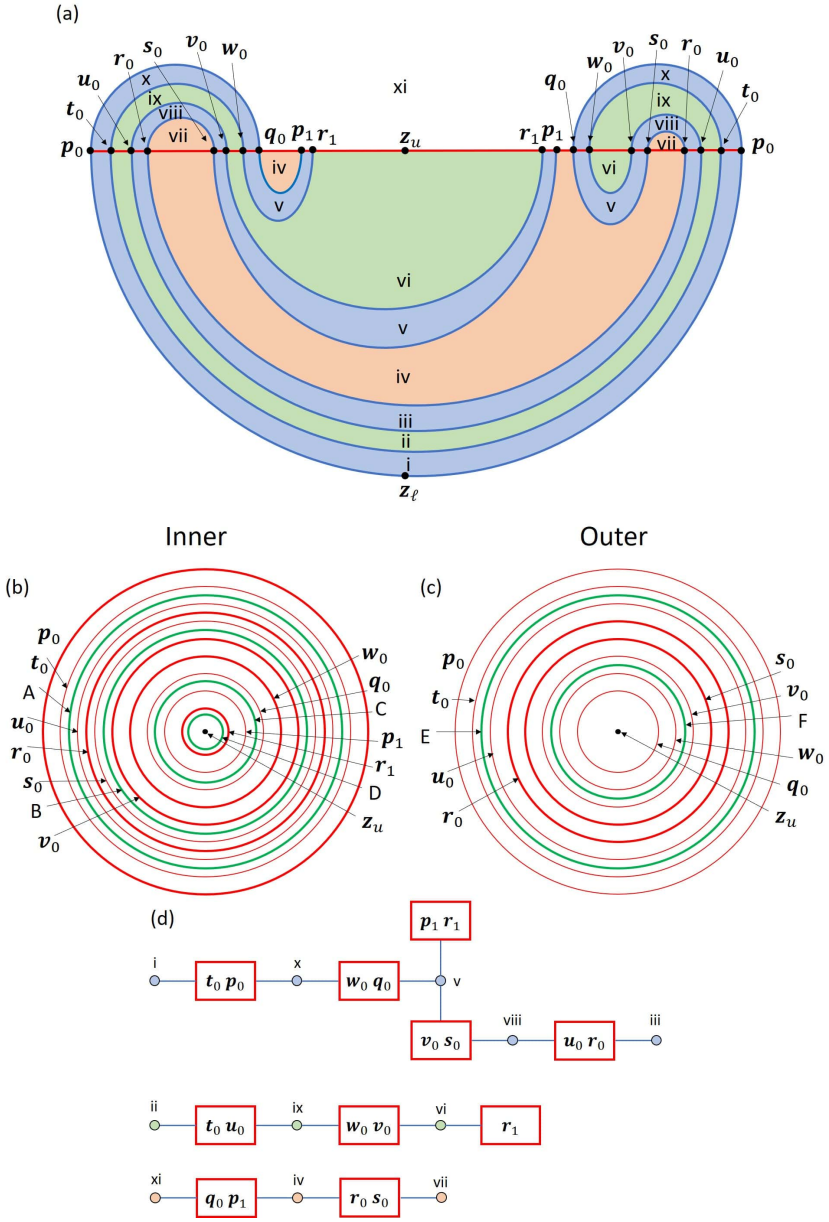

Figure 5.9: (a) A cross section view of the secondary division of phase space. Volumes partitioned by bridges are labeled i-xi. (b) The inner secondary stable division. (c) The outer secondary stable division. Curves that also appear in the primary division are shown in bold while those that appear exclusively in the secondary division are not. Boundary classes are shown in green. (d) The connection graph of the secondary division. The connection graph identifies how the partitioned volumes of the secondary division are connected across the stable fundamental annulus.

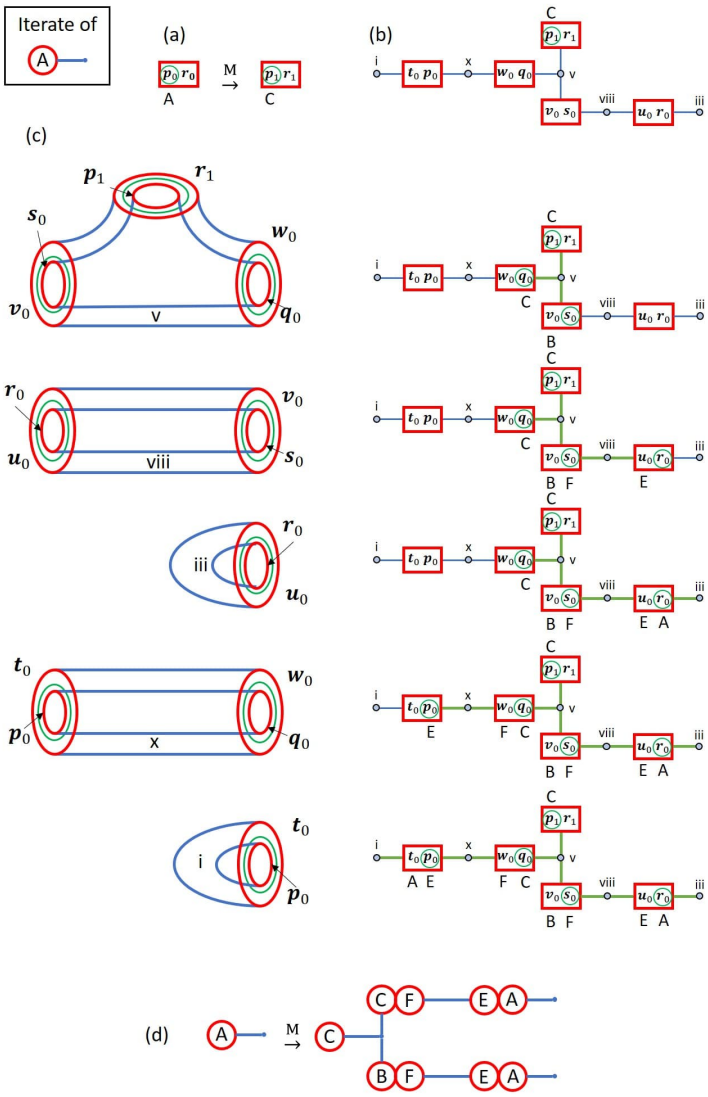

Figure 5.10: A step-by-step illustration of the process to iterate $[\![A]\!]$ forward. (a) The forward iterate of the boundary class A, represented by the green circle, is the boundary class C, represented by the second green circle. (b) The component of the connection graph used to identify the forward iterate, showing boundary class C. (c) The step-by-step process identifying the forward iterate of $[\![A]\!]$. Each of the regions the forward iterate passes through is shown on the left, while the connections made are shown on the right. Boundary classes are labeled next to each box. (d) The final concatenation of bridge classes that make up the forward iterate of $[\![A]\!]$.

red curve).

Figure 5.10 shows how to construct the forward iterate of $[\![A]\!]$. In Fig. 5.10a we show how the boundary class A maps forward. First the forward iterate of the domain $W^S_{\boldsymbol{z}_u}[\boldsymbol{p}_0, \boldsymbol{r}_0]$ is $W^S_{\boldsymbol{z}_u}[\boldsymbol{p}_1, \boldsymbol{r}_1]$, both shown as red boxes in Fig. 5.10a. Since A is between $\boldsymbol{p}_0$ and $\boldsymbol{r}_0$, we circle $\boldsymbol{p}_0$ in green. Since $\boldsymbol{p}_0$ iterates to $\boldsymbol{p}_1$, we circle $\boldsymbol{p}_1$ in green as well. As discussed above this curve is of boundary class C. Figure 5.10b shows the component of the connection graph containing $W^S_{\boldsymbol{z}_u}[\boldsymbol{p}_1, \boldsymbol{r}_1]$. As in Fig. 5.10a we circle $\boldsymbol{p}_1$ and note that it is of boundary class C. We know from the connection graph that the forward iterate of $[\![A]\!]$ must enter region v. The first row of Fig. 5.10c shows a topological representation of region v bounded by two nested tridges. Since the unstable manifold cannot intersect itself, the forward iterate of $[\![A]\!]$ is forced to intersect the domain $W^S_{\boldsymbol{z}_u}[\boldsymbol{w}_0, \boldsymbol{q}_0]$, whose intersection curve is of boundary class C, and the domain $W^S_{\boldsymbol{z}_u}[\boldsymbol{s}_0, \boldsymbol{v}_0]$, whose intersection curve is of boundary class B. We shade the connection graph lines in green to show how the iterate occupies region v, while placing green circles around $\boldsymbol{q}_0$ and $\boldsymbol{s}_0$, representing the intersection curves. Due to the intersection curve around $\boldsymbol{s}_0$, the forward iterate of $[\![A]\!]$ is forced to enter region viii. Since region viii is exterior, we note that a boundary curve between $\boldsymbol{s}_0$ and $\boldsymbol{v}_0$ is of the class F with respect to the outer primary stable division (Fig. 5.9c). Examining the topology of region viii on the second row of Fig. 5.10c, we see that the forward iterate of $[\![A]\!]$ is forced to intersect the domain $W^S_{\boldsymbol{z}_u}[\boldsymbol{r}_0, \boldsymbol{u}_0]$. We place a green circle around $\boldsymbol{r}_0$, which represents boundary class E. Next the iterate of $[\![A]\!]$ passes through the inner region iii. From the inner perspective the curve around $\boldsymbol{r}_0$ has boundary class A. The topological representation of region iii on row three of Fig. 5.10c consists of two nested caps. The minimal topological form for the iterate of $[\![A]\!]$ within region iii is a terminating cap. Returning to the curve around $\boldsymbol{q}_0$, we see it generates a similar process as the curve around $\boldsymbol{s}_0$, occupying regions x and i as seen in rows four and five of Fig. 5.10c. Putting all this together gives the forward iterate of $[\![A]\!]$ seen in Fig. 5.10d.

The iterates of the remaining four bridge classes in Fig. 5.8f are easier to construct. In the case of bridge class $[\![E, F]\!]$, we look at the representative bridge

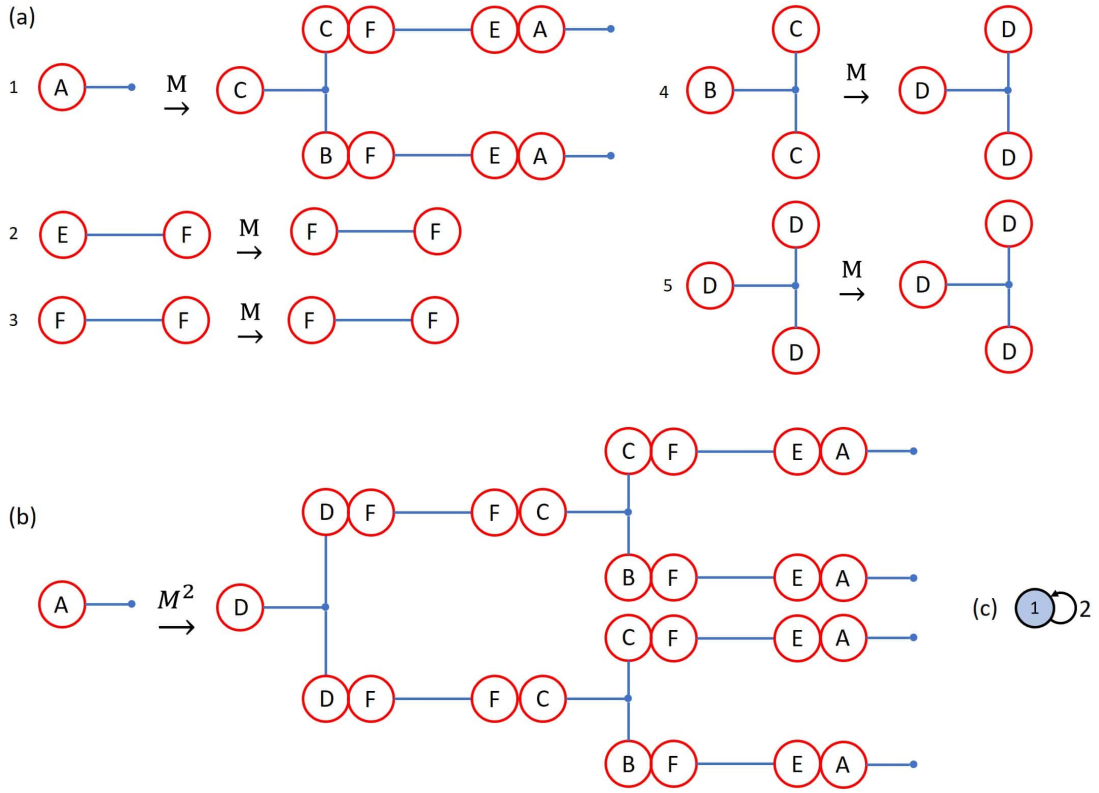

Figure 5.11: (a) The complete set of bridge classes for the dynamics and their forward iterates. (b) Bridge class $[\![A]\!]$ iterated forward twice. After two iterations, $[\![A]\!]$ produces four copies of itself. (c) The transition graph for the single active bridge class.

$W^U_{\boldsymbol{z}_\ell}[\boldsymbol{p}_0, \boldsymbol{q}_0]$. The forward iterate of $W^U_{\boldsymbol{z}_\ell}[\boldsymbol{p}_0, \boldsymbol{q}_0]$ is $W^U_{\boldsymbol{z}_\ell}[\boldsymbol{p}_1, \boldsymbol{q}_1]$, which is a single bridge, of class $[\![F, F]\!]$. The forward iterate of $W^U_{\boldsymbol{z}_\ell}[\boldsymbol{p}_1, \boldsymbol{q}_1]$ is $W^U_{\boldsymbol{z}_\ell}[\boldsymbol{p}_2, \boldsymbol{q}_2]$, also of class $[\![F, F]\!]$. Thus $[\![F, F]\!]$ maps to itself. Since all iterates of $[\![E, F]\!]$ consist of a single bridge class, we say that $[\![E, F]\!]$ is *inert*. By the same logic, $[\![F, F]\!]$ is also inert. The same process is also applied to the remaining two bridge classes, which are also inert. Figure 5.11a summarizes the complete set of dynamics for Example 1. Note that $[\![A]\!]$ is not inert because it produces multiple bridge classes upon iteration. A bridge class that is not inert is called *active*.

Having determined the iterates of all the bridge classes of the trellis, we know the forced topology of the unstable manifold. For example, suppose we wanted to iterate the bridge class of the unstable cap $W^U_{\boldsymbol{z}_\ell}[\boldsymbol{p}_0]$ forward twice. We would

first iterate the bridge class $[\![A]\!]$, to which $W^U_{\boldsymbol{z}_\ell}[\boldsymbol{p}_0]$ belongs, and then iterate each resultant bridge class forward, resulting in Fig. 5.11b. [Note that the dynamics produced by iterating $[\![A]\!]$ forward twice is exactly the trellis in Fig. 5.4.] Additionally, a lower bound of the topological entropy can be determined from the symbolic dynamics. We first create the *transition matrix* T, where the component T_{ij} records the number of times that bridge class number i appears in the iterate of bridge class number j. The log of the largest eigenvalue of T is a lower bound of the topological entropy. It is sufficient to only consider the submatrix of the active bridge classes, since inert bridge classes do not contribute to the topological entropy. In Example 1 there is a single active bridge class, $[\![A]\!]$, whose iterate contains two copies of $[\![A]\!]$. This produces the one-by-one matrix $\mathsf{T} = (2)$, which generates $h = \ln 2$ as a lower bound to the topological entropy of the original map M. Note that a transition matrix can be represented as a transition graph, as in Fig. 5.11c. In future examples we will just show the transition graph.

5.3 Example 2: A Non-Equatorial Intersection

Example 1 examined the case where there is a primary intersection curve $\boldsymbol{p}_0$ between the stable cap and primary unstable cap. Example 2 explores a case where there is no primary intersection curve between the stable and unstable caps, but there are pole-to-pole intersection curves, as in Fig. 5.2b. Despite the lack of a well defined resonance zone, we can still extract homotopic lobe dynamics on a subset of the full trellis.

Figure 5.12 constructs the topology of the trellis in Example 2. We define the stable cap and primary unstable cap as the submanifolds of the stable and unstable manifolds up to their first intersections with the xy-plane (Fig. 5.12a). We label these intersections $\boldsymbol{L}^S_0$ and $\boldsymbol{L}^U_0$ respectively, and we assume that they are proper loops. We use these curves to form the stable and unstable fundamental annuli $W^S_{\boldsymbol{z}_u}[\boldsymbol{L}^S_0, \boldsymbol{L}^S_1]$ and $W^U_{\boldsymbol{z}_\ell}[\boldsymbol{L}^U_{-1}, \boldsymbol{L}^U_0]$. The curve $\boldsymbol{L}^U_0$ is broken into an interior segment $\boldsymbol{L}^U_{i0}$ and exterior segment $\boldsymbol{L}^U_{e0}$. Figure 5.12a shows the first iterate of $\boldsymbol{L}^U_{i0}$ and the unstable manifold between them. The curves $\boldsymbol{L}^U_0$ and $\boldsymbol{L}^U_1$ intersect the pole-to-pole

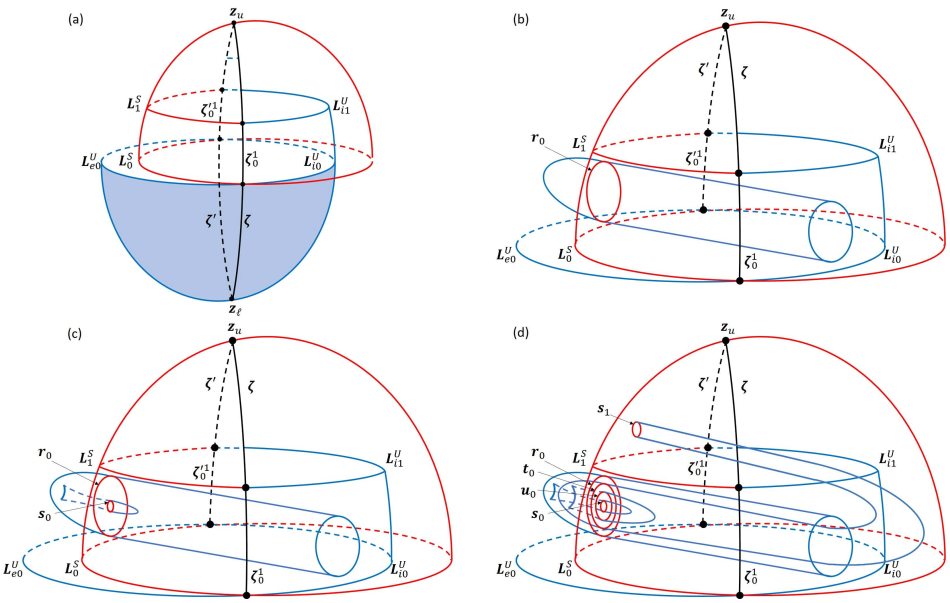

Figure 5.12: A sequence of images representing trellises with increasing complexity. (a) A trellis with no additional intersections beyond the pole-to-pole intersections $\boldsymbol{\zeta}$ and $\boldsymbol{\zeta}'$. (b) A trellis where the unstable manifold inside the stable cap is stretched across to intersect the stable cap. (c) A trellis where the cap $W^U_{\boldsymbol{z}_\ell}[\boldsymbol{r}_0]$ from (b) is pulled back through the stable cap. (d) The trellis in (c) with the forward iterate of $W^U_{\boldsymbol{z}_\ell}[\boldsymbol{s}_0]$ shown.

intersection curves $\boldsymbol{\zeta}$ and $\boldsymbol{\zeta}'$ and define the segments $\boldsymbol{\zeta}_0^1$ and $\boldsymbol{\zeta}_0'^1$ between them. This allows us to define the interior half-annulus $W^U_{\boldsymbol{z}_\ell}[\boldsymbol{\zeta}_0^1, \boldsymbol{L}^U_{i0}, \boldsymbol{\zeta}_0'^1, \boldsymbol{L}^U_{i1}]$.

In Fig. 5.12b, we modify the dynamics of Fig. 5.12a by pushing a piece of the half-annulus $W^U_{\boldsymbol{z}_\ell}[\boldsymbol{\zeta}_0^1, \boldsymbol{L}^U_{i_0}, \boldsymbol{\zeta}_0'^1, \boldsymbol{L}^U_{i_1}]$ across the interior region until it intersects the stable cap at $\boldsymbol{r}_0$. This creates the unstable submanifold $W^U_{\boldsymbol{z}_\ell}[\boldsymbol{\zeta}_0^1, \boldsymbol{L}^U_{i_0}, \boldsymbol{\zeta}_0'^1, \boldsymbol{L}^U_{i_1}, \boldsymbol{r}_0]$. The intersection $\boldsymbol{r}_0$ lies on the fundamental stable annulus $W^S_{\boldsymbol{z}_u}[\boldsymbol{L}^S_0, \boldsymbol{L}^S_1]$. The trellis in Fig. 5.12b still does not generate any topological entropy as no new heteroclinic intersections are forced to exist at any finite iterate. In Fig. 5.12c we again modify the dynamics by introducing additional structure. We take the cap $W^U_{\boldsymbol{z}_\ell}[\boldsymbol{r}_0]$ in Fig. 5.12b and push a part of it back through the stable cap $W^S_{\boldsymbol{z}_u}[\boldsymbol{L}^S_0]$ forming the intersection $\boldsymbol{s}_0$, as seen in Fig. 5.12c. While this forms an interior cap $W^U_{\boldsymbol{z}_\ell}[\boldsymbol{s}_0]$ and exterior bundt cake $W^U_{\boldsymbol{z}_\ell}[\boldsymbol{r}_0, \boldsymbol{s}_0]$, this still does not produce any topological entropy. In Fig. 5.12d we add to the trellis in Fig. 5.12c by iterating the interior cap $W^U_{\boldsymbol{z}_\ell}[\boldsymbol{s}_0]$ forward. This iterate is stretched back to the fundamental stable annulus producing the interior macaroni $W^U_{\boldsymbol{z}_\ell}[\boldsymbol{s}_1, \boldsymbol{t}_0]$, the exterior bundt cake $W^U_{\boldsymbol{z}_\ell}[\boldsymbol{t}_0, \boldsymbol{u}_0]$, and the interior cap $W^U_{\boldsymbol{z}_\ell}[\boldsymbol{u}_0]$. The trellis in Fig. 5.12d has forced dynamics with non-zero topological entropy as we shall show.

Some unstable submanifolds such as $W^U_{\boldsymbol{z}_\ell}[\boldsymbol{L}^U_0]$ and $W^U_{\boldsymbol{z}_\ell}[\boldsymbol{\zeta}_0^1, \boldsymbol{L}^U_{i0}, \boldsymbol{\zeta}_0'^1, \boldsymbol{L}^U_{i1}, \boldsymbol{r}_0]$ are not bridges because their boundaries do not solely lie on the stable cap. This makes defining escape times, primary divisions, and secondary divisions awkward. Therefore in this example we focus solely on the unstable submanifolds that are true bridges and apply HLD to those submanifolds only. Fig 5.13 shows the relevant bridges.

Since we do not have a well defined resonance zone, we avoid ETPs and work solely with the heteroclinic intersection curves directly. Figure 5.14 shows the stable and unstable fundamental annuli with the heteroclinic intersections present in Fig. 5.13. We use these plots the same way we use the ETPs to identify pseudoneighbor pairs and place obstruction rings. Looking at both the annuli in Fig. 5.14a and Fig. 5.14b, we see that $[\boldsymbol{t}_n, \boldsymbol{u}_n]$ form the sole pseudoneighbor pair. We place an obstruction ring slightly perturbed from $\boldsymbol{u}_n$ toward $\boldsymbol{t}_n$ in Fig. 5.14. Two of these obstruction rings are present in Fig. 5.13 represented by two pairs of

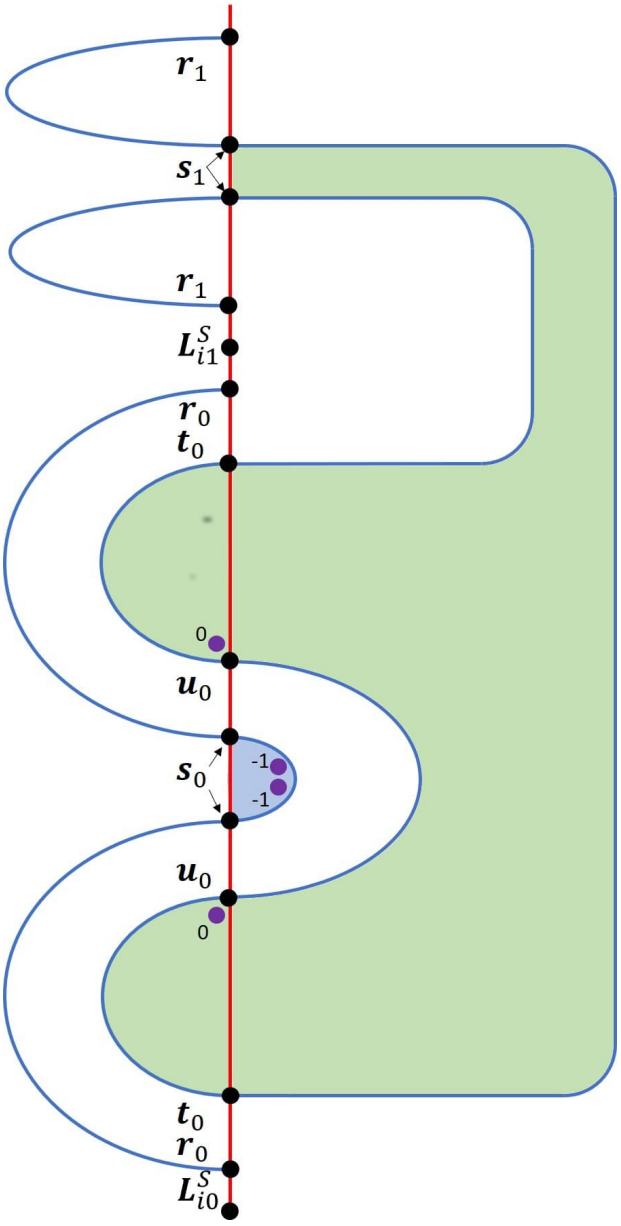

Figure 5.13: A cross section of Fig. 5.12d showing only the bridges, all of whose boundary curves lie entirely within the stable cap. Only the part of the stable cap containing these boundary curves is shown.

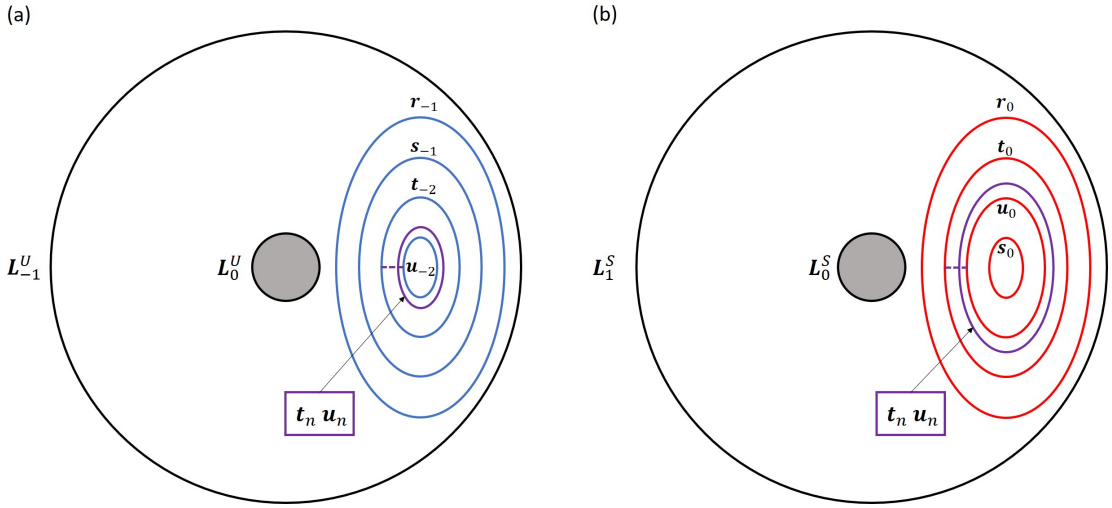

Figure 5.14: (a) The heteroclinic intersections that lie on the unstable fundamental annulus $W^U_{\boldsymbol{z}_\ell}[\boldsymbol{L}^U_{-1}, \boldsymbol{L}^U_0]$. (b) The heteroclinic intersections that lie on the stable fundamental annulus $W^S_{\boldsymbol{z}_u}[\boldsymbol{L}^S_0, \boldsymbol{L}^S_1]$. Pseudoneighbor pairs are identified based on curves that are adjacent in both the forward and backward fundamental annuli.

purple dots labeled with their iterate number.

With the obstruction rings placed we construct the primary division of phase space in Fig 5.15a. We include the bridge $W^U_{\boldsymbol{z}_\ell}[\boldsymbol{s}_0]$ based on Rule 2 of constructing the primary division in Sec. 5.2 and $W^U_{\boldsymbol{z}_\ell}[\boldsymbol{t}_0, \boldsymbol{u}_0]$ based on Rule 3. We omit the unstable cap $W^U_{\boldsymbol{z}_\ell}[\boldsymbol{L}^U_0]$ since it is not a bridge. Using the primary division, we construct the inner and outer stable divisions in Fig. 5.15b and Fig. 5.15c. We identify the boundary classes A through D from boundary curves in Fig. 5.13. Examining Fig. 5.13 we find bridge classes $[\![A]\!]$, $[\![A, B]\!]$ and $[\![C, D]\!]$ as seen in Fig. 5.15d.

To determine the iterate of the bridge class $[\![A]\!]$, let us consider the iterate of the representative bridge $W^U_{\boldsymbol{z}_\ell}[\boldsymbol{s}_0]$. We iterate the boundary curve $\boldsymbol{s}_0$ forward to $\boldsymbol{s}_1$, as seen in Fig. 5.16a. Curve $\boldsymbol{s}_1$ is of boundary class B (Fig 5.15b). Following Fig. 5.16a, $\boldsymbol{s}_1$ is connected to $\boldsymbol{t}_0$ by the interior macaroni $W^U_{\boldsymbol{z}_\ell}[\boldsymbol{s}_1, \boldsymbol{t}_0]$. Curve $\boldsymbol{t}_0$ has boundary class A on the interior so that $W^U_{\boldsymbol{z}_\ell}[\boldsymbol{s}_1, \boldsymbol{t}_0]$ is of bridge class $[\![B, A]\!]$. To the left of the stable manifold, boundary curve $\boldsymbol{t}_0$ is connected to $\boldsymbol{u}_0$ by a bundt cake forming the bridge $W^U_{\boldsymbol{z}_\ell}[\boldsymbol{t}_0, \boldsymbol{u}_0]$. On the exterior $\boldsymbol{t}_0$ and $\boldsymbol{u}_0$ have boundary classes

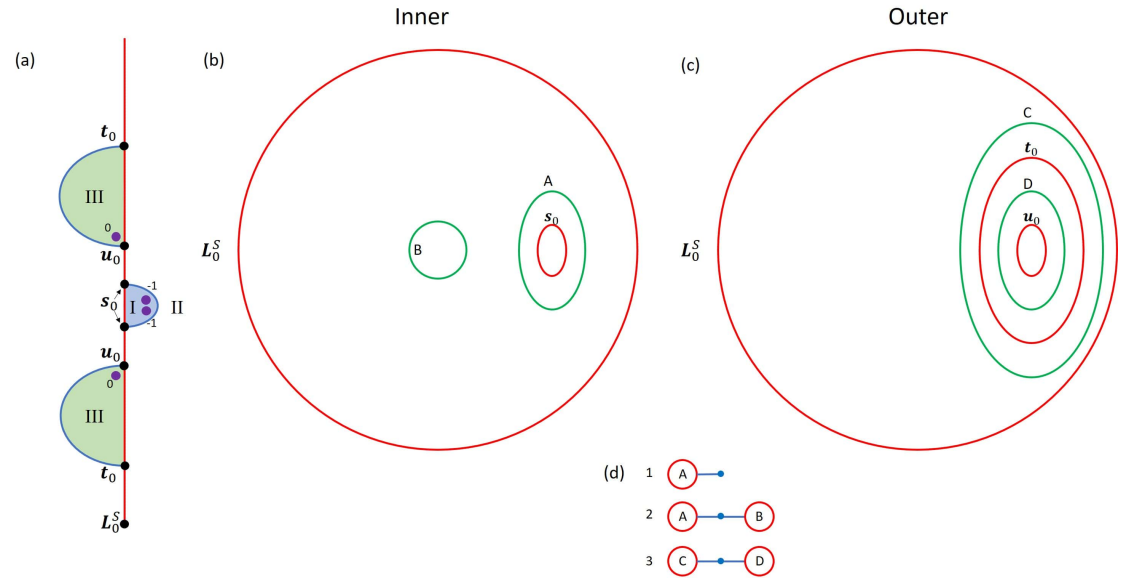

Figure 5.15: (a) The primary division of phase space. (b) The inner stable division. (c) The outer stable division. (d) The bridge classes that make up the system.

C and D respectively. This means $W^U_{\boldsymbol{z}_\ell}[\boldsymbol{t}_0, \boldsymbol{u}_0]$ belongs to bridge class $[\![C, D]\!]$. To the right of the stable manifold, $\boldsymbol{u}_0$ is terminated by a cap. $\boldsymbol{u}_0$ also has interior boundary class A so that this cap $W^U_{\boldsymbol{z}_\ell}[\boldsymbol{u}_0]$ belongs to bridge class $[\![A]\!]$. Putting all this together, the iterate of $[\![A]\!]$ is the concatenation of $[\![B, A]\!]$, $[\![C, D]\!]$, and $[\![A]\!]$ as shown in Fig. 5.16b.

We determine the iterate of the bridge class $[\![A, B]\!]$ by examining the iterate of the representative bridge $W^U_{\boldsymbol{z}_\ell}[\boldsymbol{t}_0, \boldsymbol{s}_1]$. The forward iterates of $\boldsymbol{t}_0$ and $\boldsymbol{s}_1$ are $\boldsymbol{t}_1$ and $\boldsymbol{s}_2$, each placed as in Fig. 5.16c. The curves $\boldsymbol{t}_1$ and $\boldsymbol{s}_2$ each have boundary class B. Curve $\boldsymbol{t}_1$ cannot be directly connected to curve $\boldsymbol{s}_2$ by a macaroni, because this macaroni would then intersect the bridge $W^U_{\boldsymbol{z}_\ell}[\boldsymbol{t}_0, \boldsymbol{s}_1]$. To properly connect $\boldsymbol{t}_1$ to $\boldsymbol{s}_2$, the manifold is forced to have an additional intersection around $\boldsymbol{t}_0$ as in Fig. 5.16c. This new boundary has internal boundary class A. Yielding a bridge class $[\![B, B, A]\!]$ to the right of the stable manifold. On the left this new intersection curve has boundary class C. Following Fig. 5.16c this intersection curve is connected by a bundt cake to a new intersection curve between $\boldsymbol{u}_0$ and $\boldsymbol{s}_0$. This new intersection has outer boundary class D meaning the bundt cake has bridge class $[\![C, D]\!]$. To the right of the stable manifold, the intersection curve between $\boldsymbol{u}_0$ and $\boldsymbol{s}_0$ is terminated

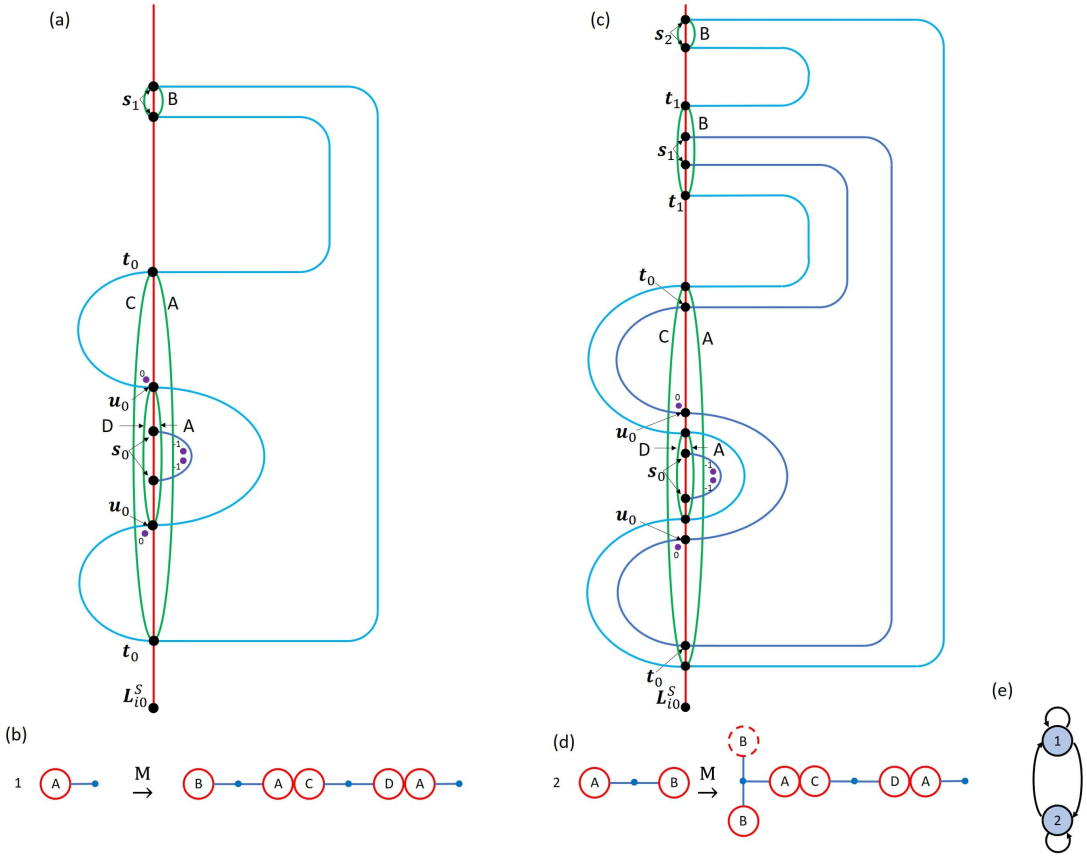

Figure 5.16: We show the construction of the forward iterate of each of the active bridge classes. (a) and (c) shows the active bridge being iterated forward in blue. The forward iterate of the bridge class is shown in cyan. The heteroclinic intersection curves of the forward iterate are in green and the boundary class they belong to labeled for both the inner and outer stable division. (b) and (d) show the symbolic equation for the two active bridge classes. (e) is the transition graph of the two active classes.

by a cap of bridge class $[\![A]\!]$. In summary the iterate of bridge class $[\![A, B]\!]$ is the concatenation of the bridge classes in Fig. 5.16d. In the iterate of $[\![A, B]\!]$ a new bridge class $[\![A, B, B]\!]$ appears. The iterate of $[\![A, B, B]\!]$ is identical to the iterate of $[\![A, B]\!]$ except that $[\![A, B, B]\!]$ is replaced by the new bridge $[\![A, B, B, B]\!]$. This pattern repeats itself with each iterate of $[\![A, B, B, ...]\!]$ producing a new bridge class with an additional B boundary class. All of these additional B boundary classes are unimportant to the symbolic dynamics. (They are inert in the sense of Ref. [43].) We therefore indicate the additional B boundary class with a dashed circle in Fig. 5.16d. Furthermore, we identify all of these classes as one symbol in the symbolic dynamics. The result is that the system has two active bridge classes $[\![A]\!]$ and $[\![A, B]\!]$ each of which produces one copy of itself and one copy of the other.

From the iterates of the active classes, we get the transition graph shown in Fig. 5.16(e). Each iterate of bridge class 1, i.e. $[\![A]\!]$, produces one copy of class 1 and class 2, i.e. $[\![A, B]\!]$. Bridge class 2 also produces a copy of both bridge classes 1 and 2. From the corresponding transition matrix, we find a topological entropy of $h = \ln 2$.

We have shown here that HLD can be applied to manifolds in a localized region of phase space without needing a well defined resonance zone. In Example 4 we revisit this geometry in the context of a well defined resonance zone and provide an alternative analysis.

5.4 Example 3: A Simple Non-Equatorial Intersection

This section explores the case in Fig. 5.17, where it is more beneficial to look at the 2D stable and unstable manifolds extending from the invariant circle $\boldsymbol{z}$ instead of from the fixed points. This example is reversible, as discussed in Sec. 3.1, with symmetry operator $S(x, y, z) = (-x, y, -z)$.

In Fig. 5.17 the 2D stable manifold (red) and 1D unstable manifold (cyan) extend from the upper fixed point $\boldsymbol{z}_u$ and intersect at the point labeled $\boldsymbol{p}_0$ on the left. Similarly the 2D unstable manifold (blue) and 1D stable manifold (magenta)

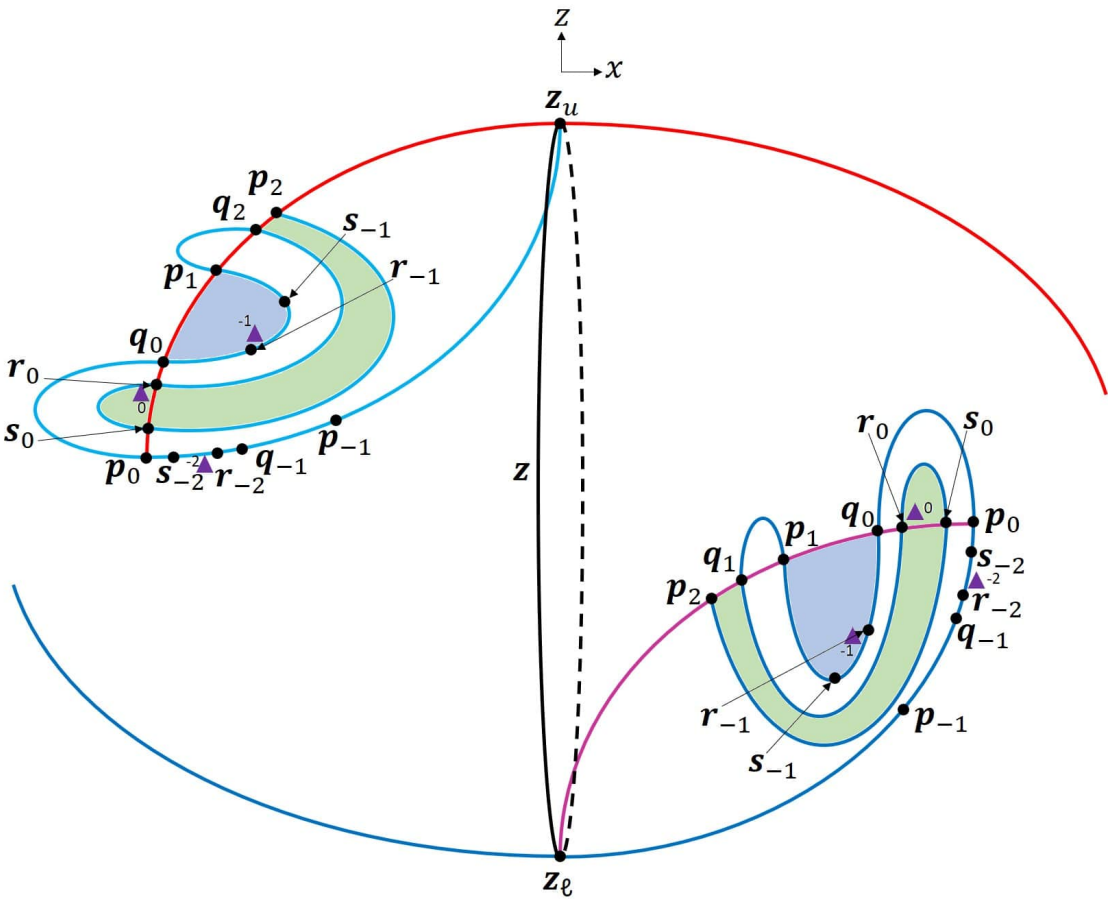

Figure 5.17: An example of invariant manifolds attached to the invariant circle $\boldsymbol{z}$. The stable manifold of the invariant circle $\boldsymbol{z}$ is the union of the 1D stable manifold (magenta) extending from the lower fixed point and the 2D stable manifold (red) extending from the upper fixed point. Similarly the unstable manifold of $\boldsymbol{z}$ is the union of the 1D unstable manifold (cyan) extending from the upper fixed point and the 2D unstable manifold (blue) extending from the lower fixed point. The stable and unstable manifolds of $\boldsymbol{z}$ intersect at several 1D curves marked with dots. The obstruction ring (purple triangles) are placed slightly perturbed from $\boldsymbol{r}_n$ toward $\boldsymbol{s}_n$.

extend from the lower fixed point $\boldsymbol{z}_\ell$ and intersect at the point labeled $\boldsymbol{p}_0$ on the right. The 1D unstable curve $W^U_{\boldsymbol{z}_u}$ lies within the 2D unstable manifold of $\boldsymbol{z}$; similarly, the 1D stable curve $W^S_{\boldsymbol{z}_\ell}$ lies within the 2D stable manifold of $\boldsymbol{z}$. The two points $\boldsymbol{p}_0$ exist on a 1D homoclinic intersection curve, which we also denote $\boldsymbol{p}_0$, that is formed by the stable and unstable manifolds of the invariant circle. In Fig. 5.17, the stable piece $W^S_{\boldsymbol{z}}[\boldsymbol{z}, \boldsymbol{p}_0]$ is an annulus extending from the invariant circle $\boldsymbol{z}$ to the homoclinic curve $\boldsymbol{p}_0$. The magenta curve at the lower right is twisted by 90° with respect to the red curve at the upper left. Note that this twist is topologically trivial and could be removed by untwisting the magenta curve in the counterclockwise direction. The unstable segment $W^U_{\boldsymbol{z}}[\boldsymbol{z}, \boldsymbol{p}_0]$ is twisted in the same way. The two pieces $W^U_{\boldsymbol{z}}[\boldsymbol{z}, \boldsymbol{p}_0]$ and $W^S_{\boldsymbol{z}}[\boldsymbol{z}, \boldsymbol{p}_0]$ intersect at $\boldsymbol{z}$ and $\boldsymbol{p}_0$ and form a topological torus, enclosing a finite volume. Here, $\boldsymbol{p}_0$ has transition number 1 (index number 0) and forms a primary intersection curve. The enclosed volume is a well defined resonance zone. Thus, all boundary curves will lie entirely in $W^S_{\boldsymbol{z}}[\boldsymbol{z}, \boldsymbol{p}_0]$.

In Fig. 5.17, $W^U_{\boldsymbol{z}}[\boldsymbol{p}_{-1}, \boldsymbol{p}_0]$ is a fundamental annulus. Its first iterate produces two bridges, $W^U_{\boldsymbol{z}}[\boldsymbol{p}_0, \boldsymbol{q}_0]$, an exterior bundt cake, and $W^U_{\boldsymbol{z}}[\boldsymbol{q}_0, \boldsymbol{p}_1]$, an interior bundt cake. Iterating $W^U_{\boldsymbol{z}}[\boldsymbol{q}_0, \boldsymbol{p}_1]$ forward produces two new interior bundt cakes, $W^U_{\boldsymbol{z}}[\boldsymbol{q}_1, \boldsymbol{r}_0]$ and $W^U_{\boldsymbol{z}}[\boldsymbol{s}_0, \boldsymbol{p}_2]$, as well as one new exterior bundt cake $W^U_{\boldsymbol{z}}[\boldsymbol{r}_0, \boldsymbol{s}_0]$. This trellis could be untwisted by rotating the lower right portion counterclockwise 90° and put in a geometric shape that is rotationally invariant about the x-axis. This symmetry implies that the topological dynamics could be reduced to a planar map with 1D invariant manifolds.

Figure 5.18 shows the forward and backward ETPs of Fig. 5.17. Since the system is reversible, the forward and backward ETPs have the same pattern of escape domains. From the ETPs we identify $\mathbf{r}_n$ and $\mathbf{s}_n$ as the sole pseudoneighbor pair and place our obstruction ring slightly perturbed from $\boldsymbol{r}_n$ toward $\boldsymbol{s}_n$. In Fig. 5.17 the ring near $\boldsymbol{r}_0$ (purple triangles) prevents the bridge $W^U_{\boldsymbol{z}}[\boldsymbol{r}_0, \boldsymbol{s}_0]$ from being pulled through the stable manifold while its backward iterate prevents the bridge $W^U_{\boldsymbol{z}}[\boldsymbol{q}_0, \boldsymbol{p}_1]$ from being pulled through the stable manifold.

Since we have a well defined resonance zone, the primary division is constructed

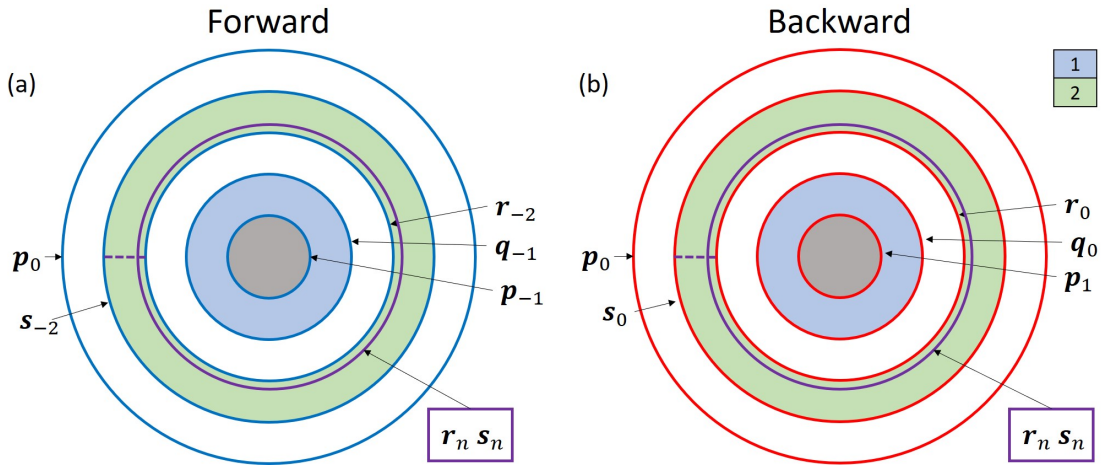

Figure 5.18: Escape time plots for Example 3. (a) The forward escape time plot. (b) The backward escape time plot. $\boldsymbol{r}_n$ and $\boldsymbol{s}_n$ are pseudoneighbor pairs with a obstruction ring (purple) placed between them slightly perturbed from $\boldsymbol{r}_n$ toward $\boldsymbol{s}_n$.

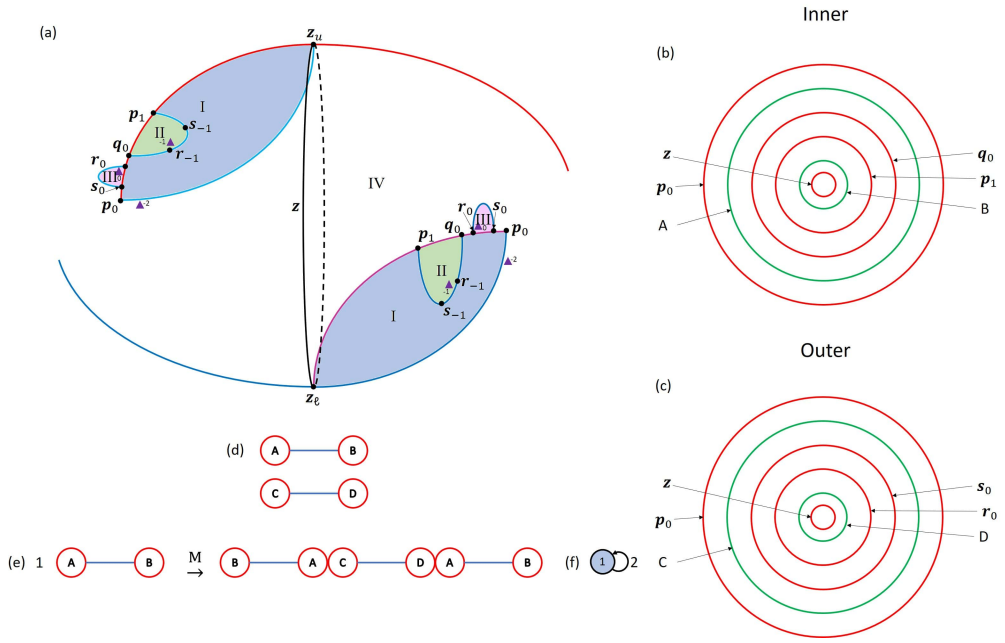

Figure 5.19: (a) The primary division for Example 3. (b) The inner stable division (c) The outer stable division. (d) The two bridge classes. (e) The forward iterate of the one active bridge class. (f) The transition graph of the active bridge class.

as in Sec. 5.2. Figure 5.19a shows the primary division from which we construct the inner and outer stable divisions seen in Fig. 5.19b and Fig. 5.19c. The green circles are the boundary classes used to specify the bridge classes in Fig. 5.19d. The bridges in Fig. 5.19a are broken into two bridge classes, $[\![A, B]\!]$ representing the interior bundt cakes and $[\![C, D]\!]$ representing the exterior bundt cake. $[\![A, B]\!]$ is the only active bridge class and when iterated forward produces two copies of itself and one copy of $[\![C, D]\!]$ concatenated together as seen in Fig. 5.19e. The fact that there is no branching in the graph representing the iterate of $[\![A, B]\!]$ is a consequence of the fact that this system reduces topologically to a 2D map. Compare Fig. 5.19e to Fig. 5.11a and Fig. 5.16d. Figure 5.19f shows the transition graph, with a single active bridge class, which yields a topological entropy $h_{top} = \ln(2)$.

In this example, the stable and unstable manifolds of the invariant circle are 2D extensions of the standard 1D manifolds of the complete horseshoe in 2D. This is a consequence of the rotational symmetry mentioned above. If we factor out this rotational symmetry we are left with the standard horseshoe in 2D. Another way to see this is that the curves in the upper left of Fig. 5.17 form a 2D horseshoe when viewed as 1D invariant manifolds of a 2D map.

5.5 Example 4: Example 2 Revisited

We analyzed Example 2 using the 2D stable and unstable manifolds of the fixed points. In Example 3 we showed that we can get a well defined resonance zone if we use the 2D stable and unstable manifolds of the invariant circle. In Fig. 5.20 we construct an example with a well defined resonance zone based on the manifolds attached to the invariant circle, like Example 3, but incorporating the topological forcing from Example 2. To construct this example, we first suppose that the stable and unstable manifolds of the invariant circle intersect at the primary homoclinic intersection curve $\boldsymbol{p}_0$, as seen in Fig. 5.20a. As in Example 3 the 2D stable manifold of the upper fixed point intersects the 1D unstable manifold of the upper fixed point at the leftmost point labeled $\boldsymbol{p}_0$. In the lower right the 2D unstable manifold of the lower fixed point intersects the 1D stable manifold of the lower fixed point at the

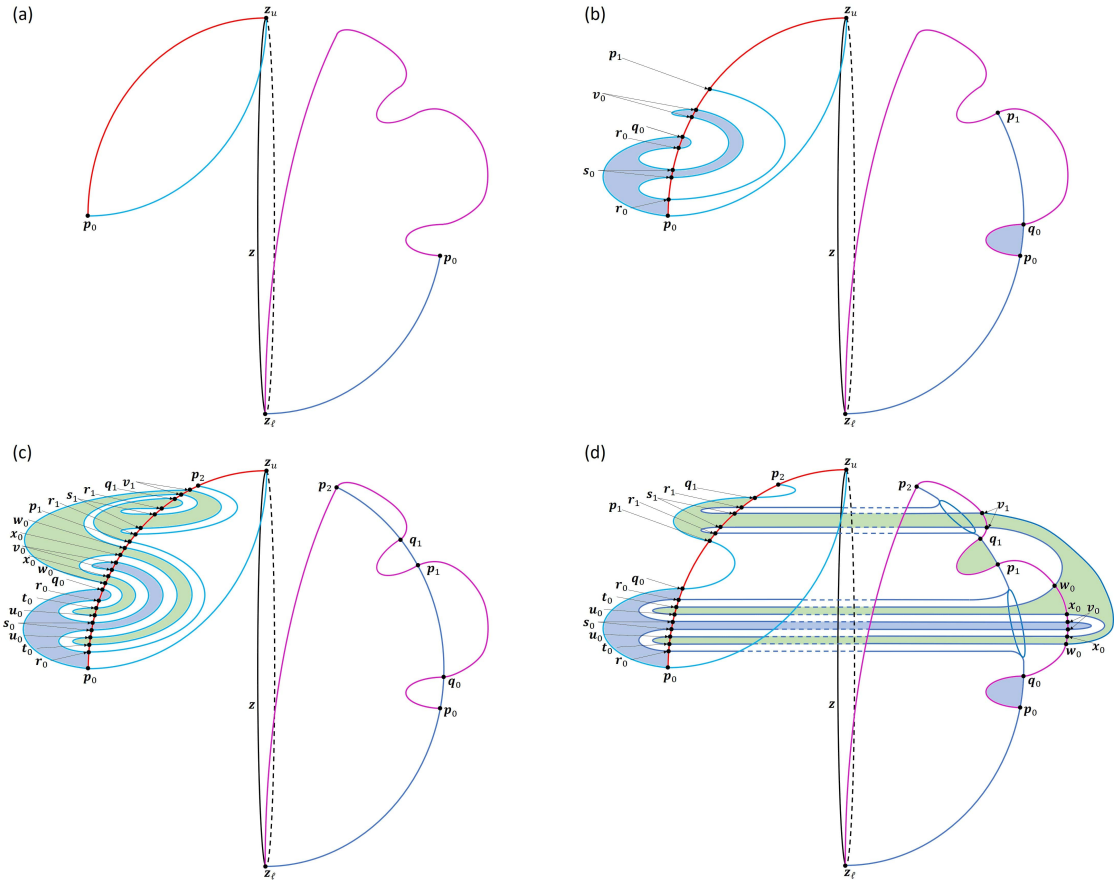

Figure 5.20: (a) The stable and unstable manifolds of the invariant circle up to the primary intersection curve $\boldsymbol{p}_0$. (b) The first iterate of the unstable fundamental annulus $W^U_{\boldsymbol{z}}[\boldsymbol{p}_{-1}, \boldsymbol{p}_0]$. (c) The second iterate of the unstable fundamental annulus. (d) A trellis topologically identical to (c) but geometrically distorted to be similar to Example 2.

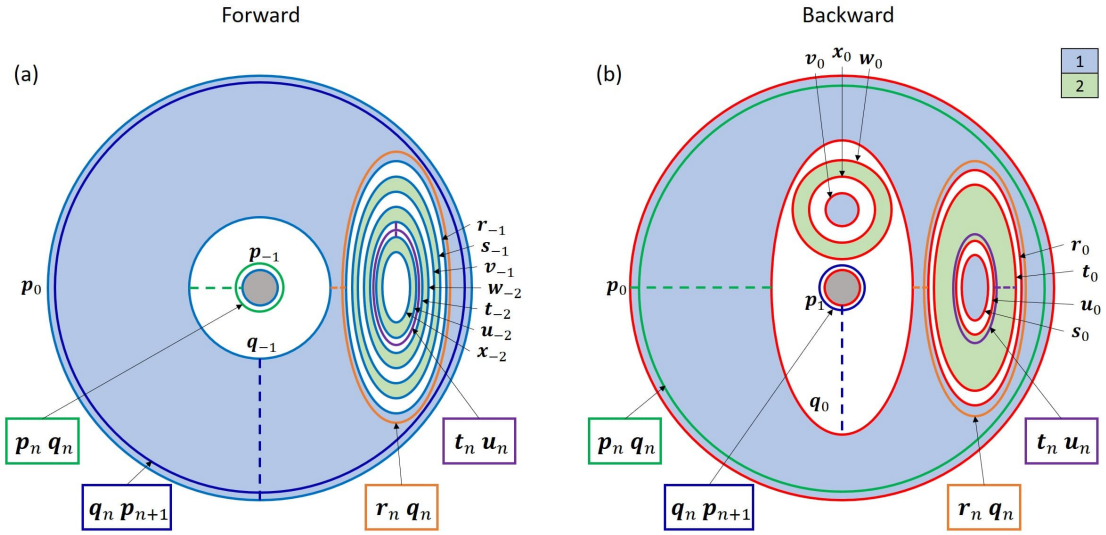

Figure 5.21: The (a) forward and (b) backward capture-time plots (CTPs). Shaded domains represent regions of the fundamental annulus that re-enter the resonance zone after 1 (blue) or 2 (green) iterates. CTPs are used to identify pseudoneighbor pairs in the same way ETPs are used.

rightmost point labeled $\boldsymbol{p}_0$. The resulting 2D manifolds form a toroidal resonance zone like Example 3.

In the simplest case, the bridge $W_{\boldsymbol{z}}^U[\boldsymbol{z}, \boldsymbol{p}_0]$ iterates forward to form an exterior bridge $W_{\boldsymbol{z}}^U[\boldsymbol{p}_0, \boldsymbol{q}_0]$ and interior bridge $W_{\boldsymbol{z}}^U[\boldsymbol{q}_0, \boldsymbol{p}_1]$.

Figure 5.20b modifies this simple dynamics to match Example 2. We take the bundt cake $W_{\boldsymbol{z}}^U[\boldsymbol{q}_0, \boldsymbol{p}_1]$ and push a small piece of it over to intersect $W_{\boldsymbol{z}}^S[\boldsymbol{p}_0, \boldsymbol{q}_0]$ as shown on the left of Fig. 5.20b. This turns the bundt cake $W_{\boldsymbol{z}}^U[\boldsymbol{q}_0, \boldsymbol{p}_1]$ into the tridge $W_{\boldsymbol{z}}^U[\boldsymbol{q}_0, \boldsymbol{r}_0, \boldsymbol{p}_1]$ in Fig. 5.20b. The remaining piece of $W_{\boldsymbol{z}}^U$ attached to $\boldsymbol{r}_0$ is pulled back through the stable submanifold forming the exterior bundt cake $W_{\boldsymbol{z}}^U[\boldsymbol{r}_0, \boldsymbol{s}_0]$. We next pull the manifold back through the stable manifold $W_{\boldsymbol{z}}^S[\boldsymbol{q}_0, \boldsymbol{p}_1]$, forming the macaroni $W_{\boldsymbol{z}}^U[\boldsymbol{s}_0, \boldsymbol{v}_0]$, and terminating in an exterior cap $W_{\boldsymbol{z}}^U[\boldsymbol{v}_0]$. The intersections $\boldsymbol{r}_0$ and $\boldsymbol{s}_0$ in Example 4 are topologically equivalent to the same intersections in Example 2. Here we have an additional intersection $\boldsymbol{v}_0$ which cuts the cap $W_{\boldsymbol{z}}^U[\boldsymbol{s}_0]$ in Example 2 into the concatenation of the macaroni $W_{\boldsymbol{z}}^U[\boldsymbol{s}_0, \boldsymbol{v}_0]$ and the cap $W_{\boldsymbol{z}}^U[\boldsymbol{v}_0]$.

Figure 5.20c shows the forward iterate of $W_{\boldsymbol{z}}^U[\boldsymbol{s}_0, \boldsymbol{v}_0]$ and $W_{\boldsymbol{z}}^U[\boldsymbol{v}_0]$. $W_{\boldsymbol{z}}^U[\boldsymbol{s}_0, \boldsymbol{v}_0]$

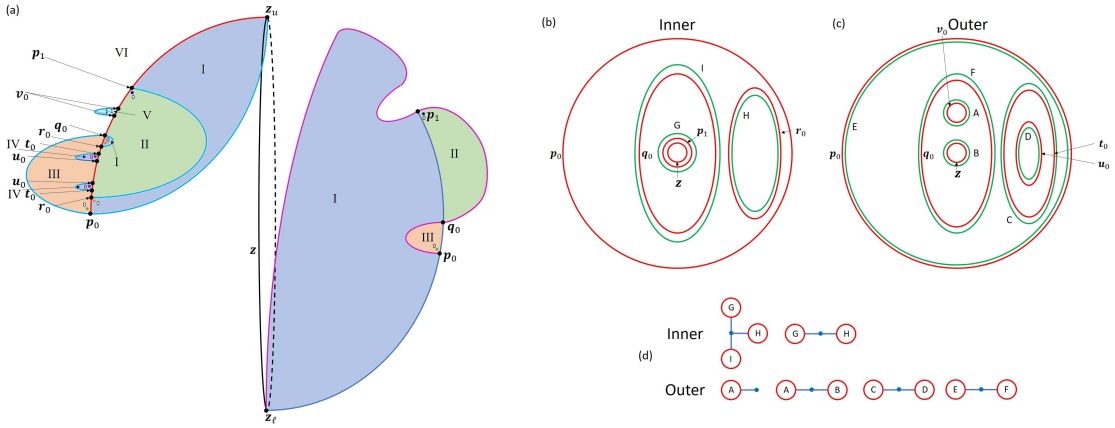

Figure 5.22: (a) The primary division (b) Inner and (c) outer stable primary division. (d) The inner and outer bridge classes for Example 4.

maps inertly forward to $W^U_{\boldsymbol{z}}[\boldsymbol{s}_1, \boldsymbol{v}_1]$. The forward iterate of the cap $W^U_{\boldsymbol{z}}[\boldsymbol{v}_0]$ creates a new intersection $\boldsymbol{x}_0$. This requires the forward iterate to be a concatenation of the exterior macaroni $W^U_{\boldsymbol{z}}[\boldsymbol{v}_1, \boldsymbol{w}_0]$, the interior macaroni $W^U_{\boldsymbol{z}}[\boldsymbol{w}_0, \boldsymbol{t}_0]$, the exterior bundt cake $W^U_{\boldsymbol{z}}[\boldsymbol{t}_0, \boldsymbol{u}_0]$, a second interior macaroni $W^U_{\boldsymbol{z}}[\boldsymbol{u}_0, \boldsymbol{x}_0]$, and the exterior cap $W^U_{\boldsymbol{z}}[\boldsymbol{x}_0]$. In total four new intersections are created: $\boldsymbol{w}_0$, $\boldsymbol{t}_0$, $\boldsymbol{u}_0$, and $\boldsymbol{x}_0$. In Example 2, $\boldsymbol{t}_0$ and $\boldsymbol{u}_0$ are formed by the forward iterate of $W^U_{\boldsymbol{z}}[\boldsymbol{s}_0]$ (Fig. 5.12d) and they have the same topological relationship as exhibited in Fig. 5.20c. The curves $\boldsymbol{w}_0$ and $\boldsymbol{x}_0$ do not occur in Example 2.

Figure 5.20d modifies the geometry of the trellis in Fig. 5.20c but keeps the topology the same. To accomplish this we start by "sliding" the intersection curves $\boldsymbol{v}_0$, $\boldsymbol{x}_0$, and $\boldsymbol{w}_0$ along $W^S_{\boldsymbol{z}}[\boldsymbol{q}_0, \boldsymbol{p}_1]$ from the left-hand side of Fig. 5.20c to the right-hand side of Fig. 5.20d. Similarly, we do the same for $\boldsymbol{v}_1$ on $W^S_{\boldsymbol{z}}[\boldsymbol{q}_1, \boldsymbol{p}_2]$. We adjust the geometry of the tridge $W^U_{\boldsymbol{z}}[\boldsymbol{q}_0, \boldsymbol{r}_0, \boldsymbol{p}_1]$ so that it has a tube connecting the unstable manifold on the right-hand side to the curve $\boldsymbol{r}_0$ on the left-hand side as in Fig. 5.20d. We have drawn Fig. 5.20d so that this tube passes behind the "hole" of the torus that forms the resonance zone.

The dynamics in Fig. 5.20c and Fig. 5.20d are topologically identical, but Fig. 5.20d now geometrically resembles Fig. 5.12d in Example 2. All of the intersection curves between the stable and unstable manifolds in Fig. 5.12d of Example 2 are present in Fig. 5.20d. However, Fig. 5.20d contains extra intersection curves

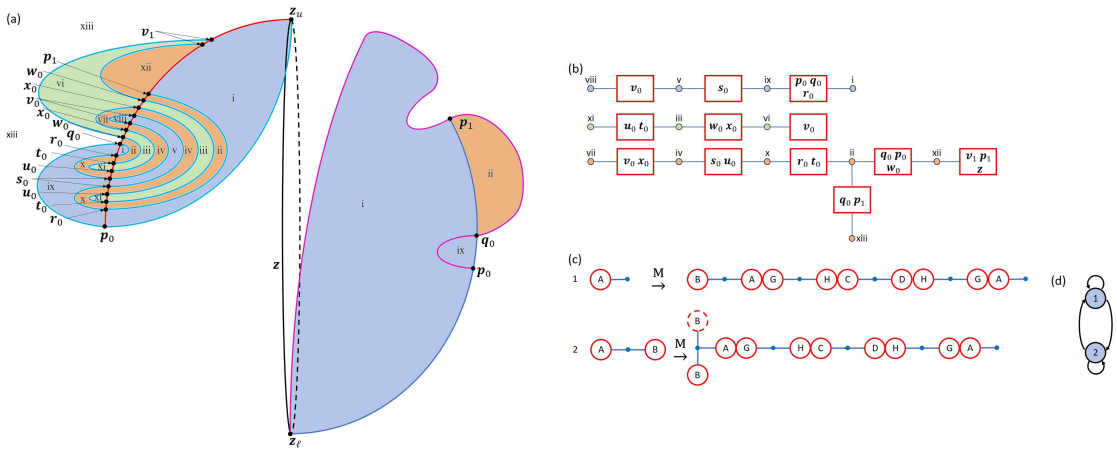

Figure 5.23: (a) The secondary division. (b) The connection graph that shows regions connected across the fundamental stable annulus in (a) (c) The forward iterate of the two active bridge classes. (d) The transition graph for the active bridge classes of Example 4. The transition graph is identical to the transition graph of Example 2. Additionally the iterates of the two bridge classes can be reduced to the iterates in Example 2.

visible on the right-hand side. All of these intersections curves include points on the 1D stable manifold. Hence these curves would always be incomplete in an analysis based solely on the 2D manifolds of the fixed points $\boldsymbol{z}_u$ and $\boldsymbol{z}_\ell$, as was done in Example 2.

Note that part of the iterate of the exterior bridge $W^U_{\boldsymbol{z}}[\boldsymbol{v}_0]$ is inside the resonance zone. This is a case of the recapture of a piece of the unstable manifold that has already escaped. Such recapture is absent from Examples 1 and 3. Additionally, none of the interior bridges of the trellis escape except for the primary bridge $W^U_{\boldsymbol{z}}[\boldsymbol{z}, \boldsymbol{p}_0]$. In order to represent the structure of the homoclinic intersections, we use capture-time plots (CTP) instead of escape time plots. See Fig. 5.21. From Fig. 5.21 we identify four pseudoneighbor pairs, $[\boldsymbol{p}_n, \boldsymbol{q}_n]$, $[\boldsymbol{q}_n, \boldsymbol{r}_n]$, $[\boldsymbol{t}_n, \boldsymbol{u}_n]$, and $[\boldsymbol{q}_n, \boldsymbol{p}_{n+1}]$. We place the appropriate obstruction rings in the CTPs: one perturbed from $\boldsymbol{q}_n$ toward $\boldsymbol{p}_n$ (green), one perturbed from $\boldsymbol{u}_n$ toward $\boldsymbol{t}_n$ (purple), one perturbed from $\boldsymbol{r}_n$ toward $\boldsymbol{q}_n$ (orange), and finally one perturbed from $\boldsymbol{p}_{n+1}$ toward $\boldsymbol{q}_n$ (dark blue).

Using the information of Fig. 5.21, we construct the primary division in Fig 5.22a. The primary division has two interior bridges $W_{\boldsymbol{z}}^U[\boldsymbol{z}, \boldsymbol{p}_0]$ and $W_{\boldsymbol{z}}^U[\boldsymbol{q}_0, \boldsymbol{r}_0, \boldsymbol{p}_1]$ and three exterior bridges, $W_{\boldsymbol{z}}^U[\boldsymbol{p}_0, \boldsymbol{q}_0]$, $W_{\boldsymbol{z}}^U[\boldsymbol{t}_0, \boldsymbol{u}_0]$ and $W_{\boldsymbol{z}}^U[\boldsymbol{v}_0]$. The interior bridge $W_{\boldsymbol{z}}^U[\boldsymbol{q}_0, \boldsymbol{r}_0, \boldsymbol{p}_1]$ and the first two exterior bridges are inert bridges included by Rule 3 in Sec. 5.2; the primary bridge $W_{\boldsymbol{z}}^U[\boldsymbol{z}, \boldsymbol{p}_0]$ and $W_{\boldsymbol{z}}^U[\boldsymbol{r}_0]$ are included by Rule 2. Using Fig. 5.22a we construct the inner and outer stable divisions of $W_{\boldsymbol{z}}^S[\boldsymbol{z}, \boldsymbol{p}_0]$ in Fig. 5.22b and Fig. 5.22c. The inner stable division contains the boundaries for the tridge $W_{\boldsymbol{z}}^U[\boldsymbol{q}_0, \boldsymbol{r}_0, \boldsymbol{p}_1]$ and the primary bridge $W_{\boldsymbol{z}}^U[\boldsymbol{z}, \boldsymbol{p}_0]$. By inspection of the initial trellis all inner boundary classes are of types G and H shown in Fig. 5.22b. The outer stable division is constructed similarly. The outer bridges have boundary classes A-F as shown in Fig. 5.22c. Examination of Fig. 5.20c allows us to identify the bridge classes in Fig 5.22d. We have two interior bridge classes, the macaroni $[\![G, H]\!]$, of which $W_{\boldsymbol{z}}^U[\boldsymbol{w}_0, \boldsymbol{t}_0]$ is a member, and the tridge $[\![G, G, H]\!]$, of which $W_{\boldsymbol{z}}^U[\boldsymbol{q}_0, \boldsymbol{r}_0, \boldsymbol{p}_1]$ is a member. Both of these bridge classes are inert. On the exterior we have inert bridge classes $[\![C, D]\!]$, of which $W_{\boldsymbol{z}}^U[\boldsymbol{t}_0, \boldsymbol{u}_0]$ is a member, and $[\![F, G]\!]$, of which $W_{\boldsymbol{z}}^U[\boldsymbol{p}_0, \boldsymbol{q}_0]$ is a member. Finally, we have the active bridge classes $[\![A]\!]$, including the cap $W_{\boldsymbol{z}}^U[\boldsymbol{v}_0]$, and $[\![A, B]\!]$, including the macaroni $W_{\boldsymbol{z}}^U[\boldsymbol{v}_1, \boldsymbol{w}_0]$.

In Fig. 5.23a we construct the secondary division following the method outlined in Sec. 5.2. From the secondary division, we construct the connection graph in Fig. 5.23b. Together these are used to derive the dynamics of the active bridge classes in Fig. 5.23c as done in Example 1. The active bridge class $[\![A]\!]$ produces one copy of itself and the other active class $[\![A, B]\!]$. Similarly the active bridge class $[\![A, B]\!]$ produces one copy of the active classes $[\![A]\!]$ and $[\![A, B, B]\!]$. Just like in Example 2 we identify $[\![A, B, B]\!]$ with $[\![A, B]\!]$. Fig. 5.23d shows the transition graph for the active bridge classes. The transition graph is identical to the transition graph in Example 2 where each active bridge class produces a copy of itself and the other active bridge class.

Comparing the dynamics between Examples 2 and 4, we see only one point difference, the addition of the inert macaroni $[\![G, H]\!]$ in the bridge dynamics of Fig. 5.23c relative to Fig. 5.16. This macaroni is the result of the stable manifold cutting across the cap $W_{\boldsymbol{z}}^U[\boldsymbol{s}_0]$ and the macaroni $W_{\boldsymbol{z}}^U[\boldsymbol{s}_1, \boldsymbol{t}_0]$ in Example 2. In

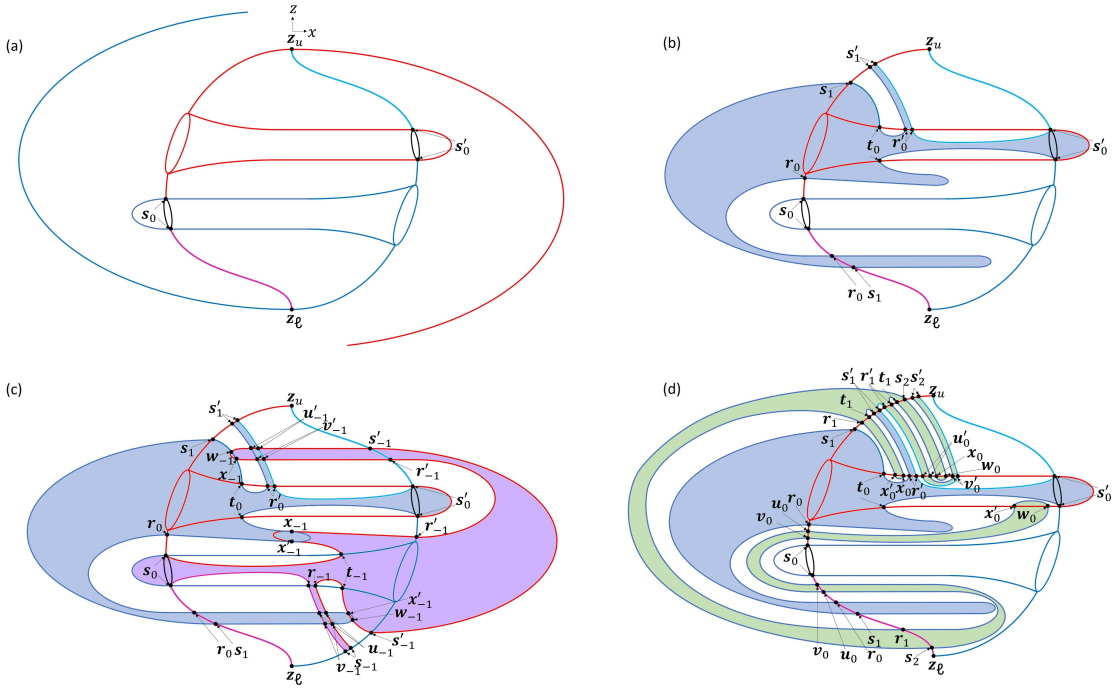

Figure 5.24: (a) The stable and unstable manifolds of the invariant circle up to the intersection curves $\boldsymbol{s}_0$ and $\boldsymbol{s}_0^{'}$. (b) The first forward iterate of the unstable fundamental annulus $W_{\boldsymbol{z}}^{U}(\boldsymbol{s}_{-1}, \boldsymbol{s}_0]$. (c) The first forward iterate of the unstable fundamental annulus and the first backward iterate of the stable fundamental annulus $W_{\boldsymbol{z}}^{S}[\boldsymbol{p}_0^{'}, \boldsymbol{p}_1^{'})$. (d) The trellis in (c) iterated forward once.

Example 4 this means that the equivalent to $W_{\boldsymbol{z}}^{U}[\boldsymbol{s}_0]$ in Example 2 is $W_{\boldsymbol{z}}^{U}[\boldsymbol{s}_0, \boldsymbol{v}_0]$ concatenated with $W_{\boldsymbol{z}}^{U}[\boldsymbol{v}_0]$. In essence this means the bridge class $[\![A]\!]$ in Example 2 is the concatenation of bridge classes $[\![A]\!]$ and $[\![G, H]\!]$ in Example 4. Additionally $[\![A, B]\!]$ in Example 2 is the concatenation of $[\![A, B]\!]$, $[\![G, H]\!]$, and $[\![A]\!]$ in Example 4. If we make those substitutions in the bridge dynamics of Example 4, we get bridge dynamics identical to Example 2.

5.6 Example 5: A Fully 3D Non-Equatorial Intersection

Here we analyze the culminating trellis. It lacks an equatorial intersection (like Examples 2-4), its dynamics are fully 3D (like Examples 1, 2 and 4), and the primary bridge class is recurrent (like Examples 1 and 3). Also like Example 3, the system is reversible with $S(x, y, z) = (-x, y, -z)$. Figure 5.24a shows the stable manifold of the invariant circle up to the homoclinic curve $\boldsymbol{s}_0$ and the unstable manifold up to $\boldsymbol{s}'_0$. The unstable manifold reaches across to intersect the stable manifold at $\boldsymbol{s}_0$. By symmetry the stable manifold reaches across to intersect the unstable manifold at $\boldsymbol{s}'_0$. The union of $W^S_{\boldsymbol{z}}[\boldsymbol{z}, \boldsymbol{s}_0, \boldsymbol{s}'_0]$ and $W^U_{\boldsymbol{z}}[\boldsymbol{z}, \boldsymbol{s}_0, \boldsymbol{s}'_0]$ is a topological genus-2 torus which bounds a well defined resonance zone. Note that neither $\boldsymbol{s}_0$ nor $\boldsymbol{s}'_0$ is a primary intersection curve, according to Sec. 5.1.2. As a pair, however, $\boldsymbol{s}_0$ and $\boldsymbol{s}'_0$ play an analogous role to a single primary intersection curve, since $W^U_{\boldsymbol{z}}[\boldsymbol{z}, \boldsymbol{s}_0, \boldsymbol{s}'_0]$ and $W^S_{\boldsymbol{z}}[\boldsymbol{z}, \boldsymbol{s}_0, \boldsymbol{s}'_0]$ only intersect at their boundaries.

We use the intersection curve $\boldsymbol{s}'_0$, which is a proper loop on $W^U_{\boldsymbol{z}}$, to define the unstable fundamental annulus $W^U_{\boldsymbol{z}}(\boldsymbol{s}'_{-1}, \boldsymbol{s}'_0]$. We similarly use $\boldsymbol{s}_0$ to define the stable fundamental annulus $W^S_{\boldsymbol{z}}[\boldsymbol{s}_0, \boldsymbol{s}_1)$. We specify that the first iterate of the unstable fundamental annulus produces Fig. 5.24b. This iterate produces an exterior tridge $W^U_{\boldsymbol{z}}[\boldsymbol{s}'_0, \boldsymbol{r}_0, \boldsymbol{t}_0]$, an interior tridge $W^U_{\boldsymbol{z}}[\boldsymbol{t}_0, \boldsymbol{r}_0, \boldsymbol{s}_1]$, an interior macaroni $W^U_{\boldsymbol{z}}[\boldsymbol{s}'_1, \boldsymbol{r}'_0]$ and two exterior caps $W^U_{\boldsymbol{z}}[\boldsymbol{s}_1]$ and $W^U_{\boldsymbol{z}}[\boldsymbol{r}_0]$. Figure 5.24c shows the first backward iterate of the stable fundamental annulus $W^S_{\boldsymbol{z}}[\boldsymbol{s}_0, \boldsymbol{s}_1)$. This backward iterate is obtained by time-reversal symmetry. Notice that the $\boldsymbol{r}_0$ and $\boldsymbol{r}'_{-1}$ curves are related by the symmetry operator S and therefore $\boldsymbol{r}_n$ and $\boldsymbol{r}'_n$ are time-reversal-symmetry partners. The curves $\boldsymbol{t}_0$ and $\boldsymbol{t}_{-1}$ are also related by the symmetry operator S so that the orbit $\boldsymbol{t}_n$ is its own time-reversal partner. The primed orbits are always the time-reversal partners of unprimed orbits.

Figure 5.24d is obtained by iterating the trellis in Fig. 5.24c forward once. The stable component of the trellis is the same as in Fig 5.24b. The unstable component of the trellis contains the second iterate of the unstable fundamental annulus $W^U_{\boldsymbol{z}}(\boldsymbol{s}_{-1}, \boldsymbol{s}_0]$.

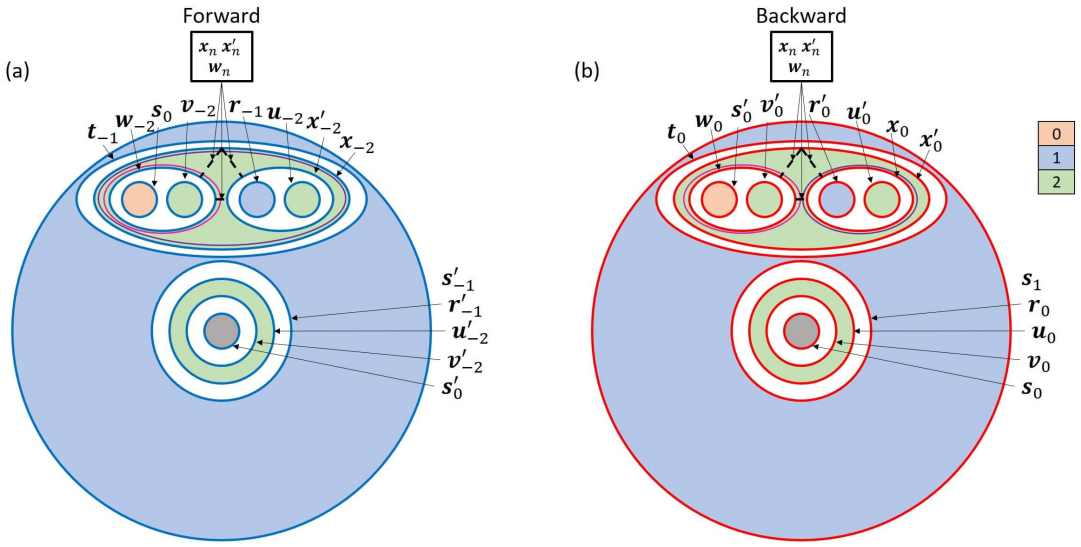

Figure 5.25: The (a) forward and (b) backward ETP for Example 5. The topologies of the ETPs are identical due to time-reversal symmetry. We consider the domains surrounded by $\boldsymbol{s}_0$ and $\boldsymbol{s}_0^{'}$ to be outside the resonance zone and thus to "escape" at the zeroth iterate. Every pair formed from the three curves $\boldsymbol{x}_n$, $\boldsymbol{x}'_n$ and $\boldsymbol{w}_n$ is a pseudoneighbor pair. Together they form a "pseudoneighbor triplet". The triplet can be broken up by two obstruction rings, one perturbed from $\boldsymbol{x}_n$ toward $\boldsymbol{x}_n^{'}$ and $\boldsymbol{w}_n$ (purple), and one perturbed from $\boldsymbol{w}_n$ toward $\boldsymbol{x}_n^{'}$ and $\boldsymbol{x}_n$ (orange).

Figure 5.25 contains the forward and backward ETPs. We see the time-reversal symmetry of the forward and backward ETPs because one can be converted to the other by swapping primed and unprimed intersection curves, noting that $\boldsymbol{t}_n$ and $\boldsymbol{w}_n$ are their own symmetry partners. The escape domains bound by $\boldsymbol{s}_0$ in the forward ETP and $\boldsymbol{s}'_0$ in the backward ETP escape the resonance zone on the zeroth iterate. This is a result of the caps $W^U_{\boldsymbol{z}}[\boldsymbol{s}_0]$ and $W^S_{\boldsymbol{z}}[\boldsymbol{s}'_0]$ existing outside the resonance zone in Fig. 5.24a. We identify pseudoneighbors by looking for curves whose iterates are adjacent in both the forward and backward ETPs. This example has a pseudoneighbor triplet $[\boldsymbol{w}_n,\ \boldsymbol{x}_n,\ \boldsymbol{x}'_n]$, i.e., $[\boldsymbol{w}_n, \boldsymbol{x}_n]$, $[\boldsymbol{w}_n, \boldsymbol{x}'_n]$ and $[\boldsymbol{x}_n, \boldsymbol{x}'_n]$ are each pseudoneighbor pairs. For a pseudoneighbor triplet we only need two obstruction rings, one around $\boldsymbol{w}_n$ perturbed toward $\boldsymbol{x}_n$ (magenta) and one around $\boldsymbol{x}_n$ perturbed toward $\boldsymbol{x}'_n$ (purple). These two obstruction rings act to uphold the exterior tridge $W^U_{\boldsymbol{z}}[\boldsymbol{w}_0, \boldsymbol{x}_0, \boldsymbol{x}'_0]$. See Fig. 5.26a.

We construct the primary division in Fig. 5.26a using the rules in Sec 5.2. We include the stable portion of the trellis from Rule 1. We include the bridge $W^U_{\boldsymbol{z}}[\boldsymbol{w}_0, \boldsymbol{x}_0, \boldsymbol{x}'_0]$ from Rule 2 and the bridges $W^U_{\boldsymbol{z}}[\boldsymbol{t}_0, \boldsymbol{r}_0, \boldsymbol{s}_1]$ and $W^U_{\boldsymbol{z}}[\boldsymbol{z}, \boldsymbol{s}_0, \boldsymbol{s}'_0]$ from Rule 3. From the primary division we obtain the inner and outer stable divisions in Fig. 5.26b and Fig. 5.26c. The system has two interior bridge classes, the primary tridge $[\![A, B, D]\!]$ and the macaroni $[\![C, E]\!]$ shown in Fig 5.26d. Figure 5.26d contains five bridges classes each of which is represented by bridges present in the trellis in Fig. 5.24d. As we will see below, these are the five bridge classes necessary to specify the active bridge dynamics.

We construct the secondary division in Fig. 5.27a based on the rules outlined in Sec. 5.2. The unstable portion of the secondary division contains the iterate of the primary tridge $W^U_{\boldsymbol{z}}[\boldsymbol{z}, \boldsymbol{s}_0, \boldsymbol{s}'_0]$ and the iterate of $W^U_{\boldsymbol{z}}[\boldsymbol{t}_0, \boldsymbol{r}_0, \boldsymbol{s}_1]$ based on Rule 2. The secondary division contains thirteen regions forming three connected components: blue, green and orange as seen in the connection graph of Fig. 5.27b.

We use the same process as in Example 1 to compute the forward iterates of the interior bridge classes in Fig 5.26d. It is easily seen that the three exterior bridge classes are inert. Figure 5.28 computes the iterate of $[\![A, B, D]\!]$. The iterate of $[\![A, B, D]\!]$ contains two copies of itself and one copy of the active interior macaroni

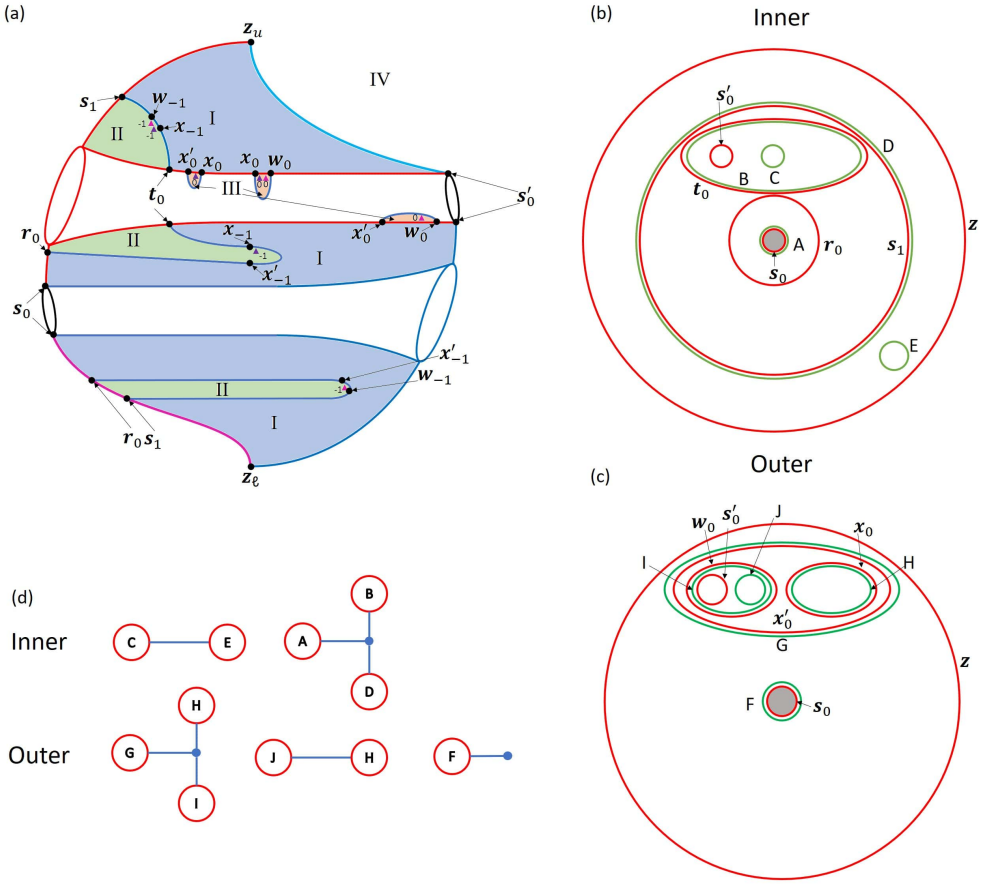

Figure 5.26: (a) The primary division of phase space. (b) The inner and (c) outer stable divisions. (d) The inner and outer bridge classes for Example 5.

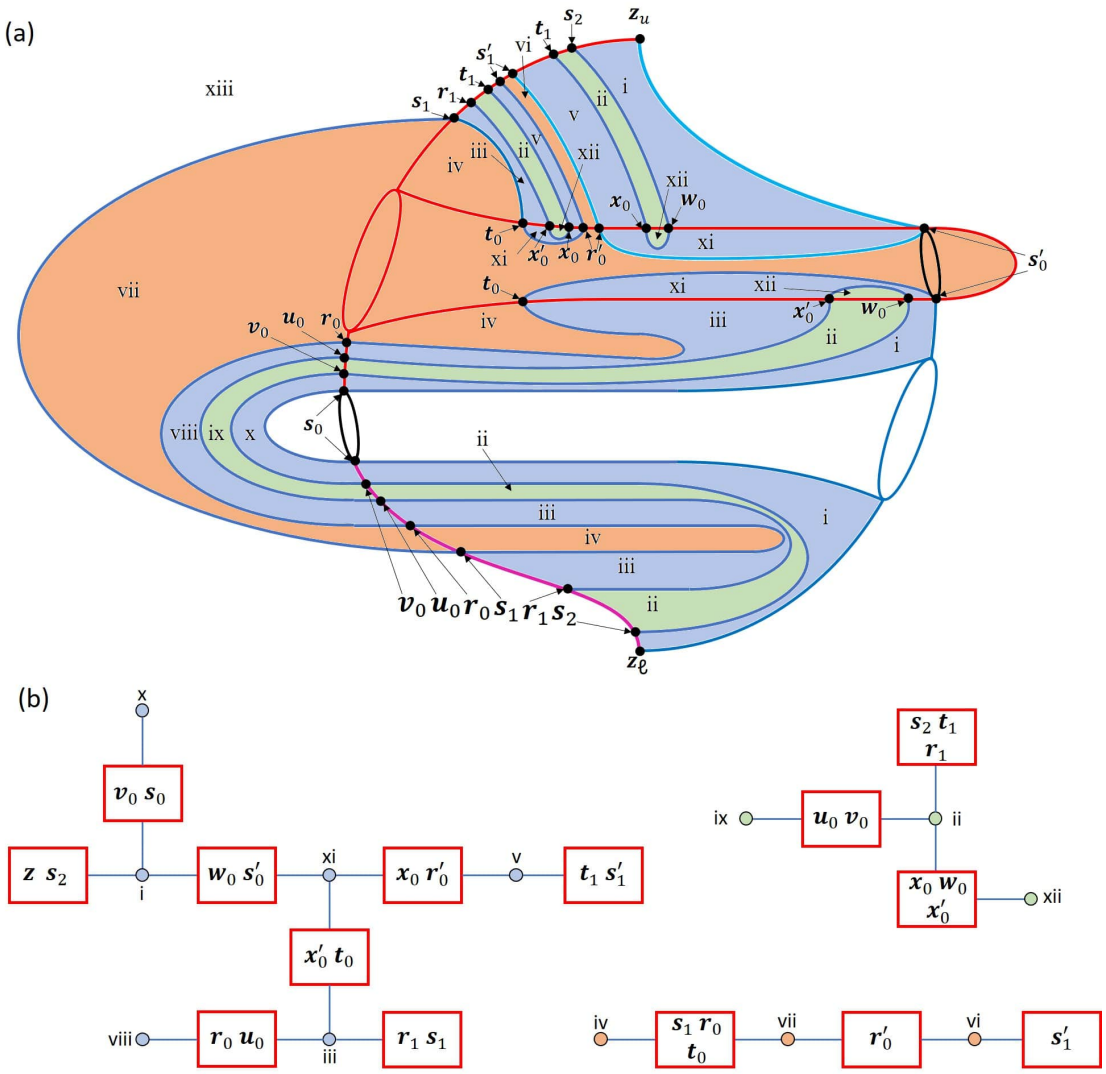

Figure 5.27: (a) The secondary division of phase space for Example 5. (b) The connection graph for the regions of the secondary division.

$[\![C, E]\!]$. Note that the primary bridge $W^U_{\boldsymbol{z}}[\boldsymbol{z}, \boldsymbol{s}_0, \boldsymbol{s}'_0]$ belongs to the bridge class $[\![A, B, D]\!]$ and hence produces copies of itself upon iteration. Figure 5.29 computes the iterate of $[\![C, E]\!]$, which contains three concatenated macaronis: two copies of $[\![C, E]\!]$ itself and one inert exterior macaroni.

Figure 5.30a summarizes the iterates of the two active bridge classes $[\![A, B, D]\!]$ and $[\![C, E]\!]$. Note that the dynamics are fully 3-dimensional because there is branching in the forward iterate of $[\![A, B, D]\!]$ in Fig. 5.30a. This iterate represents 2-dimensional stretching that is not possible in a 2D map. On the other hand the stretching seen in the forward iterate of $[\![C, E]\!]$ is 1-dimensional because it contains no branching and is essentially the same stretching seen in 2D maps. We construct the transition graph in Fig. 5.30b based on iterates of the two active classes. Bridge class 2, i.e. $[\![A, B, D]\!]$, produces two copies of itself and one of bridge class 1, i.e. $[\![C, E]\!]$, whereas bridge class 1 produces only two copies of itself. Thus bridge class 2 produces class 1 but not visa versa. This is an example of the phenomenon seen in Ref. [62] where it was demonstrated that the full transition graph decomposes into two strongly connected components; a strongly connected component is one in which each vertex has a directed path to every other vertex in the component. One strongly connected component corresponds to 2D stretching, and the other strongly connected component corresponds to 1D stretching. The 1D connected component can be reached from the 2D connected component but not visa versa. In the present example, each of these connected components consists of a single vertex. Furthermore both the 1D and 2D connected components produce stretching rates of $\ln 2$. The topological entropy is the maximum of these two; thus $h = \ln 2$. In general, the 2D and 1D stretching rates need not be equal. However, in cases with time-reversal-symmetry, like this example, it has been conjectured that they must be equal [62].

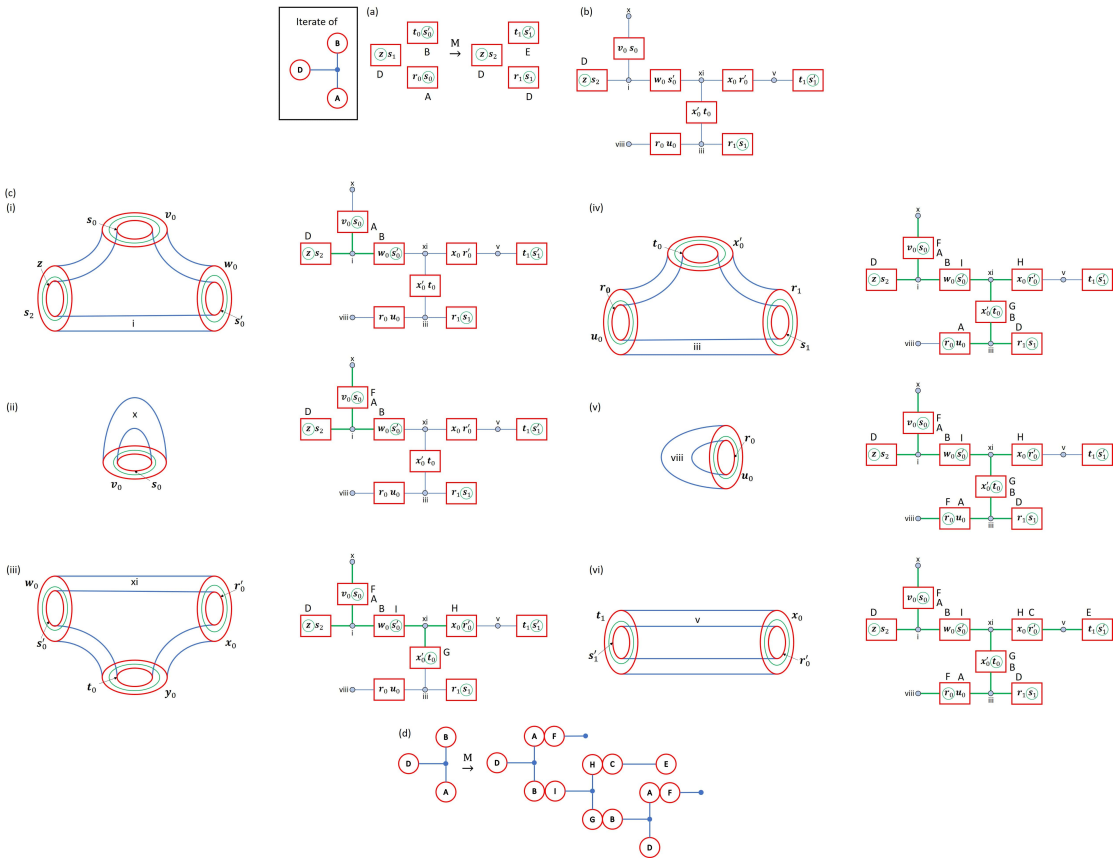

Figure 5.28: A step-by-step illustration of the process to construct the forward iterate of $[\![A, B, D]\!]$. (a) We iterate the boundary classes that make up the bridge class to identify where on the secondary division they occur. (b) The component of the connection graph that the forward iterates of the boundary classes lie within. (c) A step-by-step process of identifying the forward iterate of $[\![A, B, D]\!]$. Each of the regions the forward iterate lies within is shown on the left while the connections being made are shown on the right. Boundary classes are labeled adjacent each box. (d) The concatenation of bridge classes that make up the forward iterate of $[\![A, B, D]\!]$.

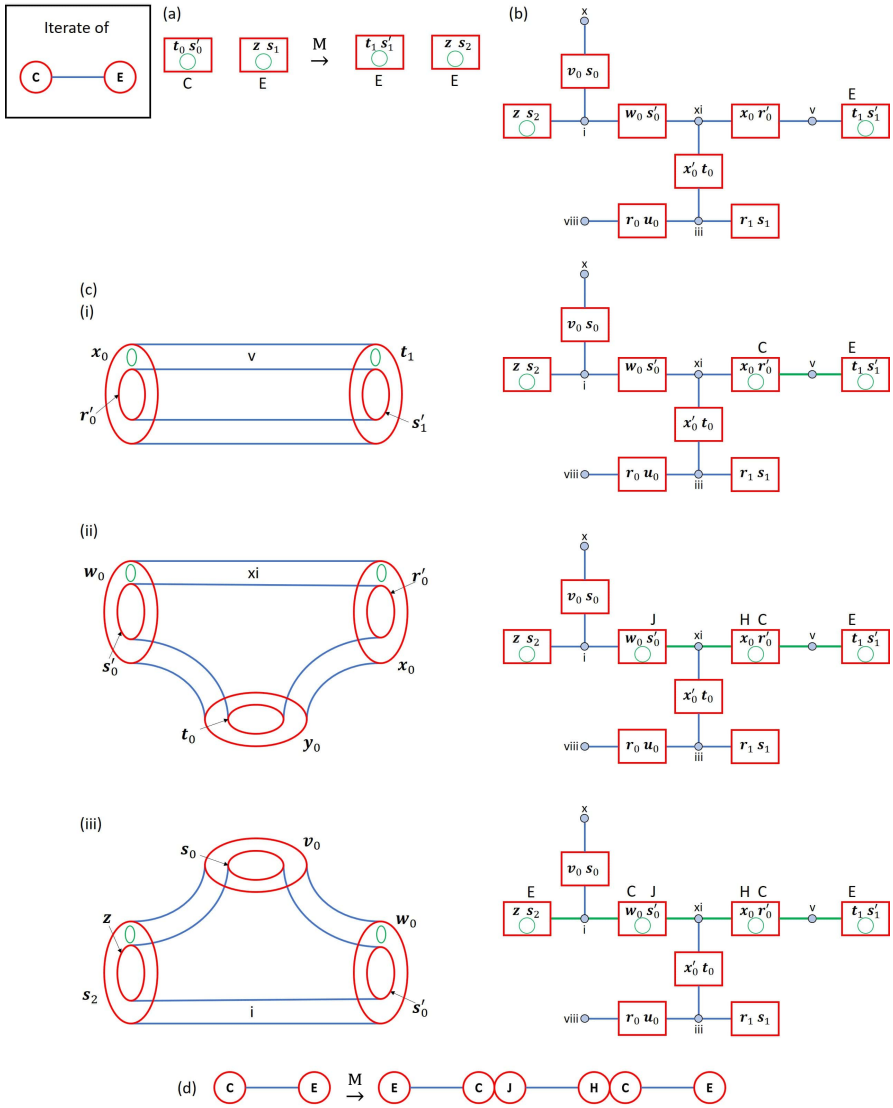

Figure 5.29: A step-by-step illustration of the process to identify the forward iterate of $[\![C, E]\!]$. (a) The boundary classes that make up the bridge class and the locations of their forward iterates. Note that in this case the boundary classes do not surround any homoclinic intersections in either the primary or secondary stable divisions. (b) The component of the connection graph that the forward iterates of the boundary classes lie within. (c) A step-by-step process of constructing the forward iterate of $[\![C, E]\!]$. (d) The concatenation of the bridge classes that make up the forward iterate of $[\![C, E]\!]$.

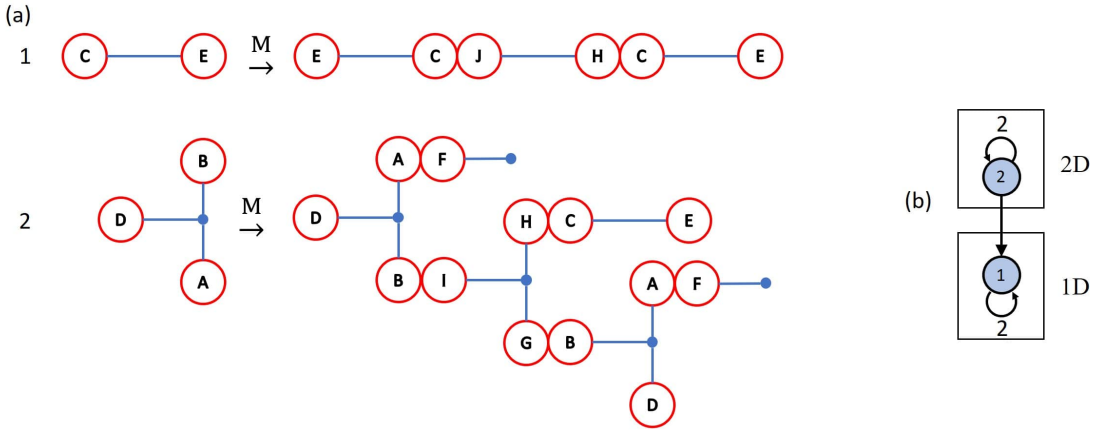

Figure 5.30: (a) The two active bridge classes in Example 5 and the concatenation of bridge classes that make up their iterates. (b) The transition graph of the two active bridge classes. Note that the forward iterate of bridge class 2 produces copies of itself and bridge class 1 while the forward iterate of bridge class 1 produces only copies of itself. This is an example of a case where the transition graph decomposes into two strongly connected components, one representing 2D dynamics and one representing 1D dynamics.

Chapter 6

HLD Applied to the Quadratic Family of Maps

With HLD extended to systems without an equatorial intersection, we turned back to the quadratic family of maps. We used our previous explorations from chapter 4 to quickly work to identify parameters that would produce suitable dynamics.

6.1 Identifying Ideal Parameters

As before, we limited ourselves to reversible maps with the parameters $\bar{a} = \bar{b} = 1$; see sec 4.1. We also opted to examine manifolds that intersected with wedges similar to our toy models in chapter 5. Finally, we hoped to examine a case with "straight" pole-to-pole intersection curves that did not spiral into the fixed points. The spiral nature of pole-to-pole curves is a result of complex eigenvectors and eigenvalues at the fixed points.

To identify parameter values where the eigenvalues are real, we calculated the discriminant (Δ) of the Jacobin of the map at the fixed points. If $\Delta > 0$ then all the eigenvalues are real, if $\Delta < 0$ then two of the eigenvalues are a complex conjugate pair. At the fixed points the Jacobin of the Lomelí map is:

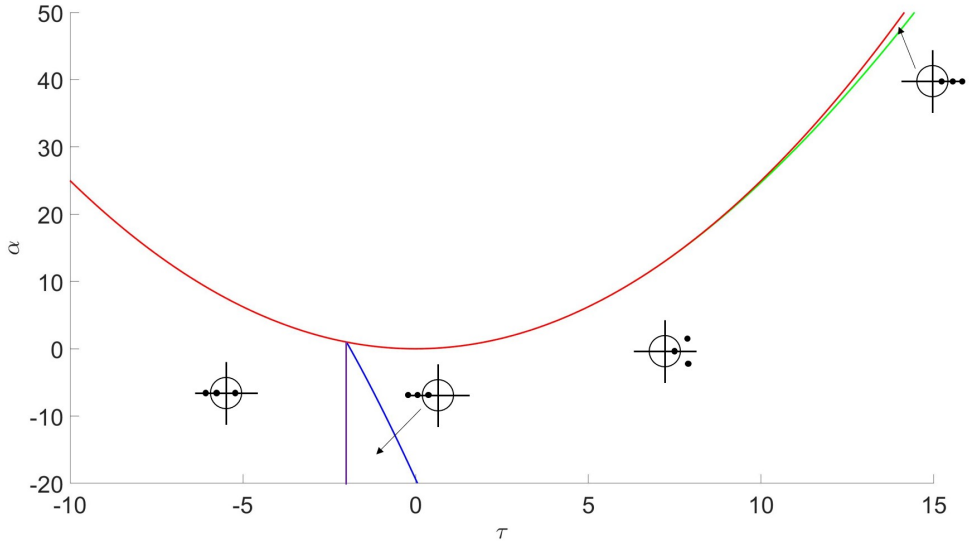

Figure 6.1: Stability of the lower fixed point for the Lomelí form of the quadratic family of maps when $a = c$. The red curve is the saddle-node bifurcation of the fixed points. The green and blue curves are where the discriminant at the fixed points is zero resulting in degenerate eigenvalues.

$$D(f(x_\pm, x_\pm, x_\pm)) = \begin{pmatrix} \tau + (2a+b)x_\pm & (2a+b)x_\pm & 1 \\ 1 & 0 & 0 \\ 0 & 1 & 0 \end{pmatrix} \tag{6.1}$$

where for the Lomelí map $x_\pm = \frac{1}{2}(-\tau \pm \sqrt{\tau^2 - 4\alpha})$. Solving for the discriminant we get:

$$\Delta = \alpha^2 + \alpha(18 + 12\tau) - 4\tau^3 - 27. \tag{6.2}$$

Eq. 6.2 assumes the required symmetry and scaling, that is $a = c$ and $a+b+c = 1$.

We plot $\Delta = 0$ in fig. 6.1 as the green and blue curves. The red curve corresponds to the saddle-node bifurcation of fixed points. The green curve corresponds to where the discriminant is zero and the eigenvalues are degenerate. For the quadratic family of maps we found that the eigenvectors are degenerate when the eigenvalues are degenerate. This prevents the formation of 2D stable and unstable

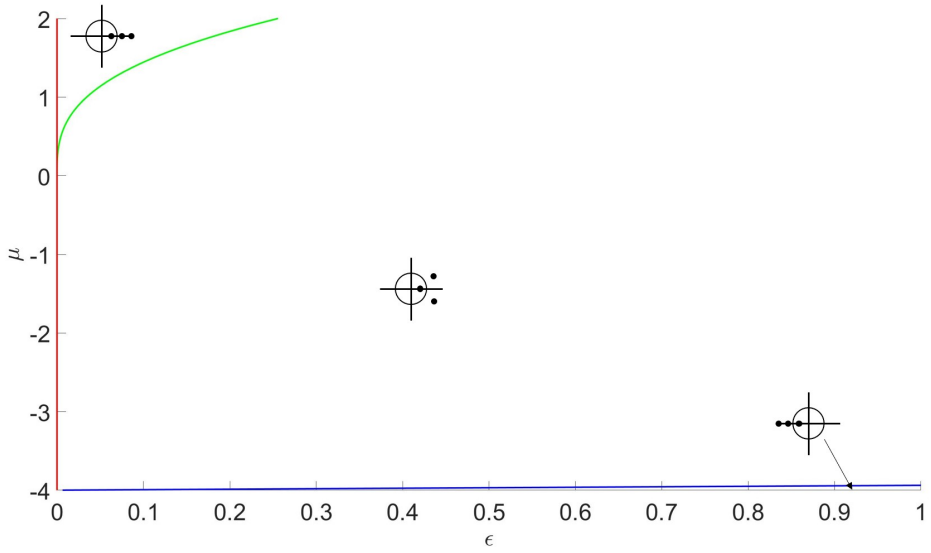

Figure 6.2: Stability of the left fixed point for the Dullin-Meiss form of the quadratic family of maps. The red curve is the saddle-node bifurcation of the fixed points. The green and blue curves are where the discriminant at the fixed points is zero resulting in degenerate eigenvalues.

manifolds at the fixed point. The slim region between the green and red curves is the portion of parameter space where all the eigenvalues are real.

Fig. 6.2 shows the stability for the Dullin Meiss form of the map. Real eigenvalues are found only when $\mu \geq 0$. We attempted to find values for μ and ϵ that would produce manifolds that we could examine but we did not find any suitable candidates. We found that even with real eigenvalues the eigenvectors nearly pointed in the same direction creating long thin manifolds that did not intersect. We opted to constrain ourselves to regions where $-4 \leq \mu \leq 0$ and $0 \leq \epsilon \leq 0.4$.

Eventually we settled on parameters $\bar{a} = \bar{b} = 1$, $\bar{c} = 0.5$, $\epsilon = 0.3$, and $\mu = -1.383$. The manifolds form wedges with pole-to-pole intersection curves that spiral into the fixed points. Additionally no invariant tori form inside the vortex bubble. We used a brute force computation to generate the manifolds in fig. 6.3a. For these parameters we observe four pole-to-pole intersection curves. The 1D stable and unstable manifolds do not intersect the 2D stable and unstable manifolds instead spiraling around the fixed point before being escaping to infinity as seen

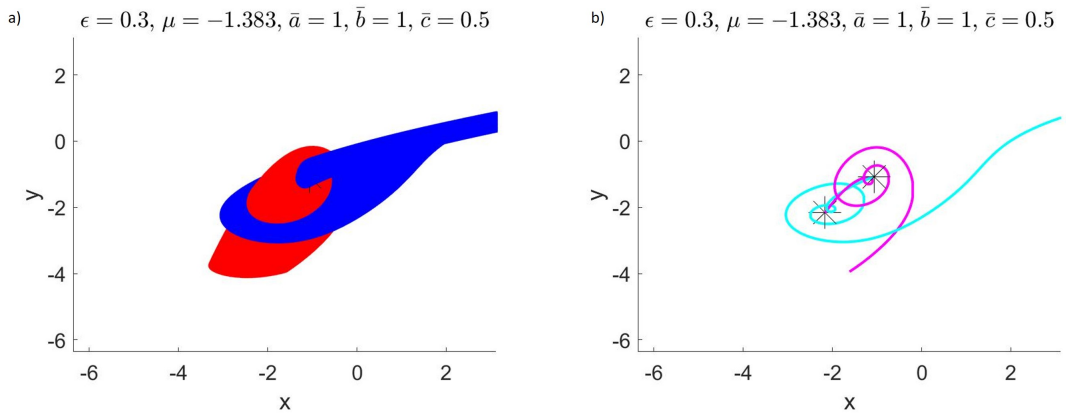

Figure 6.3: Brute force manifold computation of the a) 2D stable (red) and unstable (blue) manifolds. b) is a brute force computation of the 1D stable (magenta) and unstable (cyan) manifolds.

in fig. 6.3b.

Our next step was to compute the pole-to-pole intersection curves and their manifolds. Previous work by Jason Mireles-James numerically computed the pole-to-pole curves with a high degree of accuracy [35]. This method of computing the pole-to-pole intersections required finding an initial intersection point between the 2D stable and unstable manifold and then computing the Taylor expansion of the pole-to-pole curve.

6.2 Computing Intersections with the Symmetry Plane

We began our analysis of the manifolds by looking at their intersection with a slice of phase space. The natural slice to look at is the symmetry plane between the two fixed points. For the Dullin-Meiss form this symmetry plane is the yz-plane. For the Lomelí form the symmetry plane is the plane perpendicular to the vector pointing from one fixed point to the other and centered on the point halfway between the fixed points. We chose parameters for the Dullin-Meiss form, converted them into the Lomelí form using eq 4.12, and then preformed the computations.

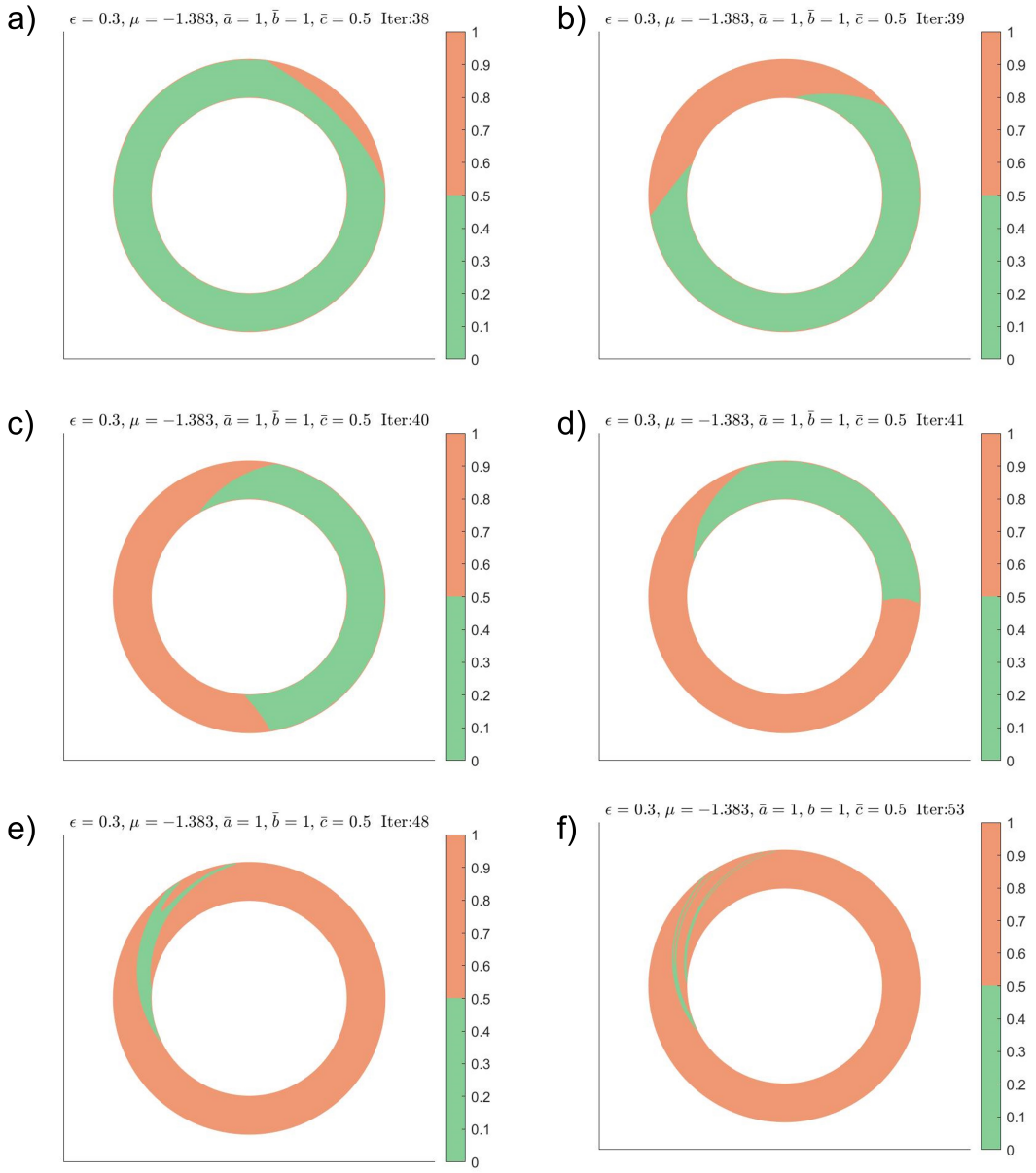

Figure 6.4: Above-below plots (ABPs) for our example map. Green regions are the part of the initial annulus below the symmetry plane after n iterates while orange regions are above the symmetry plane. Points on the boundary between red and blue regions are on the symmetry plane. ABPs for iterates a) 38 b) 39 c) 40 d) 41 e) 48 and f) 53 are shown.

To understand the intersection of the manifolds with the symmetry plane we constructed *above-below plots* (ABPs). A given ABP shows which points on an annular disk are above or below the symmetry plane at a given iterate. ABPs are constructed similar to ETPs except each point is marked as either above or below the symmetry plane at an iterate. As with ETPs delaunay triangulation is used to plot the points and identify regions where points are above (or below) the symmetry plane. Points on the boundary between regions that are above the plane and regions below the plane exist on the symmetry plane. The boundary curves are the intersections of the manifold with the symmetry plane.

To compute the ABPs, we begin at an initial annulus near enough to the fixed point such that the manifold can be linearly approximated. We chose the inner ring of the annulus to have radius of 10^{-5} and the outer radius to be $|\max(\lambda_i)| * r_{inner}$. The annulus was uniformly seeded with an initial set of points (the vertices of a triangular mesh making up the annulus). The points were iterated until they had reached a user defined number of iterates or they were above a plane parallel to the symmetry plane far from the upper fixed point. Each point was marked at each iterate to be either below the symmetry plane (marked as 0) or above the symmetry plane (marked with a 1).

Fig. 6.4 shows ABPs after n iterations of the annular disk. Green regions are the part of the initial annulus below the symmetry plane after n iterates while orange regions are the portions above. Fig. 6.4a - fig. 6.4d show the ABPs of iterates 38-41. As the initial annulus is iterated forward more of it crosses from below to above the symmetry plane. By iterate 41 all of the initial annulus has passed through the symmetry plane once and some has passed back below. In fig. 6.4e and fig. 6.4f a majority of the initial manifold is above the plane as it is drawn off to infinity.

Looking closely at fig. 6.5 we see some fractal structure forming. The green bands split into two narrow green bands. The four bands toward the edge of the annulus will split at higher iterates into eight bands which in turn will also split at higher iterates. We expected to see this fractal structure appear in the ABP.

We need to accurately compute the boundaries between regions in the ABPs in

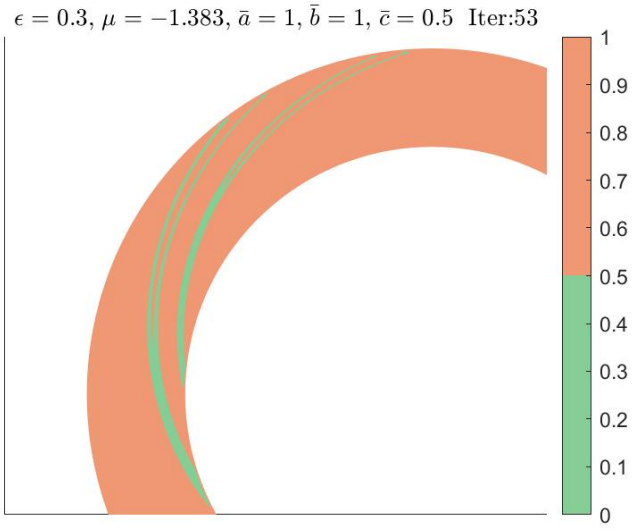

Figure 6.5: The ABP at iterate 53. We see the beginnings of the fractal structure as the two green bands split into two narrower green bands. This process will continue to occur at higher and higher iterates.

order to accurately compute the intersection of the manifold with the symmetry plane. To do so we must refine any triangles that have at least one vertex above and one vertex below the symmetry plane. We call these triangles *boundary triangles*. In ABPs boundary triangles are refined using methods outlined in sec. 2.3 with minor differences. Instead doing a topological or angular refinement we instead only do a length refinement. We identify bad *crossing edges*. Crossing edges are edges of a boundary triangle whose endpoints are on opposite sides of the symmetry plane. A crossing edge is identified as a *bad edge* if its length in phase space is greater than a user defined tolerance (we used 10^{-3}). For each unique bad edge we add a new point at the midpoint of the edge on the annulus near the fixed point. We retriangulate the annulus and iterate all the newly added points forward. We then repeat the processes of checking for bad edges and adding new points until all crossing edges have length less than our tolerance. Each cycle of the refinement should roughly halve the length of the bad edge in phase space. The algorithm is,

1. Identify edges whose length in phase space is greater than the tolerance.

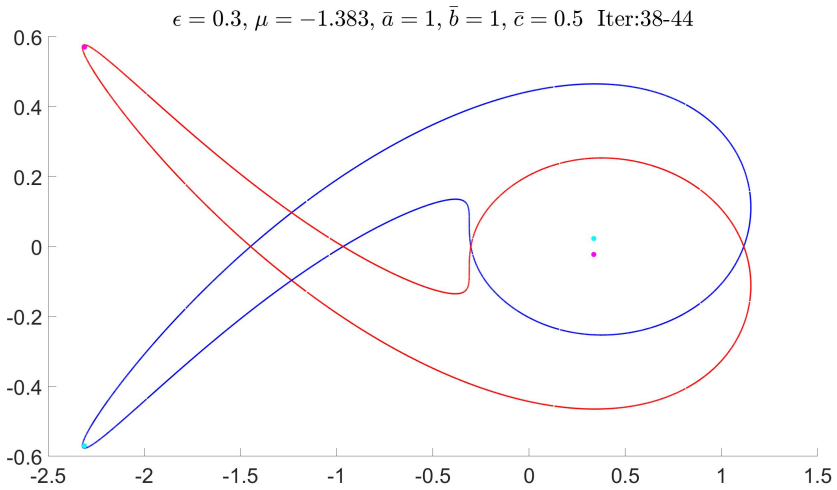

Figure 6.6: Intersection between the stable (red) and unstable (blue) manifolds and the symmetry plane. The intersections of the 1D unstable manifold (cyan dots) and 1D stable manifold (magenta dots) with the symmetry plane are also plotted.

2. Add new points at the midpoint of the edges on the initial annulus.

3. Retriangulate the annulus.

4. Iterate the new points forward.

5. Repeat steps 1-4 until no bad edges remain.

which results in a well resolved ABP for a specific iterate. The boundary triangles of the ABP are a triangular mesh in phase space that cross the symmetry plane. We repeat the algorithm for the range of iterates we want to analyze.

The final step is to take these highly refined boundary triangles and compute their intersections with symmetry plane. The intersections between the boundary triangles in phase space and the symmetry plane are an accurate approximation of the intersection between the manifold and the symmetry plane.

Fig. 6.6 shows the results of the algorithm applied to our parameter set for 44 iterates of the initial annulus. The intersection of the 2D unstable manifold with the symmetry plane is shown in blue while the intersection of the 2D stable

manifold with the symmetry plane is shown in red. Additionally the intersections of the 1D unstable and stable manifolds are marked with a cyan and magenta dots respectively. Because our map is reversible the stable manifold is a reflection of the unstable manifold over the x-axis. The 1D unstable manifold comes down from the upper fixed point to intersect with the symmetry plane near the center of the manifolds in fig. 6.6, then comes back up intersecting a second time in the bottom left of fig. 6.6 before going off to infinity. Due to our map being reversible the 1D stable manifold is symmetric to the 1D unstable manifold.

In the lower left quadrant of fig. 6.6 there is a wedge of the unstable manifold that will go off to infinity. We surmise that anything in this wedge actually gets drawn off to infinity with the wedge. The 1D unstable manifold follows this wedge out to infinity as well. In fact the 1D unstable manifold does not seem to intersect the 2D stable manifold at any point.

6.3 Identifying the Pole-to-Pole Intersection Curves

There are six intersections between the 2D stable and unstable manifolds in fig. 6.6. Using fig. 6.3, we identified four pole-to-pole intersection curves. There are three possible causes of the two additional intersections between the stable and unstable manifolds in the symmetry plane: 1) two intersections could be a closed intersection curve that crosses the symmetry plane, 2) they could be two additional pole-to-pole intersection curves we didn't see in fig. **??**, or 3) they could be the result of one of the pole-to-pole intersection curves that intersects the symmetry plane more than once. All pole-to-pole curves connect the fixed point below the symmetry plane to the fixed point above the symmetry plane so the pole-to-pole intersection curve can only transversely intersect the symmetry plane an odd number of times.

To understand the the pole-to-pole intersections, we compute a *z-stack*. A z-stack is a sequence of images where each image is a slice of 3-dimensional space. Put together, the stack shows the changing cross-section of a 3-dimensional object. In our case, we constructed our z-stacks by computing the intersection of the

manifolds with plane perpendicular to the line connecting the fixed points. The intersections were computed for planes starting slightly below the lower fixed point and extended to slightly above the upper fixed point. To compute the intersections of the manifolds with the plane we used the algorithm described in sec. 6.2, changing the symmetry plane to the plane of the z-stack. The z-stack can be compiled into a movie where each frame is a slice of phase space starting from the lower fixed point to the upper.

Fig. 6.7a - fig. 6.7f shows six images from the z-stack. Fig. 6.7a shows the manifolds at their first intersection in the z-stack. They intersect at a tangency that goes through a saddle node bifurcation into the two intersections in fig. 6.7b labeled $\boldsymbol{a}$ and $\boldsymbol{a'}$. We know the intersections are on the same pole-to-pole curve because the tangency indicates that a pole-to-pole curve has "turned around" in the direction of the z-stack. In fig. 6.7c two new intersections appear between the unstable manifold and the free ends of the stable manifold. These free ends appear to spiral into the 1D stable manifold near the center shown by the magenta star. We label them $\boldsymbol{b}$ and $\boldsymbol{c}$ since we're not sure if they're on the same pole-to-pole curve. Between fig. 6.7c and fig. 6.7d a new saddle node bifurcation occurs giving us the intersections $\boldsymbol{d}$ and $\boldsymbol{d'}$. Additionally the intersection we labeled $\boldsymbol{c}$ goes through a saddle-node bifurcation with the intersection $\boldsymbol{a'}$ indicating that $\boldsymbol{a}$, $\boldsymbol{a'}$, and $\boldsymbol{c}$ all lie on the same pole-to-pole curve. If we followed $\boldsymbol{c}$ back down the z-stack we'd pass through fig. 6.7c and eventually spiral into the 1D unstable manifold shown with the cyan dot. In fig. 6.7e we reach the symmetry plane. Two new intersection points appeared on the loose ends of the stable manifold which we've labeled $\boldsymbol{e}$ and $\boldsymbol{f}$. Finally in fig. 6.7f $\boldsymbol{b}$ and $\boldsymbol{d'}$ go through saddle-node bifurcation indicating that they are also on the same pole-to-pole curve. Since $\boldsymbol{d}$ and $\boldsymbol{d'}$ came from a saddle-node bifurcation of a single pole-to-pole curve we know that $\boldsymbol{b}$, $\boldsymbol{d}$ and $\boldsymbol{d'}$ all lie on the same curve. Finally there are two new intersections $\boldsymbol{g}$ and $\boldsymbol{h}$. These intersections will be related to one of the previous ones we've seen since we're above the symmetry plane and the map is reversible. We now know $\boldsymbol{a}$, $\boldsymbol{e}$ and $\boldsymbol{f}$ in fig. 6.7e are each on their own pole-to-pole curves while the remaining three points are on the fourth pole-to-pole curve.

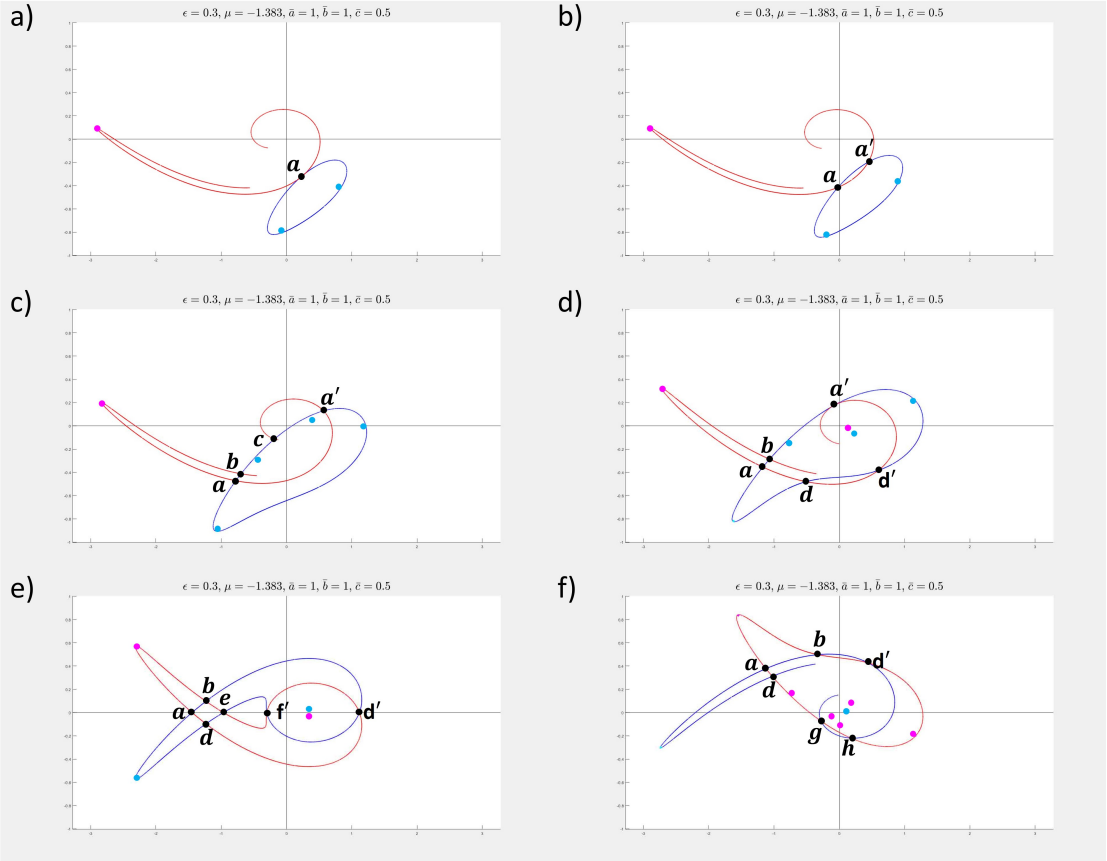

Figure 6.7: Frames from a z-stack movie used to track the pole-to-pole intersection curves and identify which intersection points in the symmetry plane are on the same pole-to-pole curve. a) shows the saddle-node bifurcation that occurs when a pole-to-pole intersection curve reverses direction. b) shows how the bifurcation becomes two points on the same pole-to-pole curve labeled as $\boldsymbol{a}$ and $\boldsymbol{a'}$. c) shows two new intersections that appear on the lose ends of the stable manifold. In d) $\boldsymbol{c}$ and $\boldsymbol{a'}$ go through a saddle node bifurcation which indicates that they are on the same pole-to-pole curve. e) is the intersection with the symmetry plane. f) shows $\boldsymbol{b}$ and $\boldsymbol{d'}$ about to go through a saddle-node bifurcation indicating that they are on the same pole-to-pole curve as $\boldsymbol{d}$.

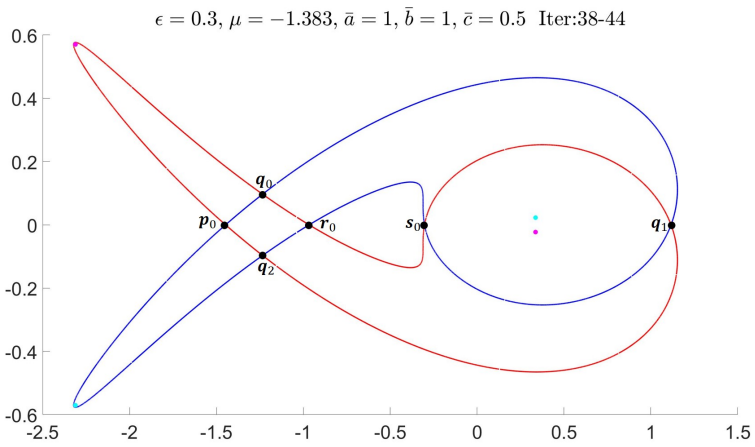

Figure 6.8: Intersection of the 1D unstable (cyan), 1D stable (magenta), 2D unstable (blue) and 2D stable (red) manifolds with the symmetry plane. Each of the intersections between the stable and unstable manifolds are labeled based on the pole-to-pole curve that passes through the point. The curve $\boldsymbol{q}$ first passes through the symmetry plane at $\boldsymbol{q}_0$ before intersecting again at $\boldsymbol{q}_1$ and $\boldsymbol{q}_2$.

The pole-to-pole intersection curves in fig. 6.8 have been relabeled to reflect our new knowledge. We label the intersection such that each letter corresponds to a unique intersection curve. The subscript indicates the order in which the pole-to-pole intersection curve intersects the symmetry plane when starting from the lower fixed point and following the curve to the upper fixed point. $\boldsymbol{p}_0$ is a pole-to-pole intersection curve that goes from the lower fixed point to the upper fixed point intersecting the symmetry plane only one time. $\boldsymbol{q}$ is a pole-to-pole intersection curve that intersects the symmetry plane three times, first by passing from below to above at $\boldsymbol{q}_0$, then going from above to below at $\boldsymbol{q}_1$, and finally by intersecting the symmetry plane a third time at $\boldsymbol{q}_2$. It then spirals into the upper fixed point without intersecting the symmetry plane again. The number of times $\boldsymbol{r}$ and $\boldsymbol{s}$ intersect the symmetry plane is still unknown, as they appeared when the open ends of the stable manifold intersected the unstable manifold in the z-stack. To understand these pole-to-pole intersection curves, we need to compute the symmetry plane intersection and z-stack for higher iterates of the initial annulus.

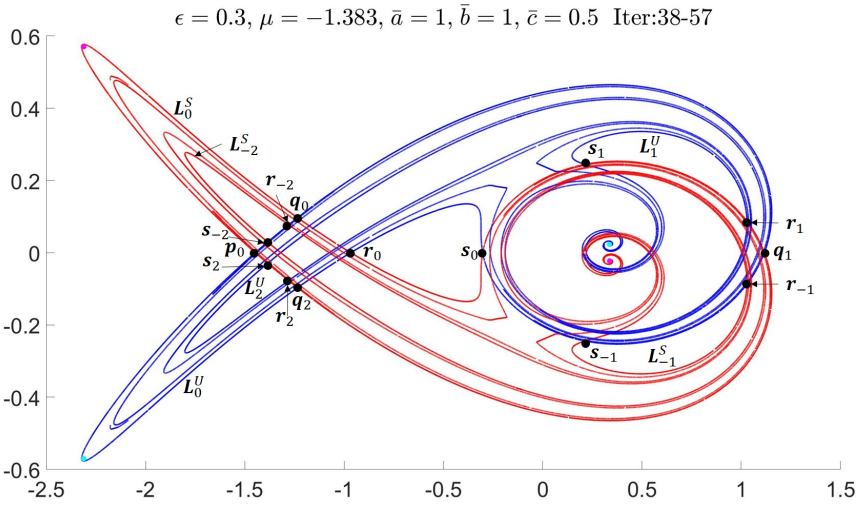

Figure 6.9: Intersection between the stable (red) and unstable (blue) manifolds and the symmetry plane after 57 iterates of the initial annulus. The four pole-to-pole intersection curves that occur at the intersection of the stable and unstable caps are labeled.

The intersections between manifolds and the symmetry plane after 57 iterations of the initial annulus is shown in fig. 6.9. We used a z-stack of the manifold generated by 55 iterates of the initial annulus to track the pole-to-pole intersection curves associated with $\boldsymbol{r}_0$ and $\boldsymbol{s}_0$. We found that $\boldsymbol{r}$ and $\boldsymbol{s}$ intersect the symmetry plane a five times each. There are additional, unlabeled, intersection curves that appear in fig. 6.9. These intersections lie on new pole-to-pole curves. It appears as though new pole-to-pole intersection curves are being forced by earlier pole-to-pole intersection curves.

6.4 Extending 2D HLD to pole-to-pole curves

We note that intersections of the stable and unstable manifolds with the symmetry plane in fig. 6.9 look very much like 1D manifolds in 2D space. There are some important subtleties to take into account. To understand them we need to understand how the pole-to-pole curves are lie in phase space.

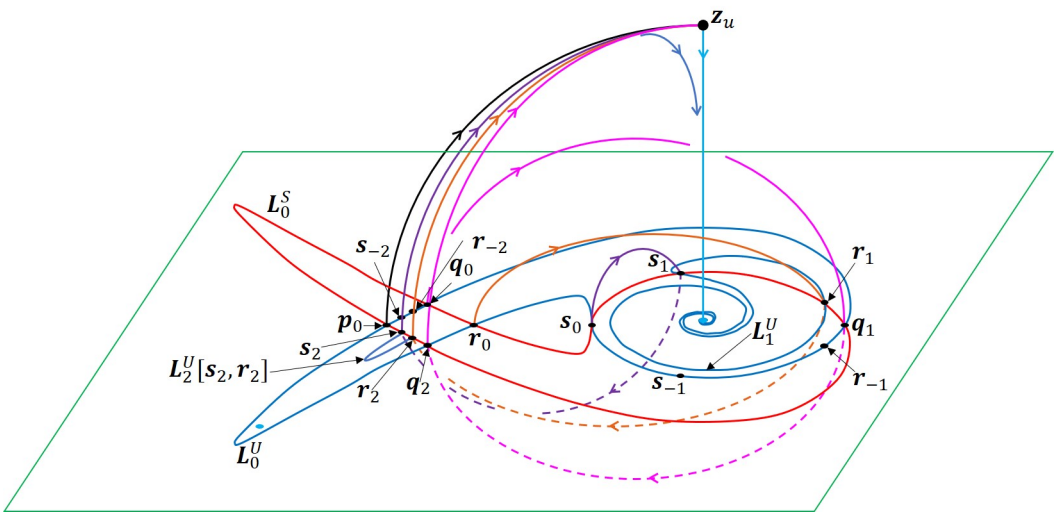

Figure 6.10: A cartoon image showing how the pole-to-pole curves connect from the symmetry plane (green box) to the upper fixed point $\boldsymbol{z}_u$. Four pole-to-pole intersection curves $\boldsymbol{p}$ (black), $\boldsymbol{s}$ (purple), $\boldsymbol{r}$ (orange), and $\boldsymbol{q}$ (pink) are shown with arrows indicating the direction of their trajectories. The intersection of the symmetry plane with the 2D unstable manifold (blue) and 2D stable manifold (red) is shown. The full 2D manifolds are omitted for clarity. The 1D unstable manifold (cyan) intersects the plane at the center of the spiral $\boldsymbol{L}_1^U$.

Fig. 6.10 shows how the pole-to-pole intersection curves lie in phase space as they extend from the symmetry plane to the upper fixed point $\boldsymbol{z}_u$. The intersection curve $\boldsymbol{p}$ (black) has only one intersection with the symmetry plane. It extends from the lower fixed point $\boldsymbol{z}_\ell$ (not shown), through the symmetry plane up to the upper fixed point $\boldsymbol{z}_u$. The portion of the curve $\boldsymbol{p}$ shown in fig. 6.10 lies entirely on the *stable cap*. The stable cap (and unstable cap) is the portion of the 2D manifold that exists from the fixed point up to its first intersection with the symmetry plane. The unstable cap intersects the symmetry plane as the closed curve $\boldsymbol{L}_0^U$ while the stable cap intersects the plane as the closed curve $\boldsymbol{L}_0^S$. Some portion of all pole-to-pole intersection curves lie on the unstable cap and another portion on the stable cap. We conclude that all pole-to-pole intersections must at some point intersect $\boldsymbol{L}_0^S$ and $\boldsymbol{L}_0^U$ however the intersection of a pole-to-pole curve with $\boldsymbol{L}_0^S$ need not also be an intersection with $\boldsymbol{L}_0^U$.

The pole-to-pole intersection curve $\boldsymbol{q}$ (pink) intersects the symmetry plane three times. From $\boldsymbol{q}_0$ the curve exists above the plane until it intersects a second time at $\boldsymbol{q}_1$. The curve passes below the plane until turning around and intersecting a third time at $\boldsymbol{q}_2$. From here the curve is on the stable cap all the way to the fixed point $\boldsymbol{z}_u$. The intersection of the 2D unstable manifold with the symmetry plane that connects $\boldsymbol{p}_0$ to $\boldsymbol{q}_2$ clockwise is labeled as $\boldsymbol{L}_0^U[\boldsymbol{q}_2, \boldsymbol{p}_0]$. From this curve in the symmetry plane the 2D unstable manifold extends along the exterior of the stable cap (intersecting at $\boldsymbol{p}$ and $\boldsymbol{q}$) as a lobe drawn to infinity, though the intersection curves themselves extend to $\boldsymbol{z}_u$. The portion of the 2D unstable manifold that is just inside the cap near the two pole-to-pole curves will get drawn up the inside of the stable cap until it is near the fixed point. Here the 2D unstable manifold will be forced back down along the 1D unstable manifold (cyan). This is noted by the blue curve near the fixed point in fig. 6.10. In this example the 2D unstable manifold is forced to spiral around the 1D unstable manifold due to the complex eigenvectors at the fixed point. Eventually this portion of the 2D unstable manifold will intersect the symmetry plane from above. The 2D unstable manifold will continue to follow the 1D unstable manifold eventually being drawn up inside the lobe connecting $\boldsymbol{p}_0$ and $\boldsymbol{q}_2$.

We know from fig. 6.9 that the pole-to-pole curves $\boldsymbol{r}$ (orange) and $\boldsymbol{s}$ (purple) intersect the symmetry plane five times each. To reduce the complexity we consider only three of the intersections as the remaining two are symmetric to what is shown. Starting from $\boldsymbol{r}_0$ on $\boldsymbol{L}_0^U$ $\boldsymbol{r}$ passes above the symmetry plane before intersecting at $\boldsymbol{r}_1$. Unlike the curve $\boldsymbol{q}$, $\boldsymbol{r}$ intersects with the curve $\boldsymbol{L}_1^U$. $\boldsymbol{r}$ continues below the symmetry plane before intersecting at $\boldsymbol{r}_2$. $\boldsymbol{r}_2$ lies on $\boldsymbol{L}_0^S$ between $\boldsymbol{p}_0$ and $\boldsymbol{q}_2$. $\boldsymbol{r}$ continues along the stable cap up to the fixed point. $\boldsymbol{s}$ follows a similar trajectory to $\boldsymbol{r}$. $\boldsymbol{r}$ intersects the plane before $\boldsymbol{r}_0$ at $\boldsymbol{r}_{-1}$ and $\boldsymbol{r}_{-2}$ as shown in fig. 6.10. The same is true for $\boldsymbol{s}$.

Consider the curve $\boldsymbol{L}_0^U[\boldsymbol{r}_0, \boldsymbol{s}_0]$. The endpoints of this curve are a part of the pole-to-pole intersection curves $\boldsymbol{r}$ and $\boldsymbol{s}$. Since the 2D unstable manifold must be attached to curves $\boldsymbol{r}$ and $\boldsymbol{s}$, the simplest possible path for the 2D unstable manifold is to be dragged along the curves. This means the manifold will intersect the symmetry plane as the curve $\boldsymbol{L}_1^U[\boldsymbol{r}_1, \boldsymbol{s}_1]$. Continuing along $\boldsymbol{r}$ and $\boldsymbol{s}$ the manifold will be forced back though the symmetry plane a third time as the curve $\boldsymbol{L}_2^U[\boldsymbol{r}_2, \boldsymbol{s}_2]$. Finally, the lobe is drawn up along the stable cap and out to infinity.

Next, consider the curve $\boldsymbol{L}_0^U[\boldsymbol{p}_0, \boldsymbol{q}_2]$ going clockwise along $\boldsymbol{L}_U^0$. The two endpoints $\boldsymbol{p}_0$ and $\boldsymbol{q}_2$ slide along the stable manifold to the fixed point. $\boldsymbol{L}_0^U[\boldsymbol{r}_0, \boldsymbol{q}_2]$ follows $\boldsymbol{r}$ to the point $\boldsymbol{r}_1$ and $\boldsymbol{q}$ to the fixed point however $\boldsymbol{L}_0^U[\boldsymbol{r}_0, \boldsymbol{q}_2)$ (i.e. the portion of the curve not including $\boldsymbol{q}_2$) will be forced by the 1D manifold back down through the symmetry plane. The manifold intersects the symmetry plane as the curve $\boldsymbol{L}_1^U[\boldsymbol{r}_1]$. Similarly $\boldsymbol{L}_0^U[\boldsymbol{q}_0, \boldsymbol{s}_0]$ follows a similar path intersecting at $\boldsymbol{L}_1^U[\boldsymbol{s}_1]$. Finally, we already know that $\boldsymbol{L}_0^U[\boldsymbol{r}_0, \boldsymbol{s}_0]$ is forced to $\boldsymbol{L}_1^U[\boldsymbol{r}_1, \boldsymbol{s}_1]$. Putting this together we see that the 2D manifold connected to $\boldsymbol{L}_0^U[\boldsymbol{p}_0, \boldsymbol{q}_2]$ is forced to intersect the symmetry plane as the curve $\boldsymbol{L}_1^U$. Since $\boldsymbol{L}_0^U[\boldsymbol{q}_2, \boldsymbol{p}_0]$ (in the counterclockwise direction) is drawn to the fixed point and never intersects the plane again we say that the 2D manifold connected to $\boldsymbol{L}_0^U$ is forced to intersect at $\boldsymbol{L}_1^U$.

We use our new understanding to construct a set of rules for applying HLD to the intersections of the manifolds with the symmetry plane. First, let us define the iterate of a pole-to-pole intersection with the symmetry plane as the next intersection between the pole-to-pole intersection and the symmetry plane (in the

forward direction). That is we "slide" from one intersection of a pole-to-pole curve with the symmetry plane along the pole-to-pole curve to the next intersection. By this definition the forward iterate of $\boldsymbol{q}_0$ is $\boldsymbol{q}_1$, the forward iterate of $\boldsymbol{q}_1$ is $\boldsymbol{q}_2$ and $\boldsymbol{q}_2$ does not have a forward iterate. It should be noted that the point $\boldsymbol{q}_0$ in phase space does **not** map to $\boldsymbol{q}_1$ under the map M. For the remainder of the chapter we will refer to iterating a point or curve as sliding it forward along the manifold to the next point or curve on the symmetry plane. We will use the term map to refer to applying the map M to a point or set of points.

Second, we define the iterate of a curve in the symmetry plane as being pushed along the 2D manifold until intersecting the symmetry plane again. The endpoints of the curve must be pole-to-pole intersection curves. For example, we say that $\boldsymbol{L}_0^U[\boldsymbol{r}_0, \boldsymbol{s}_0]$ iterates forward to $\boldsymbol{L}_1^U[\boldsymbol{r}_1, \boldsymbol{s}_1]$.

Together these definitions will allow us to apply HLD to the intersections of the manifolds with the symmetry plane. It should be noted that the pseudoneighbor pairs from 2D HLD will not just be the points in the plane but pairs of pole-to-pole intersection curves. Additionally, holes will shadow the pole-to-pole curve through 3D phase space. We refer to the iterates of the intersection of a hole with the symmetry plane in the same way refer to the iterate of an intersection of a pole-to-pole curve with the plane. Bridges and bridge classes are defined the same as in 2D HLD.

It is important to note that the end points of a bridge do not have to iterate to the same $\boldsymbol{L}$ curve. Many times this complication can be avoided by carefully selecting a longer bridge that includes the original bridge. For example, the iterate of $\boldsymbol{L}_0^U[\boldsymbol{q}_0, \boldsymbol{r}_0]$ is not obvious, however $\boldsymbol{L}_0^U[\boldsymbol{p}_0, \boldsymbol{q}_2]$ iterates to $\boldsymbol{L}_1^U$ in a more straightforward manner.

There are two important rules for iterating points forward. First when a point $\boldsymbol{L}_n^{U/S}$ is iterated forward it will lie either on the curve $\boldsymbol{L}_n^{U/S}$ or $\boldsymbol{L}_{n+1}^{U/S}$. A point cannot be iterated forward from $\boldsymbol{L}_n^{U/S}$ to $\boldsymbol{L}_{n+2}^{U/S}$ after only a single iterate. When iterated backward a point will go from $\boldsymbol{L}_n^{U/S}$ to either $\boldsymbol{L}_n^{U/S}$ or $\boldsymbol{L}_{n-1}^{U/S}$. Additionally, for systems with reversibility, if a point lies on the curve L_n^U then it must also lie on the curve L_{-n}^S at some previous iterate.

It is important to note that in the example shown in fig. 6.10 all pole-to-pole intersection curves have their final intersection with the symmetry plane on the curve $\boldsymbol{L}_0^S[\boldsymbol{p}_0, \boldsymbol{q}_2]$. Since the system is reversible all pole-to-pole intersection curves first intersect with the plane on $\boldsymbol{L}_0^U[\boldsymbol{p}_0, \boldsymbol{q}_0]$. We consider $\boldsymbol{L}_0^U[\boldsymbol{p}_0, \boldsymbol{q}_0]$ equivalent to the fundamental segment of a 2D system.

6.5 Constructing the Second Iterate in the Symmetry Plane

Fig. 6.9 shows the most information we could numerically obtain about the manifolds intersection with the symmetry plane. We fully resolve all intersections between the $\boldsymbol{L}_0^U$, $\boldsymbol{L}_0^S$, $\boldsymbol{L}_1^U$, and $\boldsymbol{L}_1^S$ curves. We only partially resolve the $\boldsymbol{L}_2^U$ and $\boldsymbol{L}_2^S$ curves. The information from the intersections of $\boldsymbol{L}_0^U$, $\boldsymbol{L}_0^S$ and $\boldsymbol{L}_1^U$ is insufficient to get any forcing from HLD, though we know it is there. Since we haven't fully resolved $\boldsymbol{L}_2^U$ we cannot directly include it. However, if we consider the intersections between $\boldsymbol{L}_1^U$ and $\boldsymbol{L}_{-1}^S$ we determine the forced intersections at $\boldsymbol{L}_2^U$. Once we understand the minimal forced structure at $\boldsymbol{L}_2^U$ we use HLD to construct the symbolic equations.

Fig. 6.11 contains the first two intersections of the unstable manifold with the plane as well as the first two intersections of the stable manifold with the plane. We use the information contained in fig. 6.11 to construct the second iterate. We identify the pseudoneighbor pairs and place the associated holes. The green hole is between the pseudoneighbor pair $\boldsymbol{s}$ and $\boldsymbol{r}$. This hole prevents the lobe connecting $\boldsymbol{r}$ and $\boldsymbol{s}$ from being topologically distorted to eliminate $\boldsymbol{r}$ and $\boldsymbol{s}$. The purple and orange dots are place above and below $\boldsymbol{t}_0$ to prevent the curves from being distorted to eliminate $\boldsymbol{t}_0$. We track $\boldsymbol{t}$ carefully using our 55 iterate z-stack to identify the first forward and first backward iterate of $\boldsymbol{t}_0$ and its holes.

Using the z-stack we identify how the holes and 1D unstable manifold wind underneath the symmetry plane. The 1D manifold acts similarly to a hole by acting as an end point to the $\boldsymbol{L}_1^U$ curve. We project the holes and 1D unstable manifold onto the symmetry plane as a visual aid, and imagine sliding the curve

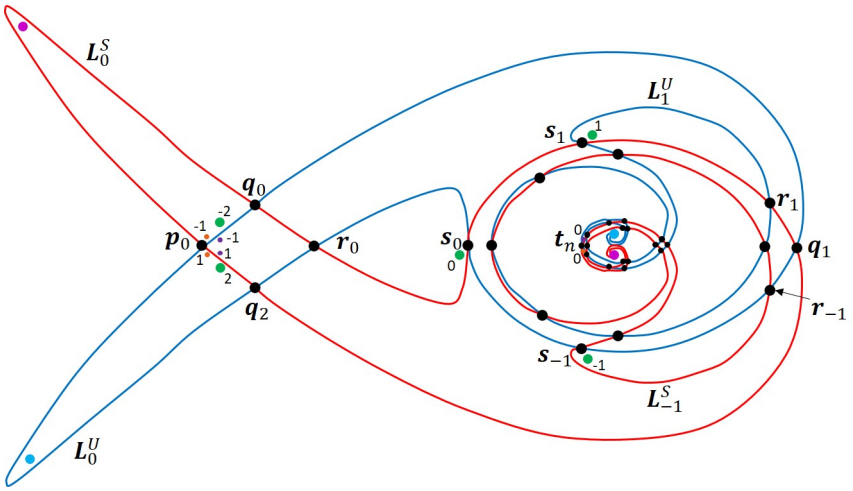

Figure 6.11: The intersection of the 2D unstable manifold (blue) up to $\boldsymbol{L}_1^U$ and the 2D stable manifold (red) up to $\boldsymbol{L}_{-1}^S$ with the symmetry plane. The intersections of three holes with the symmetry plane are denoted by the green, orange, and purple circles.

$\boldsymbol{L}_1^U$ below the symmetry plane and around the holes.

To begin we distort the $\boldsymbol{L}_1^U$ curve to be attached to the holes. This distorted curve is the purple curve in fig. 6.13. The exterior lobe is collapsed onto the green hole and the purple and orange holes are collapsed to the single orange hole since they follow nearly identical paths to their next intersections. As the purple curve is pushed below the symmetry plane it will remain attached to the holes and 1D manifold. Since the holes and 1D unstable manifold end at the symmetry plane the purple curve will eventually lie on the symmetry plane as $\boldsymbol{L}_2^U$.

The minimal forced topology for the $\boldsymbol{L}_2^U$ intersection is shown in fig. 6.14. We have split the orange hole in fig. 6.13 back into its component purple and orange holes. The complex winding of the holes and the 1D unstable manifold produces a $\boldsymbol{L}_2^U$ curve that follows the path $\boldsymbol{L}_0^U$ multiple times before ending at the 1D unstable dot in the bottom left. Portions of the numerically calculated $\boldsymbol{L}_2^U$ in fig. 6.9 are the same as the minimally forced topology of $\boldsymbol{L}_2^U$ in fig. 6.14. However, there is additional structure in the numerical $\boldsymbol{L}_2^U$ that is not forced.

We need to construct the pseudo-ETP shown in fig. 6.15 to confirm the minimal

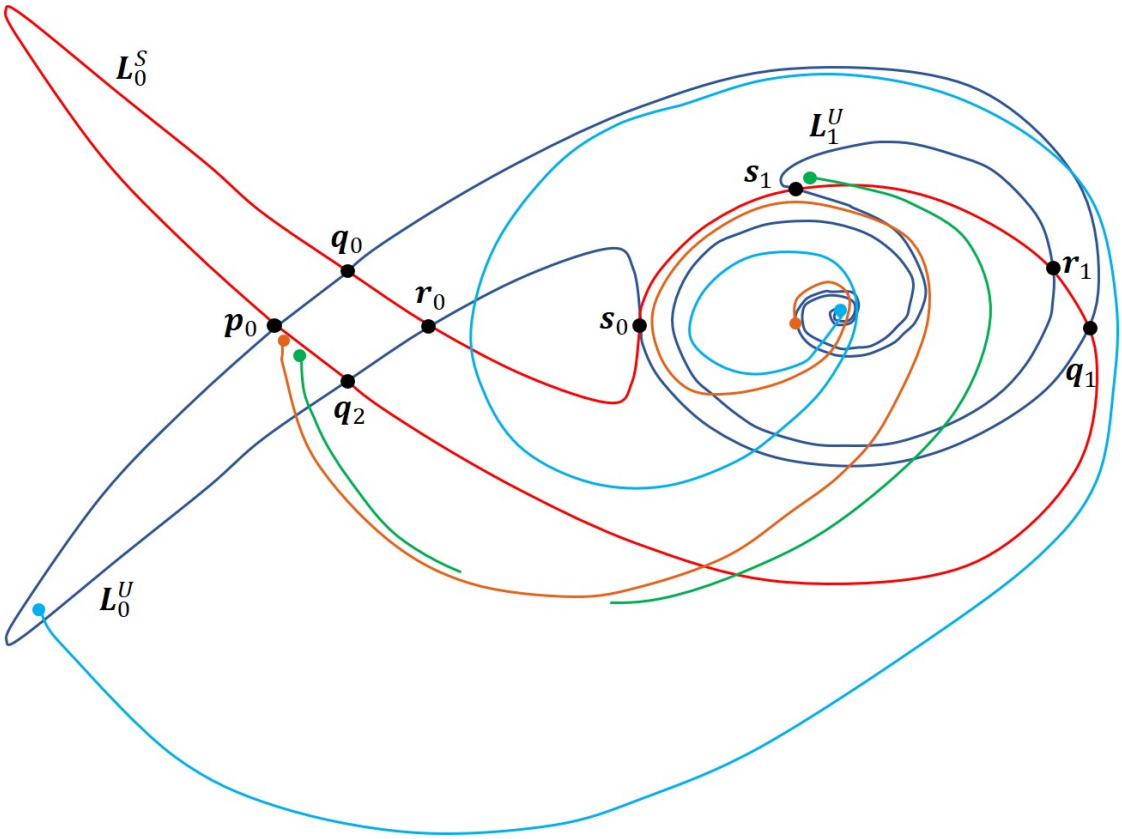

Figure 6.12: The projection of the portion of the holes (orange and purple) and 1D unstable manifold (cyan) beneath the symmetry plane onto the symmetry plane as well as the $\boldsymbol{L}_0^U$, $\boldsymbol{L}_0^S$, and $\boldsymbol{L}_1^U$ curves. We imagine sliding the $\boldsymbol{L}_1^U$ down below the symmetry plane while tracking along the holes to construct $\boldsymbol{L}_2^U$.

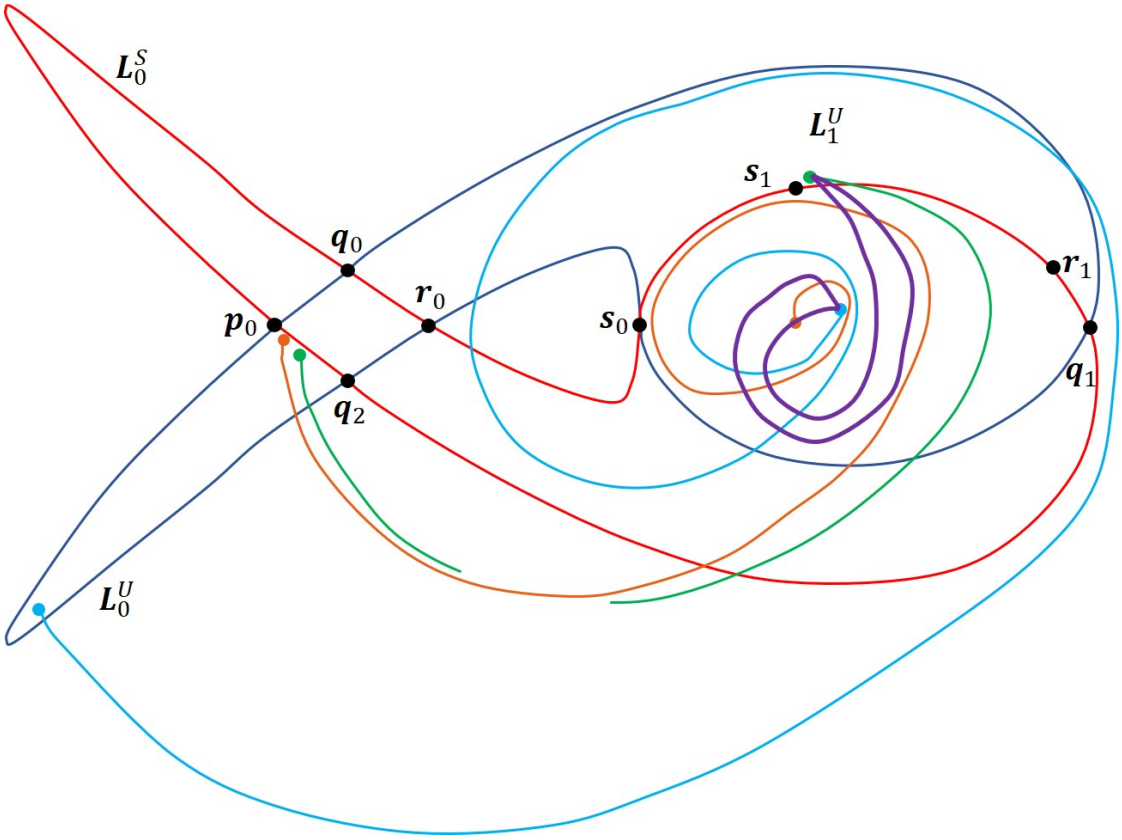

Figure 6.13: The projection of the portion of the holes (orange and purple) and 1D unstable manifold (cyan) beneath the symmetry plane onto the symmetry plane. The purple curves represent $\boldsymbol{L}_1^U$ distorted such that it attaches to the holes.

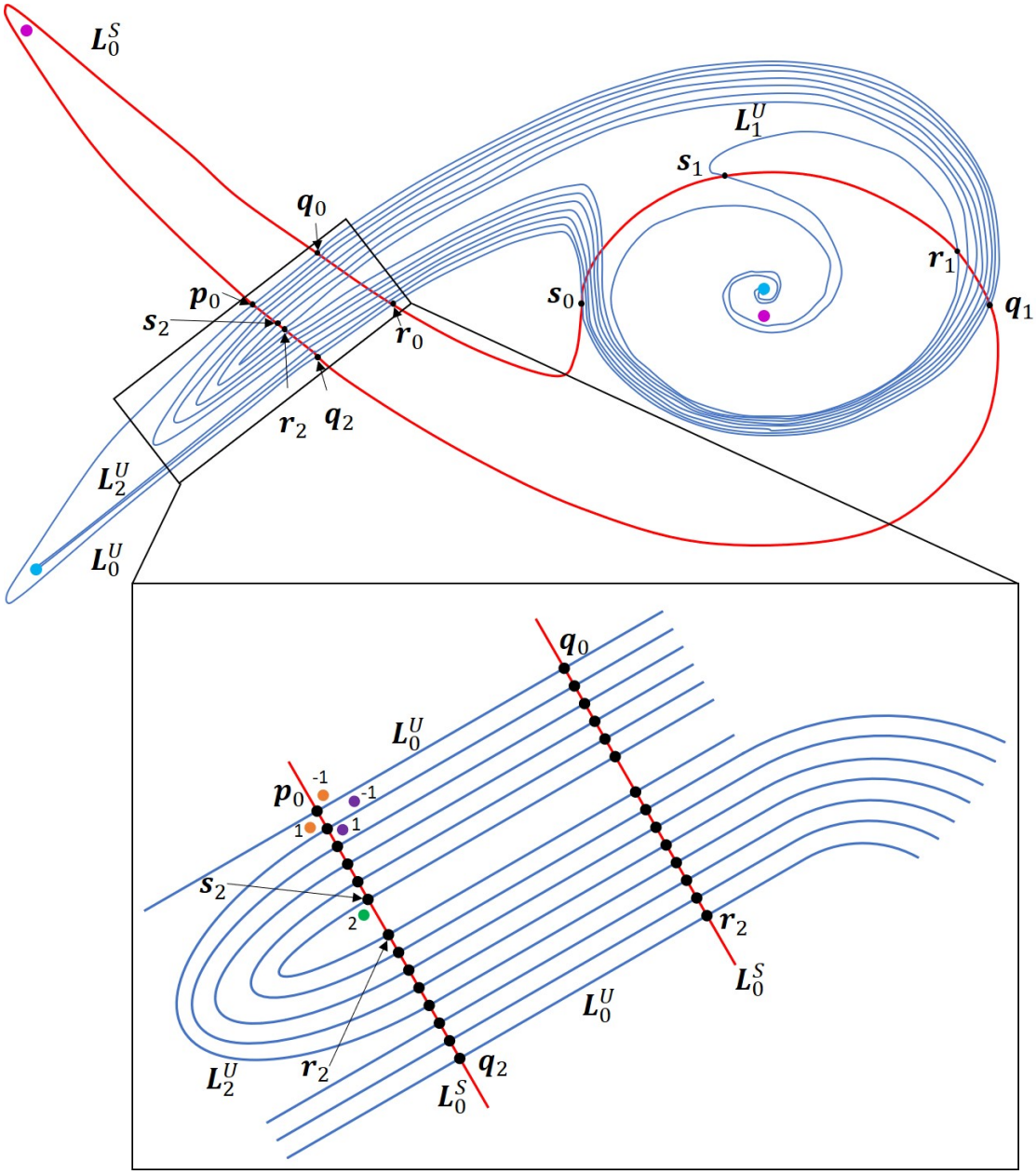

Figure 6.14: The first three minimally forced iterates of the unstable intersection. The minimal forced curve $\boldsymbol{L}_2^U$ is constructed using the 1D unstable manifold and the orange, purple, and green holes.

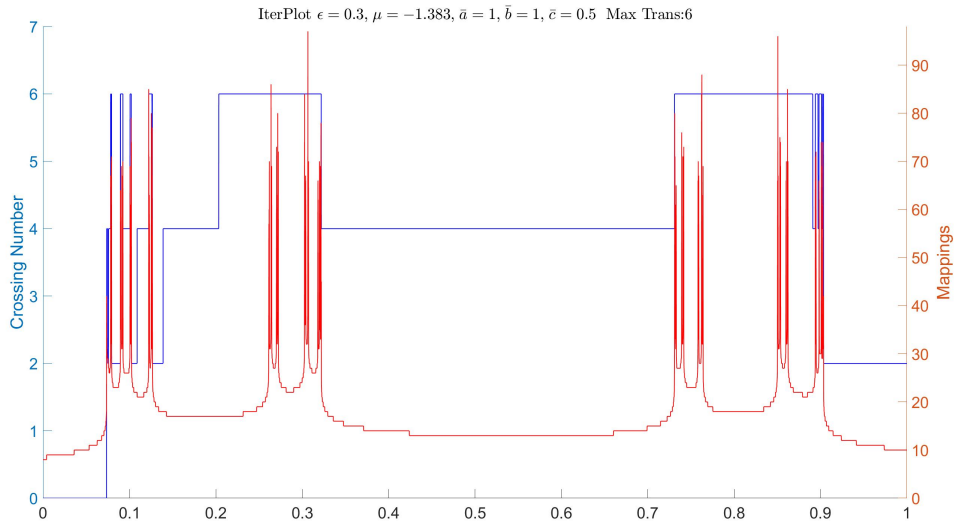

Figure 6.15: The pseudo-ETP constructed by iterating the fundamental segment $\boldsymbol{L}_0^U[\boldsymbol{p}_0, \boldsymbol{q}_0]$ forward. The blue curve corresponds to the number of times a point has crossed the symmetry plane while the red curve corresponds to the number of mappings the point. The points are mapped while below a plane sufficiently far from the fixed points and with less than six crossings.

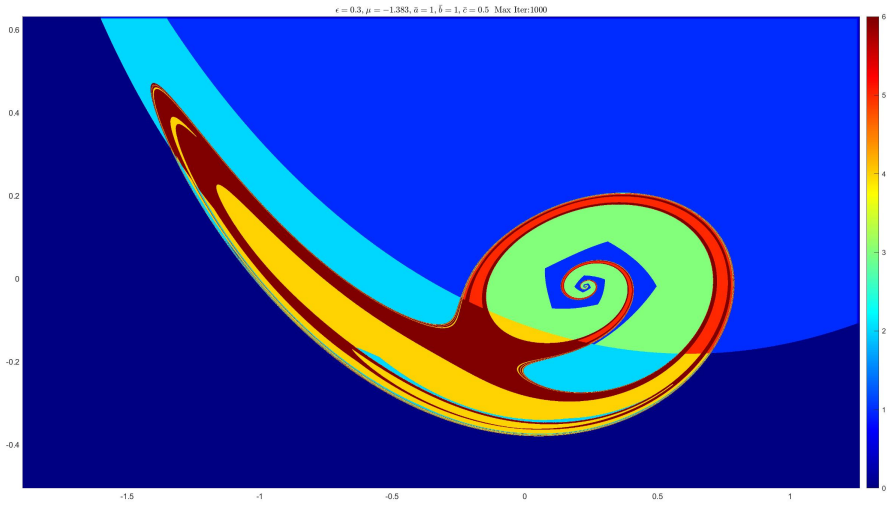

Figure 6.16: The crossing plot constructed by iterating the portion of the symmetry plane near the 2D stable and unstable manifolds. The number of times a point crosses the symmetry plane is tracked and plotted above.

structure we predicted in fig. 6.14. We do this by mapping $\boldsymbol{L}_0^U[\boldsymbol{p}_0, \boldsymbol{q}_0]$ forward while tracking the number of times the points on $\boldsymbol{L}_0^U[\boldsymbol{p}_0, \boldsymbol{q}_0]$ cross the symmetry plane until it "escapes". A point escapes once it is sufficiently above the upper fixed point. Additionally we stop mapping points forward after they reach a maximum number m crossings. We expect regions with a number of crossings less than m will be bordered by a regions with m crossings. We expect that points will only escape for even crossing numbers since we know that the fundamental segment first iterates to $\boldsymbol{L}_1^U$ before getting drawn up the exterior $\boldsymbol{L}_0^U[\boldsymbol{p}_0, \boldsymbol{q}_0]$ lobe.

In fig. 6.15 we note that there are segments where segments with crossing number two are directly adjacent to segments with crossing number four instead of the expect six. To understand why this occurs we examined the crossing plot for the symmetry plane. The crossing plot in fig. 6.16 is constructed by taking the portion of the symmetry plane near the intersections of the 2D stable and unstable manifold and mapping it forward while tracking the number of times a point on the plane crosses the plane. We obtain structure similar to the intersection plots since

the stable and unstable manifolds act to separate regions of transport in phase space. The region of the crossing plot that corresponds to $\boldsymbol{L}_0^S$ encloses domains with four different crossing numbers. This comes as a result of the symmetry plane not being invariant under the map. After one mapping, some portions of the plane map upward while others downward resulting in the patchwork regions seen in fig. 6.16. The non-invariant nature of the plane is also the cause of the issue with the pseudo-ETPs.

If a point on the fundamental annulus lies on a pole-to-pole curve then it will take an infinite number of mappings for the point to escape. In the pseudo-ETP plot the regions of high mapping correspond to points near the pole-to-pole curves while regions with a comparatively low number of mappings have escaped. We identify the regions that escape by overlaying the number of mappings the fundamental segment goes though with the number of crossings. We expect that points of the fundamental segment that iterate to $\boldsymbol{L}_2^U$ will have crossing number two or four.

We see from the magnified portion of fig. 6.14 that there are 12 segments of $\boldsymbol{L}_2^U$ that we predict to escape. A close examination of fig. 6.15 has 14 escaped segments. This indicates that the topology of the numerics includes the minimal topology that we expected.

6.6 Applying HLD

Using the minimal $\boldsymbol{L}_2^U$ topology in fig. 6.14 we identify all the bridge classes that make up our system as shown in fig. 6.17a. We concatenate some of the bridge classes into $\bar{A}$, $\bar{M}$ and $\bar{L}$ to keep our symbolic dynamics more compact. These concatenated bridges are shown in fig. 6.17b in bold. The concatenated bridges are:

$$\begin{aligned} \bar{A} &= ABC \\ \bar{M} &= MBC \\ \bar{L} &= L^{-1}BC \end{aligned} \tag{6.3}$$

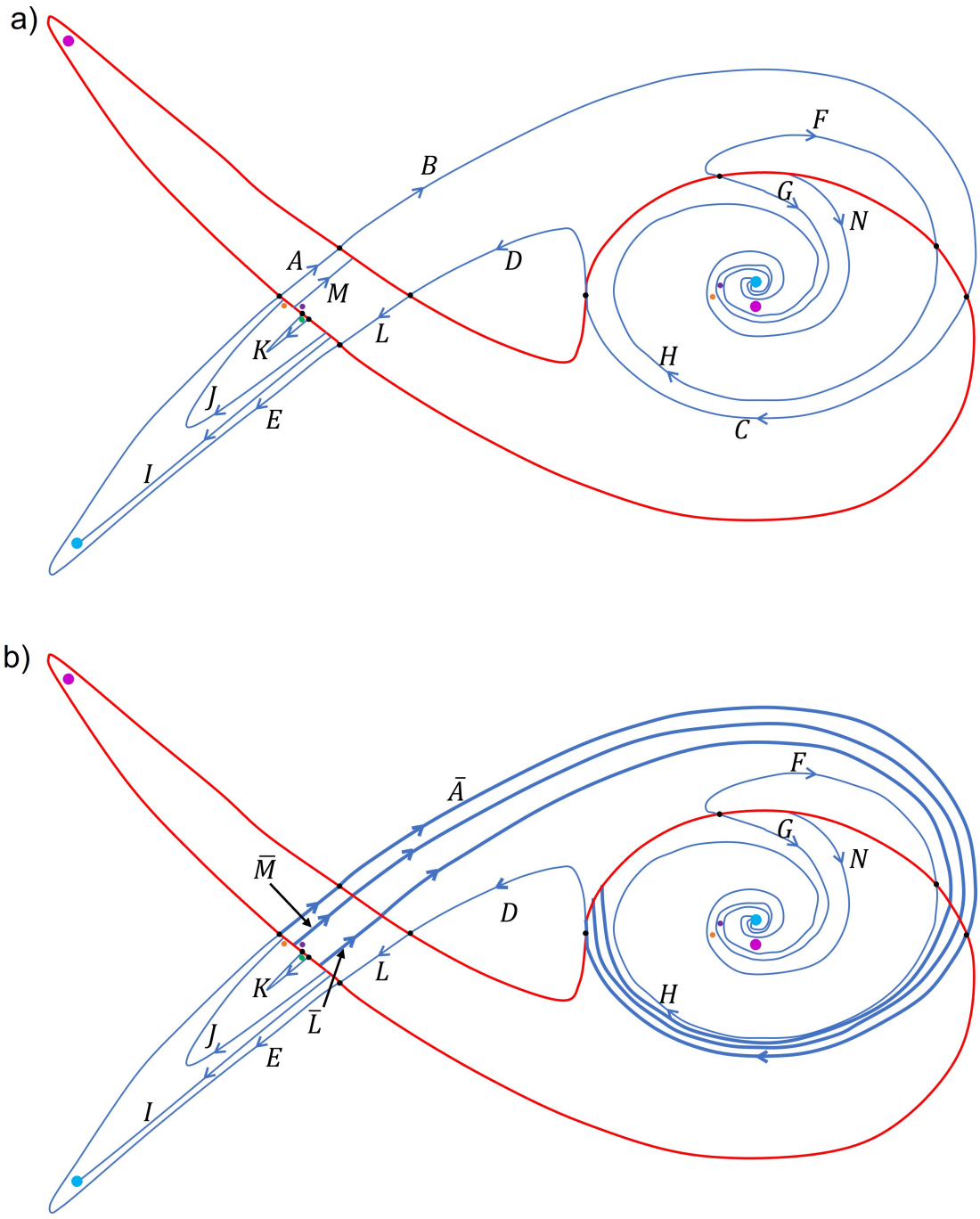

Figure 6.17: The bridge classes that make up our example with arrows indicating direction of the bridge class. In a) all possible bridge classes are shown. In b) some bridge classes have been concatenated together to make up classes $\bar{A}$,$\bar{M}$, and $\bar{L}$.

The bridge classes are iterated forward the same way as in standard 2D HLD. For example, $\boldsymbol{L}_0^U[\boldsymbol{s}_0, \boldsymbol{r}_0]$ is of class D. $\boldsymbol{L}_0^U[\boldsymbol{s}_0, \boldsymbol{r}_0]$ iterates forward to $\boldsymbol{L}_0^U[\boldsymbol{s}_1, \boldsymbol{r}_1]$ of class F. $\boldsymbol{L}_1^U[\boldsymbol{s}_0, \boldsymbol{r}_1]$ iterates forward to $\boldsymbol{L}_2^U[\boldsymbol{s}_0, \boldsymbol{r}_2]$ of class K. We determine the complete set of symbolic equations by repeating this process for the remaining bridge classes we get the complete set of symbolic equations,

$$
\begin{aligned}
M(\bar{A}) &= G^{-1} \\
M(D) &= F \\
M(E) &= \bullet \\
M(F) &= K^{-1} \\
M(G^{-1}) &= I^{-1}L^{-1}D^{-1}\bar{M}^{-1}K^{-1}L^{-1}D^{-1}\bar{L}^{-1}K^{-1}L^{-1}D^{-1}\bar{L}^{-1} \\
M(H^{-1}) &= I^{-1}L^{-1}D^{-1}\bar{L}^{-1}K^{-1}L^{-1}D^{-1}\bar{L}^{-1}K^{-1}L^{-1}D^{-1}\bar{L}^{-1} \\
M(I) &= \bullet \\
M(J) &= \bullet \\
M(K) &= \bullet \\
M(L) &= H \\
M(\bar{L}) &= N^{-1} \\
M(\bar{M}) &= N^{-1} \\
M(N^{-1}) &= I^{-1}L^{-1}D^{-1}\bar{M}^{-1}J^{-1}L^{-1}D^{-1}\bar{L}^{-1}K^{-1}L^{-1}D^{-1}\bar{L}^{-1}.
\end{aligned}
\tag{6.4}
$$

A $\bullet$ indicates the iterate of a bridge class goes to infinity while it's end points track the pole-to-pole curve to the fixed point. As a check, we iterate the concatenation of bridge classes $\bar{A}DLE$ that make up $\boldsymbol{L}_0^U$ forward. We find that,

$$
M(\bar{A}DLE) = G^{-1}FH\bullet \tag{6.5}
$$

which are the bridge classes that make up $\boldsymbol{L}_1^U$ as we would expect. We have six inert classes D, F, I, J, K, and E. We have six active classes H, L, $\bar{M}$, N, $\bar{A}$ and G. $\bar{A}$ and G are also *transient*, or bridge classes that occur only once in the dynamics. Said another way no bridge class iterates to a transient bridge class.

We construct a transition graph using all non-transient active bridge classes in

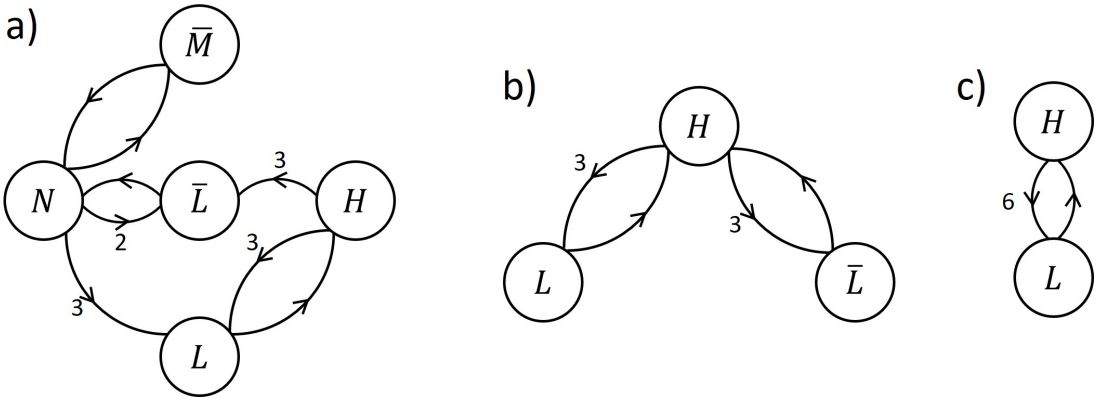

Figure 6.18: Transition graphs for the active symbolic dynamics. a) The full set of non-transient active bridge classes. b) A reduced transition graph after combining bridge classes. c) The most reduced transition graph.

fig. 6.18a. Iterates of the interior $\boldsymbol{L}_1^U$ curves (N and H) produce 6 copies of L (or M). If the purple hole is removed, $\bar{M} \equiv \bar{L}$ and if we ignore the stable 1D manifold, $N \equiv H$ which produces the transition graph in fig. 6.18b. Finally we say $L \equiv \bar{L}$ producing the transition graph in fig. 6.18c. The equivalent transition matrix is:

$$T = \begin{pmatrix} 0 & 1 \\ 6 & 0 \end{pmatrix} \tag{6.6}$$

from which we get lower bound of the topological entropy $h_{top} = \ln 6$. From the transition graph we expect that every two iterates of an L bridge will produce six new L bridges.

By zooming in on the pseudo-ETP we should see repetition of the escaping L classes. In fig. 6.19a the pseudo-ETP has 14 unescaped segments. If we zoom in on the segment in the brackets while increasing the maximum number of allowed crossing we get fig. 6.19b. This is equivalent to iterating an L class forward twice. Fig 6.19b is topologically similar to fig. 6.19a but it is mirrored. We repeat the process for the bracketed section of fig. 6.19b to get fig. 6.19c with the same result.

Here we have seen the successful application of a modified 2D HLD to a numerical example where the 2D stable and unstable manifolds intersect with a symmetry plane. We used a combination of numerical data and forced topology to generated

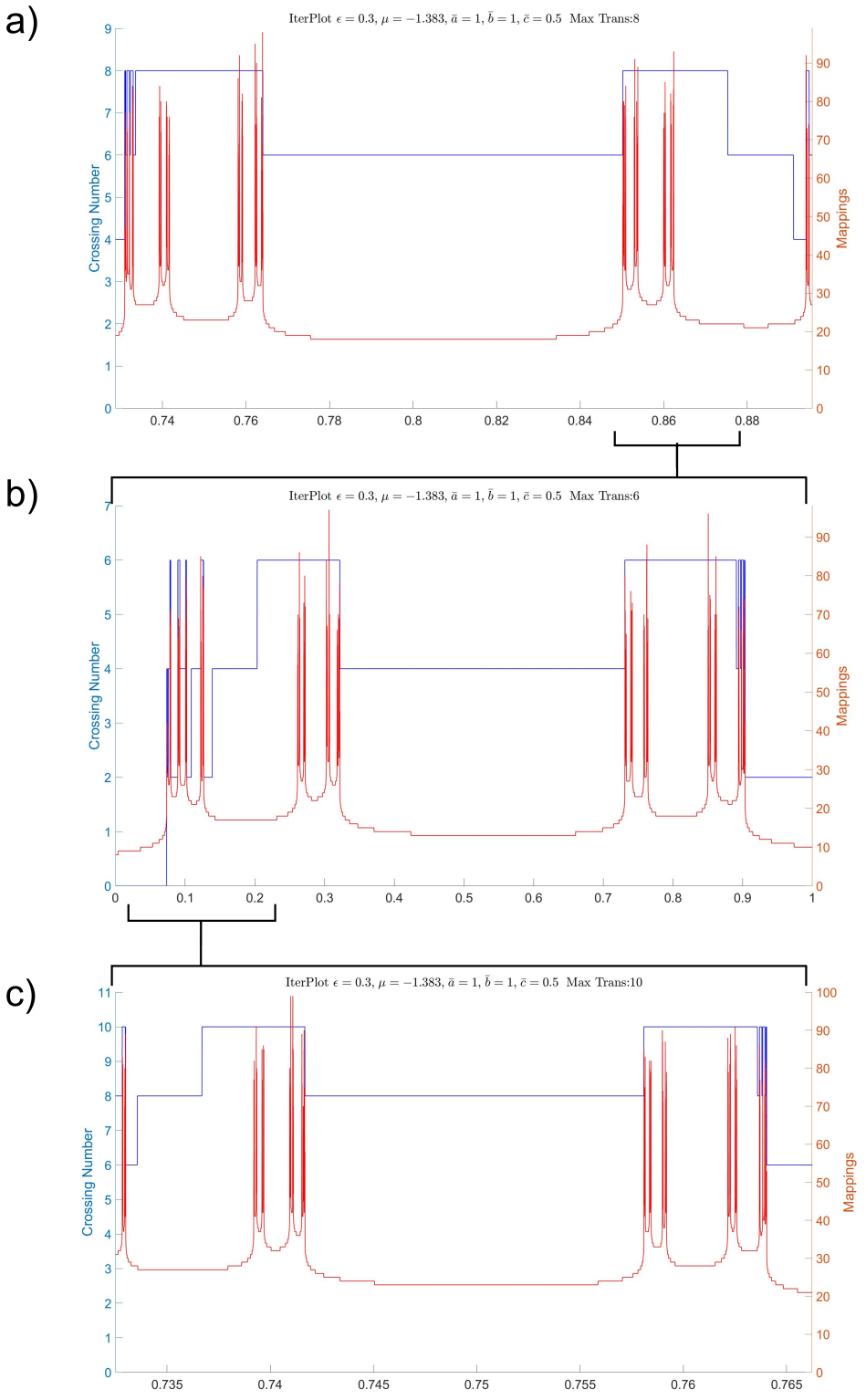

Figure 6.19: The fractal structure that occurs after two iterations of an L bridge class. Each iterate of and L class will produce a minimum of six newly escaped segments.

a system of symbolic equations. These symbolic equations were then tested against numerical data and successfully predicted the minimal observed fractal structure.

6.7 What Unknowns Remain

The application of the modified 2D HLD was successful at predicting some of the forced topological structure of a numerical model. However, it did not fully capture the structure at $\boldsymbol{L}_2^U$, and there remains two outstanding questions.

First, we hope to more accurately model the structure at L_2^U. In the worked example we placed a pair of holes near $\boldsymbol{t}$. This choice was in part impacted by the resolution of the z-stack. An alternative placement of holes closer to the center of the spiral might be able to capture more of the dynamics of the $\boldsymbol{L}_2^U$ curve.

Second, we want to understand why there seems to be two segments of $\boldsymbol{L}_2^U$ that seem to spiral to the center 1D unstable manifold in fig. 6.9. We expect that $\boldsymbol{L}_2^U$ should only end at the lower left 1D unstable intersection. We have two possible explanations: 1) it's possible that the $\boldsymbol{L}_2^U$ curve spiraling into the center 1D unstable manifold intersection actually turns around and we cannot resolve the turn; and 2) that intersections between the $\boldsymbol{L}_2^U$ and $\boldsymbol{L}_{-1}^S$ curves are forcing the additional structure. If these intersections are the cause then careful selection of holes for these interactions should allow us to construct the minimally forced $\boldsymbol{L}_2^U$ that leads to these dynamics.

Finally, we can slightly adjust the ϵ and μ parameters to get dynamics that are easier to resolve. In our explorations of parameter space we've found that setting $\mu = -1.4$ while keeping the other parameters the same might lead to better system.

Overall the extension of 2D HLD to the intersections of the 2D stable and unstable manifolds with a plane is extremely useful. We are now able to analyze a greater number of systems with a less computational load. Additionally previous versions of HLD would struggle with systems with an infinite number of forced pole-to-pole intersections while this new extension handles them.

Chapter 7

Conclusion

7.1 New Directions

This project illuminates a number of fruitful avenues for future research. We have shown that HLD works for a number of 3D systems. In its most basic application HLD can be applied to systems with 2D stable and unstable manifolds that intersect at equatorially. These types of systems are generic for reversible systems with two fixed points and a plane of invariant points under the reversor. Future work might examine a map with the above conditions in detail.

HLD can also be applied to systems with pole-to-pole invariant circles. A future project could include identifying such a system, computing the pole-to-pole intersections, then computing the stable and unstable manifolds of the pole-to-pole intersections. Once the manifolds are obtained HLD could be applied as outlined in chapter 5.

Another project would involve more exploration of the quadratic family of maps. We have examined only one case of forced pole-to-pole intersections. There are many more such systems within the quadratic family of maps ripe for exploration. Additionally there are likely to be hyperbolic plateaus that need to be identified.

In our work we have ignored the case of bubble-type intersections between the 2D manifolds. We are not currently sure if bubble-type intersections are actually wedge type intersections or if they their own unique case. If they are unique

the limited information HLD from sec. 5.3 could be applied and tested. Alternatively their unique structure may require more refinement of 3D HLD to get their complete dynamics. More exploration is clearly needed.

2D HLD can also be used to identify periodic orbits. Work still needs to be done to determine how to use 3D HLD to identify periodic orbits. We have seen some of the necessary dynamics in this work and feel that 3D HLD could be used to identify periodic orbits in these systems.

Outside of HLD, one might consider how pole-to-pole curves wrap around each other in phase space. This is especially intriguing in the case with forced pole-to-pole intersection curves as they seem to wind around each other in increasingly complex ways. One possible way to analyze the pole-to-pole curves is to apply braid theory to the pole-to-pole curves. A combination of our numerical computation of the intersections in the symmetry plane could be combined Jason Mireles-James work to compute the pole-to-pole curves using a Taylor expansion [35] to accurately model the pole-to-pole curves in phase space. The curves could then be analyzed using braid theory.

Finally, HLD needs to be extended into higher dimensional systems. 3D HLD is in of itself quite powerful and there are many applications for it in 3D but we would like to be able to apply HLD to 4D symplectic maps. Three-degree-of-freedom Hamiltonian systems generate flows in six-dimensional phase space however if one is fortunate the flow can be reduced to four-dimensional phase space. This is a rich environment to explore and 4D HLD would be a powerful tool.

7.2 Concluding Remarks

HLD is a powerful tool for exploring area-preserving 2D and volume-preserving 3D maps. While its usefulness in 2D is well studied, it is only recently that it has been extended to 3D maps. Specifically, HLD has been shown to work for systems with equatorial intersection curves, pole-to-pole invariant circles, and topologically forced pole-to-pole intersection curves. Continuing work on HLD promises to produce a wealth of possible rewards, from deeper exploration of 3D maps to its first

forays into 4D phase space. It is my hope that the work contained within this dissertation will be built upon to understand ever more complex topologies.

Bibliography

[1] Hassan Aref, John R. Blake, Marko Budišić, Silvana S. S. Cardoso, Julyan H. E. Cartwright, Herman J. H. Clercx, Kamal El Omari, Ulrike Feudel, Ramin Golestanian, Emmanuelle Gouillart, GertJan F. van Heijst, Tatyana S. Krasnopolskaya, Yves Le Guer, Robert S. MacKay, Vyacheslav V. Meleshko, Guy Metcalfe, Igor Mezić, Alessandro P. S. de Moura, Oreste Piro, Michel F. M. Speetjens, Rob Sturman, Jean-Luc Thiffeault, and Idan Tuval. Frontiers of chaotic advection. *Rev. Mod. Phys.*, 89:025007, Jun 2017.

[2] Joshua G. Arenson and Kevin A. Mitchell. Topological dynamics of volume-preserving maps without an equatorial heteroclinic curve. *Physica D: Nonlinear Phenomena*, 424:132925, 2021.

[3] G. K. Bachelor. *An Introduction to Fluid Dynamics*. Cambridge University Press, 2000.

[4] Armando Bazzani and Annamaria Di Sebastiano. Perturbation theory for volume-preserving maps: Application to the magnetic field lines in plasma physics. *Analysis and Modelling of Discrete Dynamical Systems, Adv. Discrete Math. Appl*, 1:283–300, 1998.

[5] Darin Beigie. Codimension-one partitioning and phase space transport in multi-degree-of-freedom hamiltonian systems with non-toroidal invariant manifold intersections. *Chaos, Solitons & Fractals*, 5(2):177 – 211, 1995.

[6] Simon A. Berman and Kevin A. Mitchell. Trapping of swimmers in a vortex lattice. *Chaos*, 30(6):063121, 2020.

[7] M. Bestvina and M. Handel. Train-tracks for surface homeomorphisms. *Topology*, 34:109, 1995.

[8] Tommy A. Byrd and John B. Delos. Topological analysis of chaotic transport through a ballistic atom pump. *Phys. Rev. E*, 89:022907, Feb 2014.

[9] Ivan C. Christov, Richard M. Lueptow, Julio M. Ottino, and Rob Sturman. A study in three-dimensional chaotic dynamics: Granular flow and transport in a bi-axial spherical tumbler. *SIADS20*, 13(2):901–943, 2014.

[10] Pieter Collins. Dynamics forced by surface trellises. In *Geometry and topology in dynamics*, volume 246 of *Contemp. Math.*, pages 65–86. Amer. Math. Soc., Providence, RI, 1999.

[11] Pieter Collins. Symbolic dynamics from homoclinic tangles. *International Journal of Bifurcation and Chaos*, 12(03):605–617, 2002.

[12] Pieter Collins. Dynamics of surface diffeomorphisms relative to homoclinic and heteroclinic orbits. *Dyn. Syst.*, 19:1–39, 2004.

[13] Pieter Collins. Entropy-minimizing models of surface diffeomorphisms relative to homoclinic and heteroclinic orbits. *Dyn. Syst.*, 20:369–400, 2005.

[14] Pieter Collins. Forcing relations for homoclinic orbits of the Smale horseshoe map. *Exp. Math.*, 14(1):75–86, 2005.

[15] Pieter Collins and Kevin A. Mitchell. Graph duality in surface dynamics. *Journal of Nonlinear Science*, May 2019.

[16] Michael J. Davis. Bottlenecks to intramolecular energy transfer and the calculation of relaxation rates. *The Journal of Chemical Physics*, 83(3):1016–1031, 1985.

[17] Michael J. Davis and Stephen K. Gray. Unimolecular reactions and phase space bottlenecks. *The Journal of Chemical Physics*, 84(10):5389–5411, 1986.

[18] Sarah Day, Rafael Frongillo, and Rodrigo Treviño. Algorithms for rigorous entropy bounds and symbolic dynamics. *SIAM Journal on Applied Dynamical Systems*, 7(4):1477–1506, 2008.

[19] Nelson De Leon and B. J. Berne. Intramolecular rate process: Isomerization dynamics and the transition to chaos. *The Journal of Chemical Physics*, 75(7):3495–3510, 1981.

[20] G Drótos and C Jung. The chaotic saddle of a three degrees of freedom scattering system reconstructed from cross-section data. *J. of Phys. A*, 49(23):235101, 2016.

[21] Gábor Drótos, Francisco González Montoya, Christof Jung, and Tamás Tél. Asymptotic observability of low-dimensional powder chaos in a three-degrees-of-freedom scattering system. *Phys. Rev. E*, 90:022906, Aug 2014.

[22] H. R. Dullin and J. D. Meiss. Quadratic volume-preserving maps: Invariant circles and bifurcations. *SIADS*, 8(1):76–128, 2009.

[23] R. W. Easton. Trellises formed by stable and unstable manifolds in the plane. *Trans. Am. Math. Soc.*, 294:719, 1986.

[24] R.W. Easton. *Geometric Methods for Discrete Dynamical Systems*. Oxford University Press, New York, 1998.

[25] Gregory S. Ezra, Holger Waalkens, and Stephen Wiggins. Microcanonical rates, gap times, and phase space dividing surfaces. *The Journal of Chemical Physics*, 130(16):164118, 2009.

[26] Matthew D. Finn and Jean-Luc Thiffeault. Topological optimization of rod-stirring devices. *SIAM Review*, 53(4):723–743, 2011.

[27] Matthew D. Finn and Jean-Luc Thiffeault. Topological entropy of braids on the torus. *SIAM Journal on Applied Dynamical Systems*, 6(1):79–98, 2007.

[28] Frederic Gabern, Wang S. Koon, Jerrold E. Marsden, and Shane D. Ross. Theory and computation of non-rrkm lifetime distributions and rates in chemical systems with three or more degrees of freedom. *Physica D: Nonlinear Phenomena*, 211(3–4):391 – 406, 2005.

[29] Richard E. Gillilan and Gregory S. Ezra. Transport and turnstiles in multidimensional hamiltonian mappings for unimolecular fragmentation: Application to van der waals predissociation. *J. of Chem. Phys.*, 94(4):2648–2668, 1991.

[30] F Gonzalez, G Drotos, and C Jung. The decay of a normally hyperbolic invariant manifold to dust in a three degrees of freedom scattering system. *Journal of Physics A: Mathematical and Theoretical*, 47(4):045101, jan 2014.

[31] Francisco Gonzalez Montoya, Florentino Borondo, and Christof Jung. Atom scattering off a vibrating surface: An example of chaotic scattering with three degrees of freedom. *Communications in Nonlinear Science and Numerical Simulation*, 90:105282, 2020.

[32] Boris Hasselblatt and Anatole Katok. *A First Course in Dynamics: With a Panorama of Recent Developments*. Cambridge University Press, 2003.

[33] M. HÉNON. Numerical study of quadratic area-preserving mappings. *Quarterly of Applied Mathematics*, 27(3):291–312, 1969.

[34] Ünver Çiftçi and Holger Waalkens. Reaction dynamics through kinetic transition states. *Phys. Rev. Lett.*, 110:233201, Jun 2013.

[35] J. D. Mireles James and Hector Lomelí. Computation of heteroclinic arcs with application to the volume preserving hénon family. *SIADS*, 9(3):919–953, 2010.

[36] C Jung, O Merlo, T H Seligman, and W P K Zapfe. The chaotic set and the cross section for chaotic scattering in three degrees of freedom. *New Journal of Physics*, 12(10):103021, 2010.

[37] Nidhi Khurana and Nicholas T. Ouellette. Interactions between active particles and dynamical structures in chaotic flow. *Phys. of Fluids*, 24:091902, 2012.

[38] Chun-Biu Li, Akira Shoujiguchi, Mikito Toda, and Tamiki Komatsuzaki. Definability of no-return transition states in the high-energy regime above the reaction threshold. *Phys. Rev. Lett.*, 97:028302, Jul 2006.

[39] Hector E Lomelí and James D Meiss. Quadratic volume-preserving maps. *Nonlinearity*, 11(3):557, 1998.

[40] Hector E. Lomelí and James D. Meiss. Heteroclinic primary intersections and codimension one melnikov method for volume-preserving maps. *Chaos*, 10(1):109–121, 2000.

[41] Edward N. Lorenz. The mechanics of vacillation. *Journal of Atmospheric Sciences*, 20(5):448 – 465, 1963.

[42] R S MacKay and D C Strub. Bifurcations of transition states: Morse bifurcations. *Nonlinearity*, 27(5):859–895, apr 2014.

[43] B. Maelfeyt, S. A. Smith, and K. A. Mitchell. Using invariant manifolds to construct symbolic dynamics for 3d maps. *SIADS*, 16, 2017.

[44] J. D. Meiss. Thirty years of turnstiles and transport. *Chaos*, 25(9), 2015.

[45] J. D. Mireles James. Quadratic volume-preserving maps: (un)stable manifolds, hyperbolic dynamics, and vortex-bubble bifurcations. *Journal of Nonlinear Science*, 23(4):585–615, Aug 2013.

[46] Konstantin Mischaikow and Marian Mrozek. Chaos in the Lorenz equations: a computer-assisted proof. *Bull. Amer. Math. Soc. (N.S.)*, 32(1):66–72, 1995.

[47] Konstantin Mischaikow and Marian Mrozek. Chaos in the Lorenz equations: a computer assisted proof. II. Details. *Math. Comp.*, 67(223):1023–1046, 1998.

[48] Konstantin Mischaikow, Marian Mrozek, and Andrzej Szymczak. Chaos in the Lorenz equations: a computer assisted proof. III. Classical parameter values. volume 169, pages 17–56. 2001. Special issue in celebration of Jack K. Hale's 70th birthday, Part 3 (Atlanta, GA/Lisbon, 1998).

[49] K. A. Mitchell and J. B. Delos. A new topological technique for characterizing homoclinic tangles. *Physica D*, 221:170, 2006.

[50] K. A. Mitchell, J. P. Handley, B. Tighe, S. K. Knudson, and J. B. Delos. Geometry and topology of escape. I. epistrophes. *Chaos*, 13:880, 2003.

[51] Kevin A. Mitchell. The topology of nested homoclinic and heteroclinic tangles. *Physica D*, 238(7):737–763, 2009.

[52] Kevin A. Mitchell. Partitioning two-dimensional mixed phase spaces. *Physica D: Nonlinear Phenomena*, 241(20):1718 – 1734, 2012.

[53] H. K. Moffatt and D. W. Moore. The response of hill's spherical vortex to a small axisymmetric disturbance. *Journal of Fluid Mechanics*, 87(4):749–760, 1978.

[54] Shibabrat Naik and Stephen Wiggins. Finding normally hyperbolic invariant manifolds in two and three degrees of freedom with hénon-heiles-type potential. *Phys. Rev. E*, 100:022204, Aug 2019.

[55] Jaison Novick and John B. Delos. Chaotic escape from an open vase-shaped cavity. ii. topological theory. *Phys. Rev. E*, 85:016206, Jan 2012.

[56] R. Paškauskas, C. Chandre, and T. Uzer. Dynamical bottlenecks to intramolecular energy flow. *Phys. Rev. Lett.*, 100:083001, Feb 2008.

[57] Jules Henri Poincare. *Acta Mathematica*, 13, 1890.

[58] V. Rom-Kedar. Transport rates of a class of two-dimensional maps and flows. *Physica D*, 43:229, 1990.

[59] V. Rom-Kedar. Homoclinic tangles-classification and applications. *Nonlinearity*, 7:441, 1994.

[60] Sulimon Sattari, Qianting Chen, and Kevin A. Mitchell. Using heteroclinic orbits to quantify topological entropy in fluid flows. *Chaos*, 26(3), 2016.

[61] Sulimon Sattari and Kevin A. Mitchell. Using periodic orbits to compute chaotic transport rates between resonance zones. *Chaos*, 27(11):113104, 2017.

[62] Spencer A. Smith, Joshua Arenson, Eric Roberts, Suzanne Sindi, and Kevin A. Mitchell. Topological chaos in a three-dimensional spherical fluid vortex. *EuroPhys. Lett.*, 117(6):60005, mar 2017.

[63] J.-L. Thiffeault and M. D. Finn. Topology, braids and mixing in fluids. *Phil. Trans. A*, 364:3251, 2006.

[64] Mikito Toda. Crisis in chaotic scattering of a highly excited van der waals complex. *Phys. Rev. Lett.*, 74:2670–2673, Apr 1995.

[65] Loring W. Tu. *An Introduction to Manifolds*. Springer Science+ Business Media, 2011.

[66] T Uzer, Charles Jaffé, Jesús Palacián, Patricia Yanguas, and Stephen Wiggins. The geometry of reaction dynamics. *Nonlinearity*, 15(4):957, 2002.

[67] Holger Waalkens, Andrew Burbanks, and Stephen Wiggins. Phase space conduits for reaction in multidimensional systems: Hcn isomerization in three dimensions. *The Journal of Chemical Physics*, 121(13):6207–6225, 2004.

[68] Holger Waalkens, Roman Schubert, and Stephen Wiggins. Wigner's dynamical transition state theory in phase space: classical and quantum. *Nonlinearity*, 21(1):R1–R118, dec 2007.

[69] S Wiggins, L Wiesenfeld, C Jaffé, and T Uzer. Impenetrable barriers in phase-space. *Phys. Rev. Lett.*, 86(24):5478, 2001.

[70] Stephen Wiggins. On the geometry of transport in phase space I. transport in k-degree-of-freedom hamiltonian systems, $2 \leq k < \infty$. *Physica D*, 44(3):471 – 501, 1990.

[71] Stephen Wiggins. The dynamical systems approach to lagrangian transport in oceanic flows. *Annual Review of Fluid Mechanics*, 37(1):295–328, 2005.